

NUMERICAL EVALUATION OF BRIGHT SPOTS
AND THIN LAYER REFLECTIVITY

By

HAMZAH ABDULGADER ALMOGHRABI
#

Bachelor of Science
University of Petroleum and Minerals
Dhahran, Saudi Arabia
1977

Master of Science
Oklahoma State University
Stillwater, Oklahoma
1983

Submitted to the Faculty of the
Graduate College of the
Oklahoma State University
in partial fulfillment of
the requirements for
the Degree of
DOCTOR OF PHILOSOPHY
December, 1986

Thesis
1986D
A45In
cop. 2



NUMERICAL EVALUATION OF BRIGHT SPOTS
AND THIN LAYER REFLECTIVITY

Thesis Approval:

James Lange

Thesis Adviser

James P. Wicksted

D. C. K...

Wyl A. Selt

Norman N. Dunham

Dean of the Graduate College



ACKNOWLEDGEMENT

All praise is due to ALLAH the Almighty, and peace be upon His Messenger Mohammad.

The author wishes to express sincere appreciation and deep gratitude to his major advisor, Dr. James Lange, for his interest, assistance and invaluable guidance throughout the course of this work. Additional thanks is extended to Dr. L. Scott, Dr. D. Kent, Dr. J. Wicksted and Dr. B. Ackerson for serving on my committee. Special thanks is expressed to Dr. A. Alharthi, Dr. A. Chowdhury and Mr. K. Loudiyi for their comments and encouragement. A note of thanks is given to Mrs. Patty Garrett for typing the manuscript. The help of Mr. P. McCloure and Mrs. Barbara Lange in editing the manuscript is deeply appreciated.

Thanks to King Faisal University and the Saudi Arabian Educational Mission for their financial support. Thanks and gratitude are also extended to all who have contributed in increasing my knowledge.

For you, dear parents, respected brothers and sisters, my dear wife, my lovely daughters Ibtehal and Shaima, and my lovely son Moath, thank you all for the continued help and encouragements, and for all of you, this study is dedicated.

TABLE OF CONTENTS

CHAPTER	Page
I. INTRODUCTION	1
1. Statement of The Problem	1
2. Importance of The Study.	2
3. Limitation of The Study	5
4. Procedure of The Study	7
5. Review of Related Literature	9
II. NUMERICAL METHOD.	12
1. Modeling Procedure and Input Parameters	12
2. Reflection of Plane Waves at a Single Interface	14
a. Wave Propagation	14
b. Boundary Conditions	18
c. Incident P-wave	19
d. Incident S-wave	20
e. Partitioning of Energy	21
3. Reflection of a P-wave From a Single Layer	23
a. Wave-sum Technique	23
b. Multiple Waves	30
c. Mode Converted Waves	36
d. Thin Layer Reflectivity to an Incident Impulse	45
4. Reflection of a Pulse From a Thin Layer.	48
a. Input Signal	48
b. The Fourier Transform	51
c. Convolution	53
d. Waveform Sampling.	54
e. The Discrete Fourier Transform	56
III. NUMERICAL RESULTS AND DISCUSSION	58
1. Layer Reflectivity and Bright Spots	58
a. Amplitude Anomalies For Different Lithologies	58
b. Amplitude Variation With Offset and Layer Parameters	58
c. Phase-shift Variation With Offset and Layer Parameters	72
d. Mode Converted Shear Waves	69
2. Thin Layer Response to an Incident Impulse	82
a. Layer Thickness	82
b. Layer Lithology and Pore-fluid	84
c. Bounding material.	88
d. Spectral Character of Reflected Wavelets	95
e. MPA Definition and Applications.	111
IV. SUMMARY AND CONCLUSION	116

CHAPTER	Page
REFERENCES	123
APPENDIX A - Computation of The Fast Fourier Transform	126
APPENDIX B - A Pictorial Table of Fourier Transform Pairs	129
APPENDIX C - Basic Properties of the Fourier Transform	131

LIST OF TABLES

Tables	Page
I. Designations of Mode-Converted Waves Within the Layer	31
II. Physical Properties of Rocks.	32
III. Abbreviations of Multiples and Mode Converted Waves.	39
IV. Seismic-Model Boundary Configurations.	91

LIST OF FIGURES

Figure	Page
1. Structural Configurations Associated with Trapping Hydrocarbons.	4
2. Schematic Diagram of Modeling Procedure	13
3. Reflection of a plane P-wave at an interface of two solids.	17
4. Various paths taken by incident rays which interfere with multiple waves.	26
5. The amplitude of p-waves multiply reflected in the layer.	33
6. The finite wave sum compared to the exact solution at normal incidence.	35
7. The energy flux of the total reflected, transmitted, and mode converted waves.	37
8. The amplitude of mode converted waves which emerge as p-waves from the layer.	41
9. The amplitude of mode converted s-waves for various conversion sequences.	42
10. S-wave directivity patterns of their emergence into the reflection zone.	44
11. The frequency dependence of gas layer reflectivity versus angle of incidence.	46
12. The frequency dependence of brine layer reflectivity as extended beyond the critical angle.	47
13. The input signal in the frequency domain.	49
14. The input Ricker wavelet in the time domain.	50
15. Impulse function convolution.	55
16. Graphical derivation of the discrete Fourier transform pair.	57

Figure	Page
17. The normal component of the reflected amplitude of p-wave for an incident frequency of 40 Hz and thickness of 20 meters (65.5 feet).	60
18. The normal component of the p-wave amplitude of a 40 Hz wave reflected from a 3 meter (10.1 feet) thick layer bounded by identical shale interfaces.. . . .	61
19. The net normal component of the reflected P-wave amplitude for a sandstone layer saturated with gas and bounded by shale.	63
20. The net normal component of the reflected p-wave amplitude for a sandstone layer containing brine and bounded by shale.	64
21. The normal component of the p-wave amplitude surface for a sandstone containing gas when the bounding materials are a shale of higher velocity above and a lower velocity below.	66
22. The normal component of the net reflected P-wave amplitude from a layer of coal encased in dissimilar shale formation [S(H)/CO/S(L)].	68
23. The mode converted s-wave amplitude which results from reflection of a p-wave from a coal layer surrounded by shale.. . . .	70
24. Mode converted s-wave amplitudes for a gas saturated sandstone layer surrounded by shale.	71
25. The phase of net p-wave reflected from a limestone layer surrounded by identical shale boundary material.	73
26. The phase of the net p-wave reflected from a gas-saturated layer encased in shale formation.	74
27. The wave phase for one quarter wavelength thick layer.	75
28. The normal component of the net p-wave amplitude reflected from a gas saturated sandstone bounded above by limestone and below by shale.	77

Figure	Page
29. The amplitude of the mode converted shear waves extended beyond the critical angle for a limestone layer.	79
30. The normal component of the net reflected p-wave extended beyond the critical angle for a limestone layer.	81
31. Seismic traces of reflected P-wave for a wide range of thickness.	83
32. Amplitude offset dependence of reflected P-waves from gas saturated sands.	85
33. Amplitude offset dependence of reflected P-waves from a coal layer.	86
34. Amplitude offset dependence of reflected P-waves from a limestone layer.	87
35. Amplitude offset dependence of reflected P-waves from brine saturated sands.	89
36. Sensitivity of wavelet polarity to the bounding materials.	90
37. Mode-Converted S-waves for a gas saturated sand as a function of offset.	93
38. Mode-converted S-waves for a coal layer as a function of offset.	94
39. Variation of Fourier transforms of reflected P-waves with angle of incidence.	96
40. Relative amplitudes of reflected P-waves versus offset.	98
41. Relative amplitudes of mode converted S-waves versus offset.	99
42. Variation of central frequency of reflected P-waves at normal incidence with thickness and lithology.	100
43. Variation of central frequency of reflected P-waves with offset and thickness for a gas saturated sand.	102
44. Variation of central frequency of reflected P-waves for a limestone layer.	103

Figure	Page
45. Central frequency shift of S-waves due to offset and thickness variations for a gas saturated sand.	104
46. Central frequency shift of S-waves due to offset and thickness variations for a brine saturated sand.	105
47. Scattergram of central frequencies of reflected P-waves and mode converted waves for different lithologies and pore fluids.	107
48. Normalized difference of mode-converted S-waves with respect to the incident Ricker wavelet for a gas saturated sand.	108
49. Normalized difference of mode converted S-waves with respect to the incident Ricker wavelet for a brine saturated sand.	109
50. Schematic diagram of MPA technique when applied to a general formation.	113
51. General scheme of MPA technique when applied to formations having shale boundaries.	115

CHAPTER I

INTRODUCTION

Statement of the Problem

Recently, there has been a growing interest among seismologists in locating hydrocarbon accumulations directly. The motivation behind this interest was the 'believed' correlation between amplitude anomalies (bright spots) and gas bearing formations. However, the existence of non-gas related anomalies indicated the need for detailed analysis of bright spots and other seismic data. Reflected amplitudes are influenced by many factors other than those attributed to lithology and pore-fluid of the subsurface formation.

Seismic modeling is considered a feasible vehicle to establish qualitative and quantitative correlation between the wavelet characteristics and the geologic features of the reflecting system. Furthermore, it can be used to generate synthetic seismic traces for a comparison with real seismic data. Ultimately, it would minimize the ambiguities in data interpretation and provide more reliable methods of investigation.

This study evaluates the potential of using seismic reflection amplitude and impulse shapes as a function of

offset to determine lithology and pore-fluid of thin beds. A numerical model is used to generate synthetic seismic traces as a convolution of thin layer reflectivity with a Ricker wavelet input signal. The parameters used in the numerical model are characteristic of the variation in acoustic impedance which occur when systems change pore-fluid from a liquid to a gas in order to exhibit effects associated with "bright spots". The objectives of this forward modeling are:

1. To analyze the reflected wavelet in the time and frequency domains.
2. To determine the effect of pore fluid and lithology of the investigated layer on the signal shape and frequency content as a function of offset.
3. To evaluate the effect of thickness and physical properties of the bounding materials.
4. To determine mode-converted shear-wave signal character.
5. To develop a multiparameter algorithm based upon wavelet characteristics available in time and frequency domains to identify gas zones.

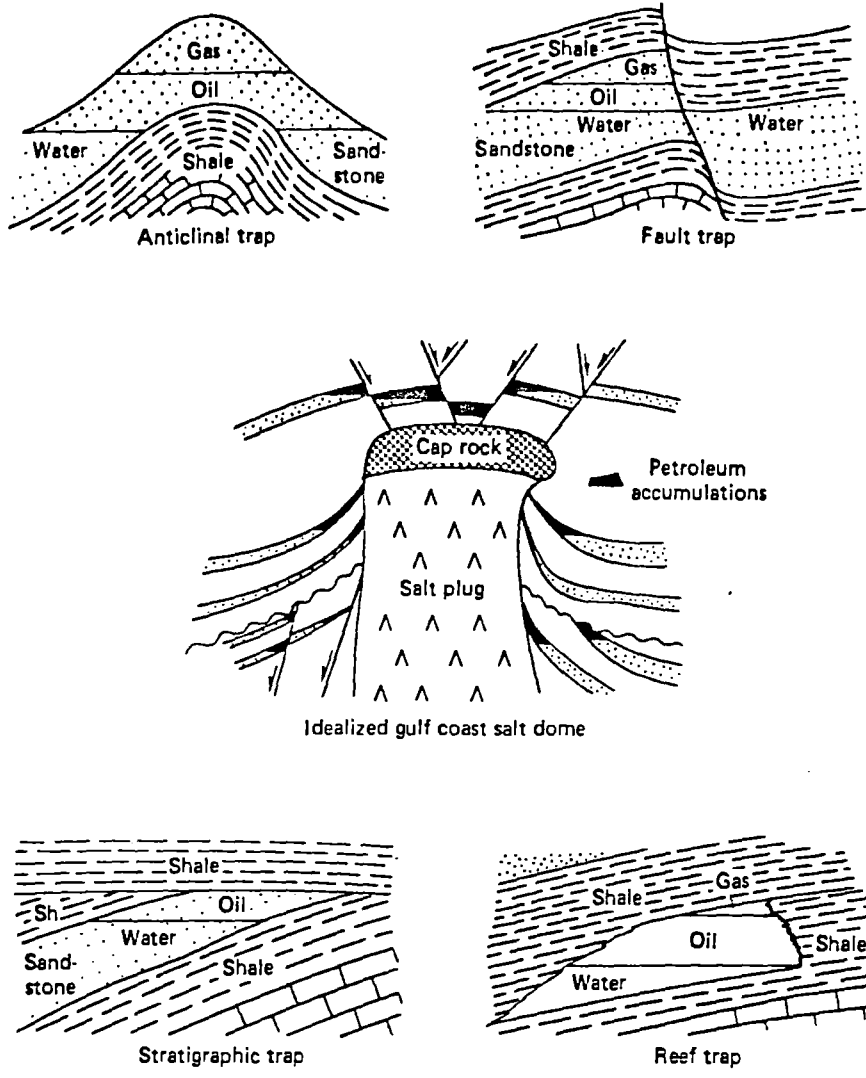
Importance of The Study

Existing information on the amplitude and wavelet character of the seismic response as a function of offset is usually overlooked, mainly because it is not directly correlated to the physical properties of the seismic

section. The common-depth-point (CDP) technique, which was originally designed to cancel unwanted signals by adding traces shot at different source-to-receiver offsets, encodes valuable information of the relative amplitudes as a function of the angle of incidence. In addition to the reflected p-wave there is also the mode-converted s-wave which is mainly determined by the relative shear moduli of the reflecting bed to its surroundings and is distinguished from the p-wave by its later arrival time and direction of propagation.

Consequently, it is very important to utilize all significant features of both types of waves as a function of offset from the seismic reflection profiles to infer maximum subsurface information.

Conventional methods of hydrocarbon exploration were limited to mapping subsurface geological structures by measuring the wave travel-time. The main concern was to recognize structures with geometrical features which are likely to be associated with oil accumulation such as anticlines, faults and salt domes (as shown in Figure 1). In addition to structural reservoirs there are stratigraphic traps, which are a major factor in the world's current oil and gas production and known reserves. Stratigraphic traps are formed by changes within a layer resulting from deposition of sedimentary rocks (of reservoir character), enclosed by sealing rocks. Amplitude anomalies (bright spots) were considered to be the direct technique for



Source: E. A. Robinson and S. Treitel, Geophysical Signal Analysis (New Jersey, 1980), pp. 3.

Figure 1. Illustration of Typical Structural Configurations Associated with Trapping Hydrocarbons.

locating stratigraphically trapped gas. However, the fact that there have been erroneous interpretations of bright spots pointed out the necessity of re-evaluating of bright spot analysis. The acoustic logging evidence indicated that stratigraphic traps have a thin-layer structure; hence detailed analysis of the physical principles of wave propagation and interference in reflecting media is necessary to gain reliable interpretations of stratigraphic traps.

The foregoing discussion explains the reason for choosing a thin-layer model and the importance of an integrated method which utilizes signal characters to identify hydrocarbon reservoirs directly. The method considered here also provides an explanation of the existence of bright spots which are not related to a gas bearing formation and gives more insight to the complex dependence of the reflected signals on the variation of the geological environment of the target layer.

Limitation of the Study

The medium of propagation is assumed to be non-dispersive and isotropic except at finite discontinuities along the z-direction which define the parallel boundaries of the investigated layer. Although the numerical model can be applied to thin and thick layers, it has been limited to thicknesses less than the dominant wavelength of a 25-HZ zero-phase Ricker wavelet typical of exploration

circumstances. Amplitude-offset analysis is limited to source-to-receiver offsets which correspond to pre-critical region. Such a limitation is not severe since this range of angles encompasses offsets larger than most data-gathering strings.

Resolution of thin beds is dependent on the dominant frequency of the incident wavelet, but the increase of attenuation with increasing frequency and depth put an upper boundary for the range of frequency that can be used for deep exploration. A Ricker wavelet is a typical wave resembling the propagation of an impulse in earth strata which experiences a second-order frequency absorption. Analyzing the signal spectrum in the frequency domain added a new dimension in recognizing spectral characters related to the reflecting system which are not seen easily in the time domain.

Although the multiparameter technique developed in this study is successfully applied to various model configurations considered in this study, deviation of real structure from ideal model would lead to limitations and difficulties in direct application of the technique. An example of such difficulties is the variation of frequency content of the reflected signal due to frequency selective absorption, the lateral variation of the velocity, or noise interference. Nevertheless, improvement in seismic data gathering and processing techniques should overcome these

difficulties and make the integrated technique a feasible approach to the evaluation of formation in situ.

Procedure of The Study

A brief description of the numerical model, is introduced in the next chapter followed by evaluation of reflection coefficients at an interface of two solids for an incident plane wave. Both types of waves (p-wave and s-wave) are considered; existence of mode-converted waves is explained when solving the boundary conditions for the wave equation. Partitioning of energy between wave components is introduced and checked by conservation of energy flux.

Layer reflectivity for a monochromatic incident p-wave is developed in the next section. A wave sum technique, which considers the interference of a finite number of multiple and mode converted waves, is discussed in detail. A comparison is made between four types of layers of exploration interest that might lead to bright spots. The comparison is illustrated by displaying the amplitude-offset dependence of the reflected p-wave and the mode converted s-wave.

Next, the overall layer reflectivity is developed for a wavelet of finite duration. The input wavelet is digitized in the time domain and then expanded to its frequency components by applying the fast Fourier transform. Synthetic seismic traces are then generated as a convolution of layer reflectivity with the input wavelet. Effects of

different parameters of the seismic model on the reflected wavelet are studied for thin layers. A brief discussion of Fourier transforms and convolution is given.

Results and discussion are presented in two sections. The first section considers layer reflectivity and bright spots. A distinction is made between bright spots (amplitude anomalies) which are related to lithologies and bright spots which are related to gas bearing formations. The results are displayed for phase-shift and amplitudes of reflected p-waves and s-waves as a function of offset and model parameters. Thin layer response to an incident wavelet is discussed in the next section. Attention is focused on variation of wavelet characters in the time and frequency domains as a function of thickness, bounding material, lithology and pore fluid of the thin layer. Afterwards, a multiparameter algorithm is developed and applied to different seismic model configurations to identify gas zones.

Finally, a brief summary for the study is given with emphasis on the importance of numerical modeling in the evaluation of bright spots and other seismic data. General conclusions regarding limitations and applications of the developed technique are presented and some suggestions for further discussion are provided.

Review of Related Literature

Early in the past decade, the use of bright spot analysis added a new dimension in seismic prospecting for petroleum exploration. The advantage of this analysis (Craft, 1973) is to utilize high-amplitude anomalies, which are easily recognized in seismic sections, as direct indications of gas zones. This technique had led to many discoveries of hydrocarbon accumulation, particularly in young unconsolidated sands, such as gas fields in the Gulf of Mexico.

Unfortunately, amplitude anomalies can be caused by factors other than gas accumulation (Sheriff, 1975); consequently, dry holes continue to be drilled on bright spots which are not associated with gas deposits. Considerable research has been dedicated to follow up bright spots technology developed in the last decade.

One approach is to determine lithology and pore fluid from analysis of offset dependence of reflection amplitude data, which is available in common-depth-point (CDP) gathers (Ostrander, 1982; Gassaway and Richgeis, 1983; Almoghrabi and Lange, 1983; Backus, 1983; Ostrander, 1984; Gassaway et al, 1986). The basic concept behind this technique is that offset-dependent reflectivity is a function of p-wave velocity, s-wave velocity, and density contrasts between two media. Ostrander (1982) pointed out that "gas sands which produce a seismic bright spot, will generally produce gas saturation when there is no anomalous amplitude in the

equivalent s-wave event. If the s-wave section shows a bright spot, the p-wave anomalies are related to lithology and do not reveal any hydrocarbon accumulation. Robertson and Prichett (1985) applied these observations to three case histories of gas producing zones and concluded that 's-wave section can validate p-wave amplitude anomalies attributed to gas saturation'.

The above approaches are only valid if the reflecting system is a single interface or so thick that multiples do not interfere with primary reflections. The discrepancy of results found by Ostrander and Gassaway (i.e. whether or not gas-bearing sands is the only geologic configuration that results in an increase of amplitude with offset) provides an insight to the problem of uniqueness in inverting seismic data. Since it is difficult to handle the complex geology involved in the real structure, it is necessary to develop seismic models to examine the correlation between signal characteristics and elastic parameters of the model in a controllable manner.

The concept of correlation between seismic character and geologic features has been used by geophysicists since the beginning of exploration. Various numerical modeling techniques have been described and used to characterize geologic sections based on recognition of significant changes in the seismic character (Almoghrabi and Lange (1986); Dedman et al, 1975; Neidell et al, 1977; Sengbush, et al, 1961; Wuenschell, 1960). Neidell and Poggiagliolmi

discussed the importance of seismic modeling in stratigraphic studies and the utilization of seismic amplitudes and waveforms in the quantitative analysis of thin stratigraphic reservoirs.

The application of complex trace analysis to evaluate resolution of thin beds has been studied by Widess (1973); De Voogd and Den Rooljen (1983); Robertson and Nogami (1984); and Lange and Amoghriabi (1986). Widess (1973) determined the limit of thickness resolution as $1/8$ the dominant wavelength of the incident wavelet. He also discussed the linear response of thin layer to a vertically incident seismic pulse. However he neglected the influence of internal multiples. Koefoed and De Voogd (1980) showed that the contribution of multiples becomes more significant for increasing values of the reflection coefficient and provided limits to the linear response of thin layers.

A common constraint is that in most cases, analysis is limited to layers with enough thickness for the reflected signal to be resolved. When the thickness is so small [less than the tuning thickness (Kallaweit and Wood, 1982)] resolution of the signal in the time domain is not possible and information is encoded in the amplitude and shape of the signal. This leaves an open field for the searching of other seismic characters to investigate thin layers.

CHAPTER II

NUMERICAL METHOD

Modeling Procedure and Input Parameters

In this study, a model containing three materials is used to generate synthetic seismic traces for a Ricker wavelet reflecting from thin lithological units. The numerical results are obtained using forward seismic modeling following the algorithm shown in Figure 2. The input parameters of the seismic model include the thin layer thickness, the wave velocities, and the bulk densities of the three lithological units. The reflection coefficients at each interface are determined for a plane monochromatic wave using Zoeppritz coefficients. Subsequently, the layer reflectivity $R(f)$ is found for the specified frequency, using reflection amplitudes and relative phases of the wave components, as well be discussed in the following sections.

The input signal is expanded into its Fourier components using the fast Fourier transform (FFT) technique (Brigham; 1974). Each frequency component of the Fourier spectrum experiences a different reflectivity. The impulse response of the system $W(f)$, is determined from the product of the layer reflectivity $R(f)$ and the Fourier transform of the incident signal $X(f)$, i.e.

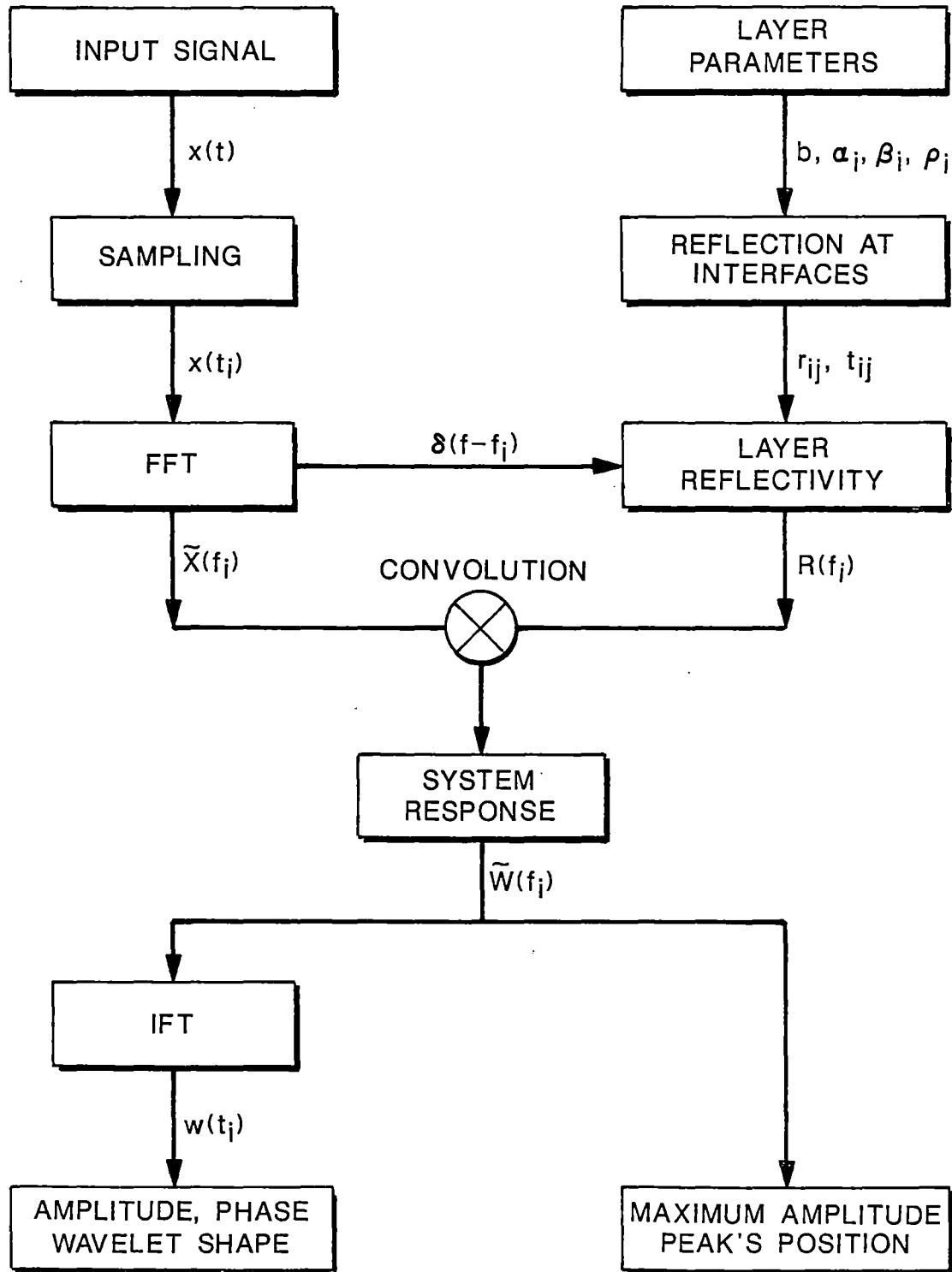


Figure 2 Schematic Diagram of Modeling Procedure

$$W(f) = R(f) X(f) \quad (1)$$

The seismic trace $w(t)$ is the real part of the complex function of time (Taner et al., 1979). which is found by applying the inverse Fourier transform (IFT) to the frequency spectrum of the output signal $W(f)$, i.e.

$$w(t) = \text{Re} \int_{-\infty}^{\infty} e^{i2\pi ft} W(f) df \quad (2)$$

The variation of both, the frequency and time domain responses as the layer parameters are changed is of particular interest in this investigation.

Reflection of Plane Waves at a Single Interface

Wave Propagation

The seismic method utilizes wave propagation through the earth to get an inference of the physical properties of the subsurface formation. The physics of wave propagation in solids is quite complex since two modes of elastic waves can exist simultaneously. These two types of waves (longitudinal and transverse) are referred to as pressure (P-) waves and shear (S-) waves. When either wave is reflected obliquely from an interface of two solids, the other type must be generated upon reflection (Ewing et. al., 1957) to satisfy the boundary conditions. The boundary conditions include continuity of wave fronts (Huygaen's principle) which leads to the generalized Snell's Law; and

continuity of normal and tangential components of the displacements and stresses vector, which leads to the solution of reflection coefficients.

The purpose of this section is to discuss briefly reflection coefficients for an incident plane wave. The reader is referred to Almoghrabi (1983) for further details.

Using Helmholtz separation method (Aki, 1980) the displacement vector \bar{x} can be expressed as

$$\bar{x} = \bar{\nabla}\phi + \bar{\nabla} \times \bar{\Omega}; \bar{\nabla} \cdot \bar{\Omega} = 0 \quad (3)$$

where $x = (u, v, w)$ is the elastic displacement

ϕ is a scalar potential associated with the P-wave,

$\bar{\Omega}$ is a vector potential associated with the S-wave.

If the S-wave is polarized purely as SV and the wave propagation is in the X-Z plane, then the general SV-wave can be expressed in terms of the potential $\bar{\Omega} = (0, \psi, 0)$, with displacement $\bar{\nabla} \times \bar{\Omega} = (-\frac{\partial \psi}{\partial z}, 0, \frac{\partial \psi}{\partial x})$.

For a P-wave propagating in the X-Z plane, it can be expressed in terms of a potential $\phi = \phi(x, z, t)$ (independent of the y-coordinate), with displacement

$$\bar{\nabla}\phi = \left(\frac{\partial \phi}{\partial x}, 0, \frac{\partial \phi}{\partial z} \right)$$

The advantage of using potentials (ϕ and Ω) for elastic displacement is that they can be used to separate P- and S-components and they satisfy the following wave equations:

$$\frac{\partial^2 \phi}{\partial t^2} = \alpha^2 \nabla^2 \phi$$

$$\frac{\partial^2 \psi}{\partial t^2} = \beta^2 \nabla^2 \psi \quad (4)$$

where α and β are the P-wave and the S-wave velocities respectively.

When a seismic wave (P-wave or S-wave) encounters a discontinuity in the elastic properties, as when it arrives at a surface separating two beds, part of the energy is reflected and part of it is refracted, the balance of the energy is transferred to the other wave type (S-wave or P-wave). The direction of wave propagation for the reflected and refracted waves is governed by the generalized Snell's law, which can be derived as a result of requiring that the projections of the wave fronts on the interface travel with the same phase velocity C stated as

$$C = \frac{\alpha'}{\sin \theta_p} = \frac{\beta'}{\sin \theta_s} = \frac{\alpha'}{\sin \theta_p'} = \frac{\beta'}{\sin \theta_s'}$$

where θ_p , θ_s , θ_p' , and θ_s' are angles of reflected and refracted P-waves and S-waves as shown in Figure (3). Reflection coefficients are found by applying the boundary conditions at the surface of discontinuity.

The steady-state plane wave solutions to the wave equations in a homogenous medium (Aki, 1980) take the form $A \exp[i(k \cdot x - \omega t)]$, where A is the wave potential amplitude.

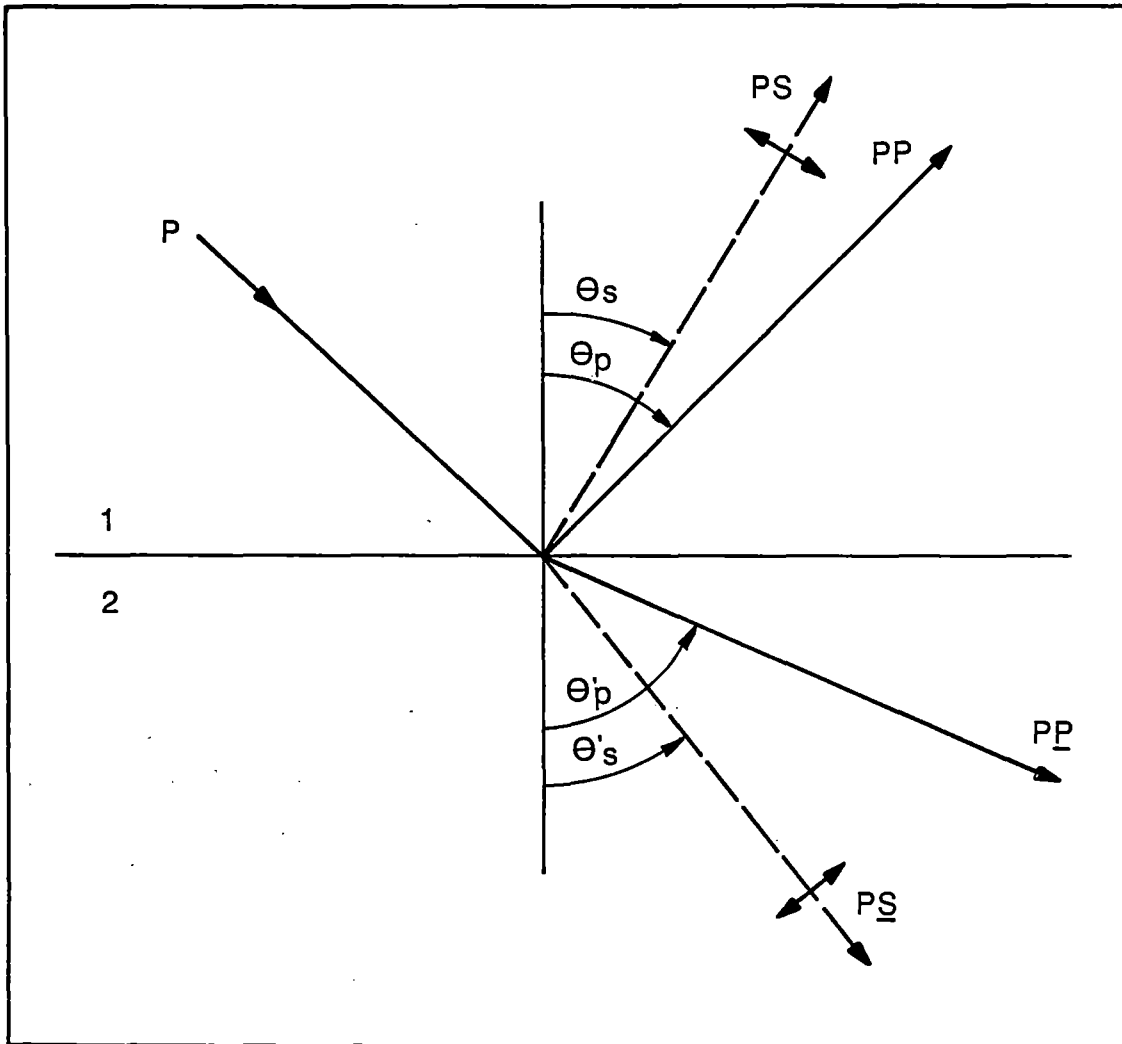


Figure 3 Rays which are reflected, transmitted, and mode-converted from a plane interface of two solids.

Knott's equations are obtained by solving the following displacement potentials:

in medium (1) i. e., $z < 0$:

$$\phi^- = A_0 e^{-i(k_{px} X - k_{pz} Z)} + A_1 e^{-i(k_{px} X + k_{pz} Z)},$$

$$\psi^- = B_0 e^{-i(k_{sx} X - k_{sz} Z)} + B_1 e^{-i(k_{sx} X + k_{sz} Z)}$$

and in medium (2) i. e., $z > 0$:

$$\phi^+ = A_2 e^{-i(k'_{px} X - k'_{pz} Z)},$$

$$\psi^+ = B_2 e^{-i(k'_{px} X - k'_{sz} Z)}.$$

where $k_p = \frac{w}{\alpha}$, $k'_p = \frac{w}{\alpha'}$, $k_s = \frac{w}{\beta}$, and $k'_s = \frac{w}{\beta'}$. (5)

It should be noted that the time factor, $e^{i\omega t}$, has been omitted from the above expressions for ϕ^\pm and ψ^\pm

Boundary Conditions

The first boundary condition requires the continuity of normal components at the surface, that is at the interface, $z=0$.

$$w^- = w^+; \text{ where } w = \frac{\partial \phi}{\partial z} + \frac{\partial \psi}{\partial x}$$

hence

$$(A_0 - A_1) \cot \theta_p - (B_0 + B_1) = A_2 \cot \theta'_p - B_2. \quad (6)$$

The next condition is that the tangential displacements be equal at $z=0$:

$$u^- = u^+; \text{ where } u = \frac{\partial \phi}{\partial x} - \frac{\partial \psi}{\partial z}$$

$$\text{or } (A_0 + A_1) + (B_0 - B_1) \cot \theta_s = A_2 + B_2 \cot \theta'_s. \quad (7)$$

the continuity of normal stresses requires that at the

interface $z = 0$ $\sigma_{zz}^- = \sigma_{zz}^+$,
 where $\sigma_{zz} = \lambda \nabla^2 \phi + 2\mu \left(\frac{\partial^2 \phi}{\partial z^2} + \frac{\partial^2 \psi}{\partial x \partial z} \right)$
 and λ, μ are lame's constants.

After simplification it becomes

$$\begin{aligned} & \mu_1 (\cot^2 \theta_s - 1) (A_0 + A_1) - 2\mu_1 (B_0 - B_1) \\ & = \mu_2 (\cot^2 \theta'_s - 1) A_2 - 2\mu_2 B_2 \cot \theta'_s \end{aligned} \quad (8)$$

continuity of the tangential stress implies that at $z = 0$

$$\begin{aligned} \sigma_{xz}^- &= \sigma_{xz}^+, \text{ where} \\ \sigma_{xz} &= \mu \left(2 \frac{\partial^2 \phi}{\partial x \partial z} + \frac{\partial^2 \psi}{\partial x^2} - \frac{\partial^2 \psi}{\partial z^2} \right) \end{aligned}$$

so

$$\begin{aligned} & \mu_1 \{ 2(A_0 - A_1) \cot \theta_p + (B_0 + B_1) (\cot^2 \theta_s - 1) \} \\ & = \mu_2 \{ 2A_2 \cot \theta'_s + B_2 (\cot^2 \theta'_s - 1) \}. \end{aligned} \quad (9)$$

It seems that there are four equations and six unknowns; however, there is one type of incident wave at a time and reflection coefficients can be normalized to the incident amplitude.

Incident P-wave

When a P-wave is incident at an interface of two solids ($B_i = 0$) the above equations (6-9) can be expressed in a matrix form as

$$\begin{bmatrix} a & a' & 1 & -1 \\ 1 & -1 & -b & -b' \\ \mu C & -\mu' C' & 2\mu b & 2\mu' b \\ 2\mu a & 2\mu' a' & -\mu C & \mu' C' \end{bmatrix} \begin{bmatrix} A_1 \\ A_2 \\ B_1 \\ B_2 \end{bmatrix} = A_0 \begin{bmatrix} a \\ -1 \\ -\mu C \\ 2\mu a \end{bmatrix}$$

where

$$\begin{aligned} a &= \cot\theta_p & , & \quad a' = \cot\theta'_p \\ b &= \cot\theta_s & , & \quad b' = \cot\theta'_s \\ c &= b^2 - 1 & , & \quad c' = b'^2 - 1 \end{aligned}$$

$$\text{and } \mu = \rho\beta^2 \quad , \quad \mu' = \rho'\beta'^2 \quad (10)$$

Solving the matrix equation leads to the reflection coefficients for the potential fields relative to the incident P-wave amplitude.

Noting that if the incident angle θ_p exceeds critical angles, Snell's law leads to imaginary angles. Consequently, some of the coefficients (a' , b' , c') become pure imaginary which leads to complex reflection coefficients.

Incident S-wave

When an S-wave is incident at an interface of two solids ($A_i=0$), using the above definitions, the boundary-condition equations can be expressed in a matrix form as

$$\begin{bmatrix} a & a' & 1 & -1 \\ 1 & -1 & -b & -b' \\ \mu C & -\mu' C' & 2\mu b & 2\mu' b' \\ 2\mu a & 2\mu' a' & -\mu C & \mu' C' \end{bmatrix} \begin{bmatrix} A_1 \\ A_2 \\ B_1 \\ B_2 \end{bmatrix} = B_0 \begin{bmatrix} -1 \\ -b \\ -2\mu b \\ \mu C \end{bmatrix} \quad (11)$$

Solving this matrix equation, which differs from the previous P-matrix equation (10) by the right hand side only,

leads to the reflection coefficients for the potential fields relative to the incident S-wave amplitude.

Partitioning of Energy

The disturbance caused by travelling waves induces the particles of the medium to possess both types of energy (kinetic and potential). Since the displacement is harmonic, the total energy can be found using maximum potential energy or the maximum kinetic energy. The total mechanical energy per unit volume then is

$$E_T = E_{K \max} = \frac{1}{2} (\dot{u}_{\max}^2 + \dot{w}_{\max}^2). \quad (12)$$

The energy densities for seismic waves are as follows:

$$\begin{aligned} \text{incident P-wave} \quad E_0^{(P)} &= \frac{1}{2} \rho \frac{\omega^4}{\alpha^2} A_0 \\ &= \frac{1}{2} \rho \omega^2 a_0 \end{aligned}$$

$$\begin{aligned} \text{incident S-wave} \quad E_0^{(S)} &= \frac{1}{2} \rho \frac{\omega^4}{\beta^2} B_0 \\ &= \frac{1}{2} \rho \omega^2 b_0 \end{aligned}$$

$$\begin{aligned} \text{reflected P-wave} \quad E_1^{(P)} &= \frac{1}{2} \rho \frac{\omega^4}{\alpha^2} A_1 \\ &= \frac{1}{2} \rho \omega^2 a_1 \end{aligned}$$

$$\begin{aligned}
\text{reflected S-wave } E_1^{(S)} &= \frac{1}{2}\rho \frac{\omega^4}{\beta^2} B_1 \\
&= \frac{1}{2} \rho \omega^2 b_1 \\
\text{refracted P-wave } E_2^{(P)} &= \frac{1}{2} \rho \frac{\omega^4}{\alpha^2} A_2 \\
&= \frac{1}{2} \rho \omega^2 a_2 \\
\text{refracted S-wave } E_2^{(S)} &= \frac{1}{2} \rho \frac{\omega^4}{\beta^2} B_2 \\
&= \frac{1}{2} \rho \omega^2 b_2
\end{aligned} \tag{13}$$

where $a_i = \left(\frac{\alpha_i}{\omega} A_i\right)$, $b_i = \left(\frac{\beta_i}{\omega} B_i\right)$, $i=0,1,2$

represent the displacement amplitudes, which when used instead of potential amplitudes in Knot's equations provide Zoeppritz equations.

Applying conservation of energy per unit area per unit time along the z-direction yields the following equation:

$$\begin{aligned}
\frac{1}{2} \rho \frac{\omega^4}{\alpha} \cos \theta_p A_o^2 &= \frac{1}{2} \rho \frac{\omega^4}{\alpha} \cos \theta_p A_1^2 + \frac{1}{2} \rho \frac{\omega^4}{\alpha} \cos \theta_p A_2^2 \\
&+ \frac{1}{2} \rho \frac{\omega^4}{\beta} \cos \theta_s B_1^2 + \frac{1}{2} \rho \frac{\omega^4}{\beta} \cos \theta_s B_2^2 ;
\end{aligned} \tag{14}$$

or by normalizing the energies w.r.t the incident energy it is reduced to

$$1 = \xi_1^2 + \xi_2^2 + \eta_1^2 + \eta_2^2$$

where $\xi_1 = A_1/A_0$ the square root energy of the reflected P-wave

$$\xi_2 = \sqrt{\frac{\rho'}{\rho} \frac{\alpha}{\alpha} \frac{\cos\theta'}{\cos\theta_p}} \quad \frac{A_2}{A_0} \quad \text{for the refracted P-wave}$$

$$\eta_1 = \sqrt{\frac{\alpha}{\beta} \frac{\cos\theta_s}{\cos\theta_p}} \quad \frac{B_1}{B_0} \quad \text{for the reflected S-wave}$$

$$\eta_2 = \sqrt{\frac{\rho'}{\rho} \frac{\alpha}{\beta} \frac{\cos\theta_s'}{\cos\theta_p}} \quad \frac{B_2}{B_0} \quad \text{for the refracted S-wave} \quad (15)$$

Reflection of a Plane P-wave From a Single Layer

Wave-sum Technique

The model calculation uses a plane p-wave which is incident on a layer whose thickness is in the range of a fraction of the wavelength typical of seismic circumstances. The net return wave reflected from the layer is determined by adding all of the wave components in a vector summation, i.e. amplitude and phase. This return amplitude represents the interference of the waves reflected from the top and the bottom of the layer as well as contributions due to mode converted waves at each of the interfaces. Because the net

wave amplitude is a result of interference, the frequency and layer thickness are important parameters in determining the net reflection of the layer.

The amplitude of the reflected signals is determined by solving the boundary value problem associated with the continuity of the components of the stress, the displacements, and the wave fronts across the plane interface which is the boundary between the three rock layers. The incident wave is monochromatic and the layer contains two parallel, planar interfaces. The solution to the boundary value problem results in the reflection amplitudes which are expressed in terms of the so-called Zoeppritz coefficients. These coefficients relate the amplitude of the reflected wave to that of a unit amplitude incident wave. The boundary value problem leads to mode conversion in which the incident wave is converted to a second wave type upon reflection and transmission through the interface. This can be explained by referring to equations (6) and (7) where both types of wave contribute to the displacement. These mode converted waves can play an important role in reconstructing the net emerging wave, particularly for larger angles of incidence. The geometry for the boundary value problems is illustrated in Figure 3. The incident wave is a plane pressure wave which encounters the layer at an angle θ_p with respect to the normal to the boundary interface. The p-wave reflected from the top layer is referred to as the primary reflection and is indicated by

PP in this diagram. In addition to the p-wave that is reflected, a shear wave (PS) is generated upon reflection which makes an angle θ_s less than the incident angle as it propagates in the upper medium. The transmitted wave consists of a transmitted p-wave and a mode-converted s-wave (PS).

The net reflected wave amplitude can be represented symbolically in terms of transmission coefficients T and reflection coefficients R determined from the boundary value problem. The amplitude of the reflected wave is a product of the incident amplitude multiplied by the reflection coefficient R, while the amplitude of the transmitted wave is T times the incident amplitude. The physical parameters characterizing the three materials are the pressure wave velocity α , the shear wave velocity β , and the density of the material. The subscripts associated with these quantities indicate the material with which these values are associated.

The net reflected signal of the layer involved individual ray reflections from two plane parallel boundaries as illustrated in Figure 4. The boundary media are designated by numeral 1 for the upper material, referred to as the reflection zone, 2 for the layer material, and 3 for the lower bounding material or transmission zone. The net reflected wave of the layer involves two reflection problems: (i) from the upper planar interface between material 1 and 2, and (ii) the lower interface between

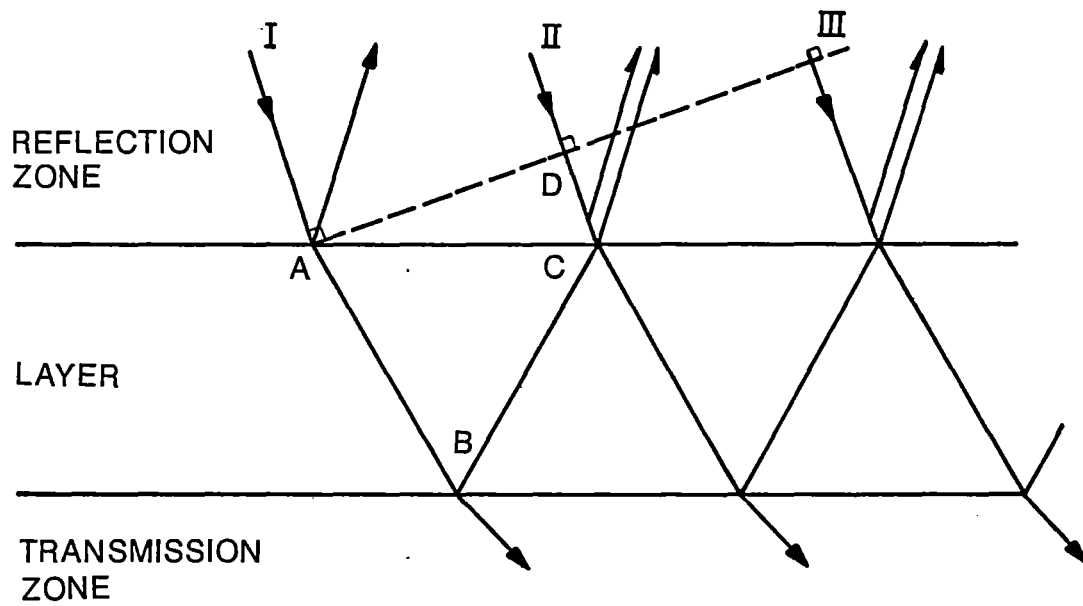


Figure 4 A diagram indicating the various paths taken by incident rays (I, II, III) which interfere with rays which are multiply reflected in the layer and emerge in the reflecting zone. No mode-converted waves are shown for simplicity.

material 2 and 3. The reflection and transmission coefficients for these two interfaces are designated by subscripts which indicate the media from which the wave initially travels, with the second subscript indicating the media in which the wave is either reflected from or transmitted through. Thus, T_{12} is a transmission coefficient for a wave that is initially in layer 1 and emerges in layer 2, while T_{21} is a transmission coefficient for a wave that is initially in layer 2 which emerges into material 1. It is necessary to designate this order since waves that reflect from the interface bounding materials 2 and 3 are important contributions to the net reflected wave in medium 1. The second interface 2, 3 is also a means of changing initially mode converted shear waves back to p-waves. The multiple reflections of the waves within layer 2 leads to multiple conversions from one wave type to the other. The numerical solution to the boundary value problem is outlined in standard texts such as Ewing et. al (1957). The resulting reflection and transmission coefficients are used in a wave sum to determine the net wave reflected from the layer.

As an approximation to the final sum, let us first consider the interference of the multiples which are reflected within layer 2 and the primary wave reflected from the interface between 1 and 2. Assuming the incident amplitude is A_I , the primary reflected wave amplitude is A_I times R_{12} . The wave transmitted through that first

interface is A_I times T_{12} , while the wave reflected at the interface between 2 and 3 is $A_I T_{12} R_{23}$. This wave then is incident on the interface between 2 and 1 where the emerging wave has an amplitude $A_I T_{12} R_{23} T_{21}$. The emerging multiple has traveled a different path length in the layer than has the primary reflected ray with which it interferes. The paths are indicated in Figure 4. The geometric phase shift between the two rays is determined by the difference in path length from an initial point at which both rays are in phase. This initial point is indicated by the dashed wavefront in the diagram. The path difference is determined from the length traveled, ABC, by the primary reflection, compared to the length traveled DC, by the multiple. The geometric phase shift is given by

$$\zeta = 4\pi \frac{b \alpha_1}{\lambda \alpha_2} \sin \theta_2 \quad (16)$$

where α_1 and α_2 are velocities of the reflection zone and layer, λ is the incident wavelength, and θ_2 is the angle of refraction. The emergence of this first multiple interferes with ray 2 in Figure 4, but part of the energy is reflected at interface 2,1 and additional multiples are generated in the layer which emerge further down with offset. These multiples interfere with other rays which are part of the original wavefront defined by the dashed line. The amplitudes of the multiples are determined from the application of reflection and transmission coefficients at

each of the interfaces. The amplitude of the nth multiple A_n is given by

$$A_n = T_{12} T_{21} R_{23}^n R_{21}^{n-1} A_I \quad (17)$$

where A_I is the amplitude of the incident wave. A combination of the multiples at a fixed point on the interface leads to an interference pattern between the primary reflection and the multiples as they arrive at that particular point and yields the net reflected wave from the interface. The net reflected amplitude is given by

$$A_R = A_o + \sum_n A_n \cos(n\zeta) \quad (18)$$

where the zero reference phase is assumed to occur at the point of interference at the interface 1,2. This is a vector sum over the amplitudes of the wave arriving at that point and their phases. In addition, there are waves which result from mode conversion at both the top and bottom interface and are reconverted back to the initial wavetype and add to the wave sum (Meissner and Meixner, 1969). The geometric phase difference between the primary reflected wave and either the multiples or the mode converted waves can be written, in general, as

$$\zeta = \frac{2\pi b}{\lambda} \left[\frac{v}{v'} \sin\theta' + \frac{v}{v''} \sin\theta'' \right] \quad (19)$$

where b is the thickness of layer, λ the wavelength, θ' , θ'' the incident and refracted angles and v , v' , v'' are determined by the type of wave traveling in the layer. If the wave is a multiple of the incident p-wave, then v is equal to α_1 . If the wave results from mode conversion in

the layer, i.e. an incident p-wave, a transmitted p-wave, a mode converted s-wave, and then an emergent p-wave, then V is equal to α_1 , V' is equal to α_2 and V'' is equal to β_2 . By combining the various multiples combinations we obtain a list (Table 1) of the relationship between the type of propagation in the layer and the designation for the parameters V , V' , and V'' for various mode converted combinations.

Multiple Waves

The emerging amplitude given by the infinite sum in equation 18 can often be approximated by a finite number of terms. The amplitude of the multiple A_n can decrease significantly as energy is radiated into the region above and below the layer. The decrease in the amplitude of ensuing terms allows the infinite series to be terminated approximately with a finite number of terms. As an example of the multiples as a function of the angle, a series of material values were chosen to numerically evaluate the amplitude of each multiple. The types of material parameters assigned to the layer and its surroundings are listed in Table 2. In Figure 5, the amplitude of the multiples as a function of angle is shown on a logarithmic scale. The units are given in decibels. It is seen that the amplitude decreases quite rapidly as one gets beyond the second or third multiple. The separation between the multiples is constant at a fixed angle of incidence as the

TABLE I

THE GEOMETRIC PHASE SHIFT GIVEN BY EQUATION (19) DEPENDS ON THE WAVETYPE WHICH PROGAGATES IN THE LAYER. THE FIRST LETTER INDICATES THE MODE TYPE IN THE DOWNWARD DIRECTION AND THE SECOND IN THE UPWARD DIRECTION. THE LETTERS ARE UNDERLINED TO INDICATE THE WAVE IS TRAVLEING IN THE LAYER.

<u>Mode Type</u>	<u>V'</u>	<u>V''</u>
<u>PP</u>	α_2	α_2
<u>PS</u>	α_2	β_2
<u>SP</u>	β_2	α_2
<u>SS</u>	β_2	β_2

TABLE II

THE WAVE VELOCITIES AND DENSITIES OF VARIOUS MATERIALS USED IN THE NUMERICAL EVALUATION. THE VALUES ARE OBTAINED FROM THE LITERATURE GIVEN BY: (A) GREGORY ET. AL (1977), (B) ROSS (1984), (C) FERTIG AND MULLER (1978). THE DESIGNATIONS ARE USED TO INDICATE THE TYPE OF MATERIAL IN THE REFLECTION ZONE, THE LAYER, AND THE TRANSMISSION ZONE I.E. S(L)/GS/S(H) YIELDS A LOW VELOCITY SHALE LAYER ABOVE (REFLECTION ZONE), A GAS SATURATED LAYER, WHICH IS BOUNDED BELOW (TRANSMISSION ZONE) BY A HIGH VELOCITY SHALE.

<u>Type of rock</u>	<u>Designation</u>	<u>P-velocity</u> <u>(M/S)</u>	<u>S-velocity</u> <u>(M/S)</u>	<u>Density</u> <u>x10³ KG/M³</u>	<u>Poisson's</u> <u>Ratio</u>	<u>Source</u>
Gas sand	GS	2069	2045	1.92	0.100	a
Brine Sand	BS	3292	1908	2.21	0.247	a
Limestone	LS	4120	2260	2.25	0.285	a
Shale	S	3170	1585	2.36	0.333	b
Shale (L)	S(L)	2743	1372	2.29	0.333	
Shale (H)	S(H)	3414	1707	2.39	0.333	
Coal	CO	1998	1155	1.41	0.250	c

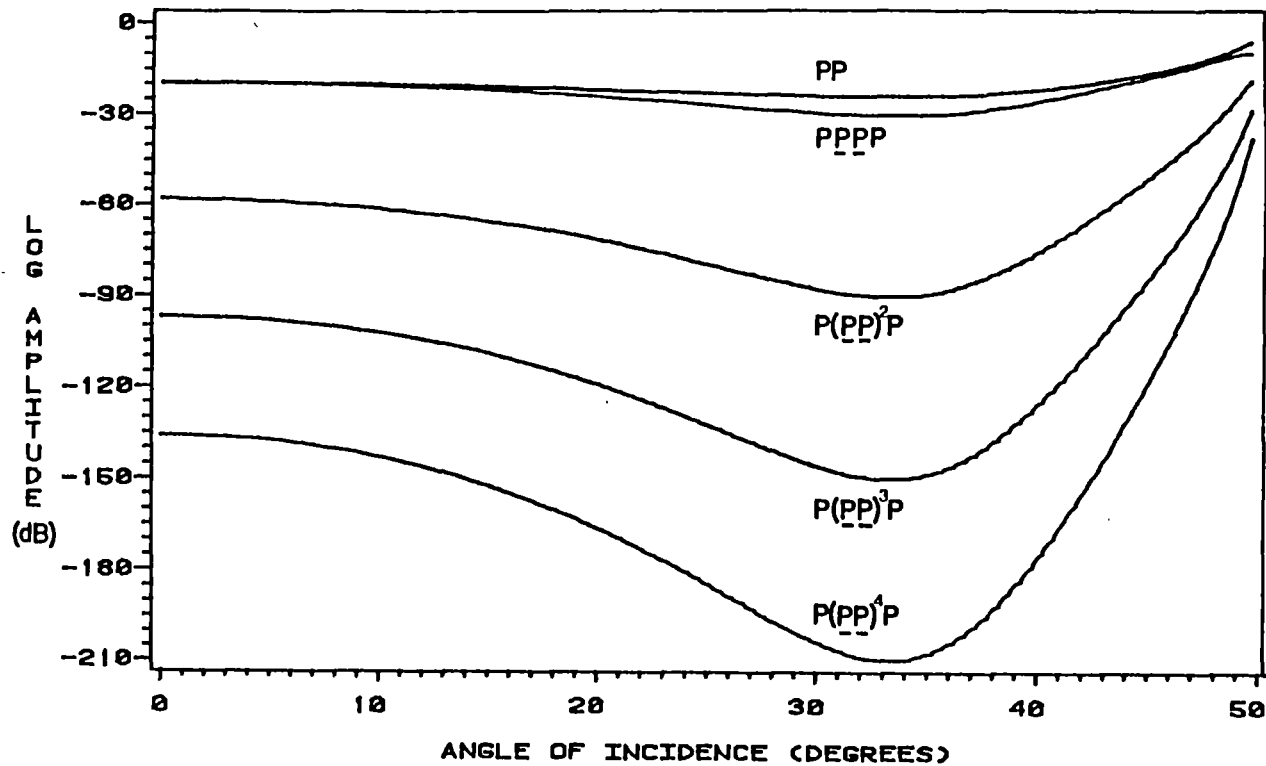


Figure 5 The amplitude of p-waves multiply reflected in the layer $[(S(H)/gs/s(H)]$ as a function of angle of incidence. A logarithmic scale is used to display the amplitude where the abscissa is in units of decibels $[(dB = 20 \cdot \log(A_n/A_1)]$.

energy leaks out of the layers. This leads to essentially exponential decay as the multiple propagates in the layer. This is not an absorption of energy, but rather energy being radiated into the half spaces above and below the layer. The large difference in amplitude between the multiples ranging up to 50 decibels for the brine sand, suggests that a limited number of terms is sufficient in the wave sum to obtain accuracy which is compatible with resolution of typical seismic data. The amplitude calculated from a finite wave sum is compared to the exact infinite sum in Figure 6 at normal incidence where no mode conversion occurs. The infinite sum can be written in closed form for normal incidence on the layer as

$$A_R = \frac{R_{12} + R_{23} e^{i\zeta}}{1 + R_{12}R_{23} e^{i\zeta}} \quad (20)$$

where R is the reflection coefficient and ζ is the geometric phase shift (Brekhovskikh, 1980). The wave sum of equation 18 rapidly approaches the exact infinite sum value after only a few terms (3 to 4). At non-normal incident angles, mode conversion generates other wavetypes and an exact solution in closed form is not available for comparison to the finite sum, however, the asymptotic value is still approached rapidly after only a few terms. The number of terms used is determined by the requirement that the finite sum be within 1.0% of the asymptotic value.

An independent way to verify the finite wave summation solution is to compare the total incident energy flux with

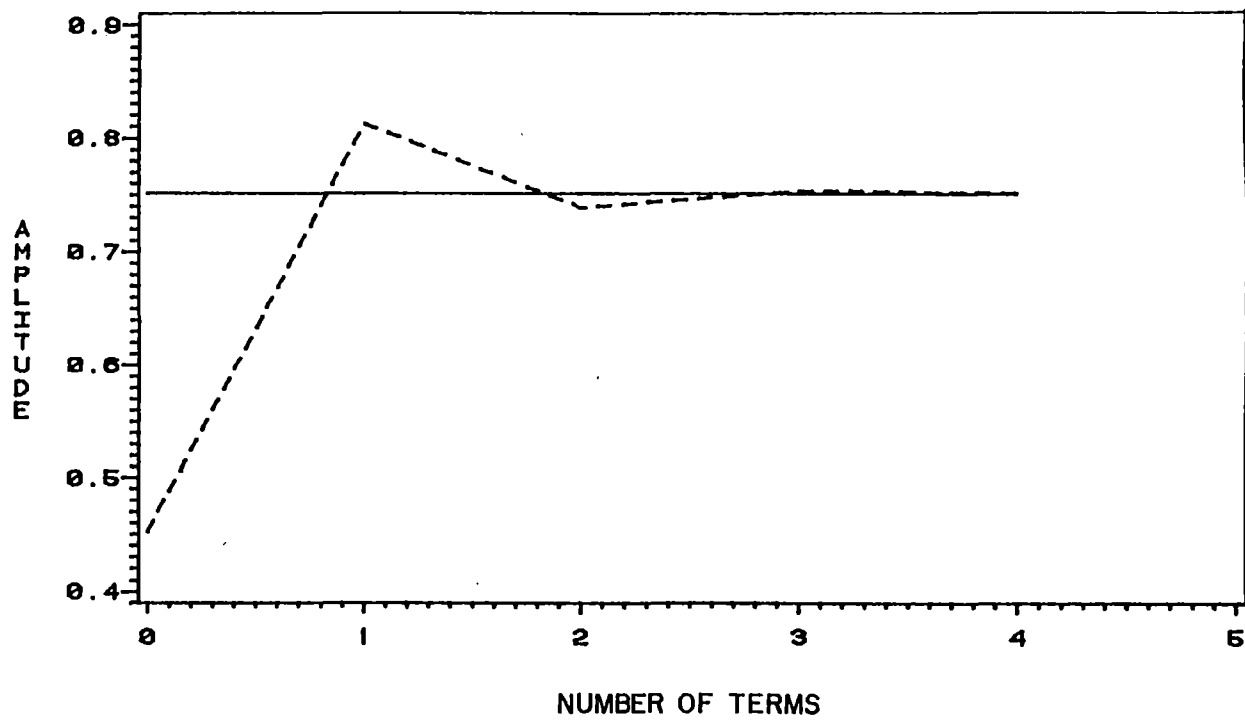


Figure 6 The finite wave sum (solid curve) compared to the exact solution at normal incidence as the number of terms is increased for a s/co/s layer.

the net reflected and transmitted energy to determine if overall energy conservation occurs in the calculation. In Figure 7, energy components are exhibited as a function of the incident angle. The upper curve is the sum of the energy components and approaches 1 (for a unit incident amplitude) to within 4% over the entire range of incident angles. The approximate conservation of the energy while using only four multiples of the p-wave and mode converted waves of the first multiple in the wave sum, verifies the accuracy of the wave sum technique and indicates the relative unimportance of many of the mode converted and multiply reflected components to the overall amplitude. It should be noted that net shear wave conversion is only significant at large angles near grazing or critical incident angles and that most of the energy is transmitted through the layer even for "bright spots".

Mode Converted Waves

Energy reflected from the interface or transmitted through the layer can be multiply converted from an incident p-wave to an s-wave. This s-wave travels at a different velocity and interacts with material in a unique manner. Since there are multiple reflections within the layer, the s-wave can be reconverted to a p-wave before emerging into the reflected zone. The s-wave may also remain an s-wave and emerge in an entirely different direction than the reflected p-waves. The mode converted waves then, are of

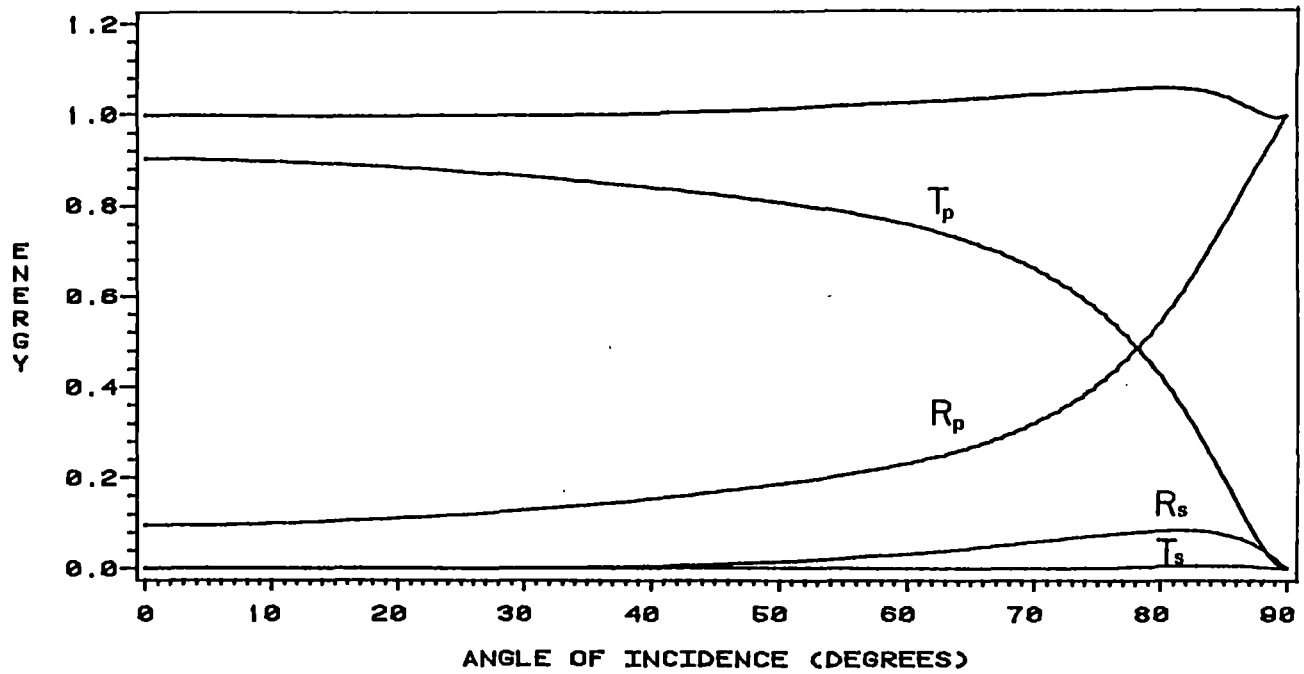


Figure 7 The energy flux of the total reflected, transmitted, and mode converted components as a function of incident angle. The energy flux is normalized to the incident energy flux.

two classes of interest in the reflected spectrum: those which are converted to s-waves and emerge from the layer as a distinct wavetype and those that are converted to s-waves and back to p-waves and emerge from the layer as a p-wave interacting with the primary reflected p-wave. The phase shifts for the mode converted waves are, of course, different from the multiply reflected p-waves in the layer and this factor must be included in the wave sum. The direction of propagation (ray) of the wave which is reconverted to a p-wave upon emission from the top surface, is the same as the reflected p-waves, while the directions of the s-waves that emerge from the top surface are the same as the top surface mode converted s-waves. The emergent, mode converted s-waves are considered separately in the following since their velocities and directions of propagation are substantially different from the p-wave field. The symbols used to designate the various unconverted, converted, and reconverted mode types are shown in Table 3.

The amplitude of the reconverted p-wave is the sum over amplitudes of the multiples that undergo initial conversion to s-waves (PSPP) or reflection conversion to s-waves (PPSP) and ultimate emission as a p-wave. The largest overall magnitude of the reconverted (SP or PS) p-wave occurs in the region near grazing incidence and is generally less than 25 decibels below the primary reflected p-wave (PP). In general, the reconverted p-wave that undergoes an s-p conversion in the layer (PSPP or PPSP) is of a larger

TABLE III

THE ABBREVIATIONS USED TO DESIGNATE THE TYPE OF WAVE AS IT PROPAGATES AND EMERGES FROM THE LAYER. A PLANE PRESSURE WAVE IS INCIDENT ON THE LAYER AND IS THE FIRST LETTER IN THE DESIGNATION. THE MODE TYPE IN EACH TRANSIT OF THE LAYER IS UNDERLINED.

<u>Designation</u>	<u>Explanation</u>
PP	Top surface, primary P reflection.
P(<u>PP</u>) ⁿ P	The n th p-wave multiple.
<u>P</u> SPP	A mode converted and sometimes reconverted wave which emerges as a p-wave after one transit reflection in the layer
<u>P</u> PSP	
<u>P</u> SSP	
<u>P</u> PPS	Mode converted waves which emerge as s-waves after one reflection in the layer.
<u>P</u> PSS	
<u>P</u> SSS	
<u>P</u> SPPS	
P(<u>SP</u>) ⁿ P	Examples of mode conversion for multiple transits in the layer.
P(<u>SPPS</u>)P	
P(<u>SPSS</u>)P	

magnitude than the wave which travels as an s-wave in the layer and is reconverted on transmission at the upper emerging surface (PSSP) (Figure 8). The (PSSP)-wave which propagates in the layer is typically 50-75 decibels below the p-wave reflectivity and is of negligible magnitude in this calculation. The mode converted s-p waves (PSPP and PPSP), however, have a magnitude which is significant compared to the primary p-wave, over a narrow angular range (approximately 10 degrees, for example, for limestone). The multiple sum of reflected p-waves undergo a minimum at large angles and the mode converted p-wave exceeds the magnitude of the multiple sum Eq (18) in this angular range. The mode converted s-p wave is then the major contribution to the emerging p-wave spectrum in a narrow range and is retained in the following calculations for at least two multiples.

The second type of mode converted wave emerges as an s-wave and is distinguishable because of its different travel time. The mode converted s-waves in the reflection zone are treated separately because of their different direction of emergence and velocity of propagation and are not included in the p-wave sum. The largest amplitude s-wave results from partial propagation as a p-wave in the layer and mode conversion to an s-wave on the bottom surface (PPSS) (Figure 9). The amplitude of the s-wave resulting from transmission from the original surface and propagation entirely as an s-wave in the layer (PSSS) is considerably less than the PS-wave. The maximum in the PS amplitude occurs at large

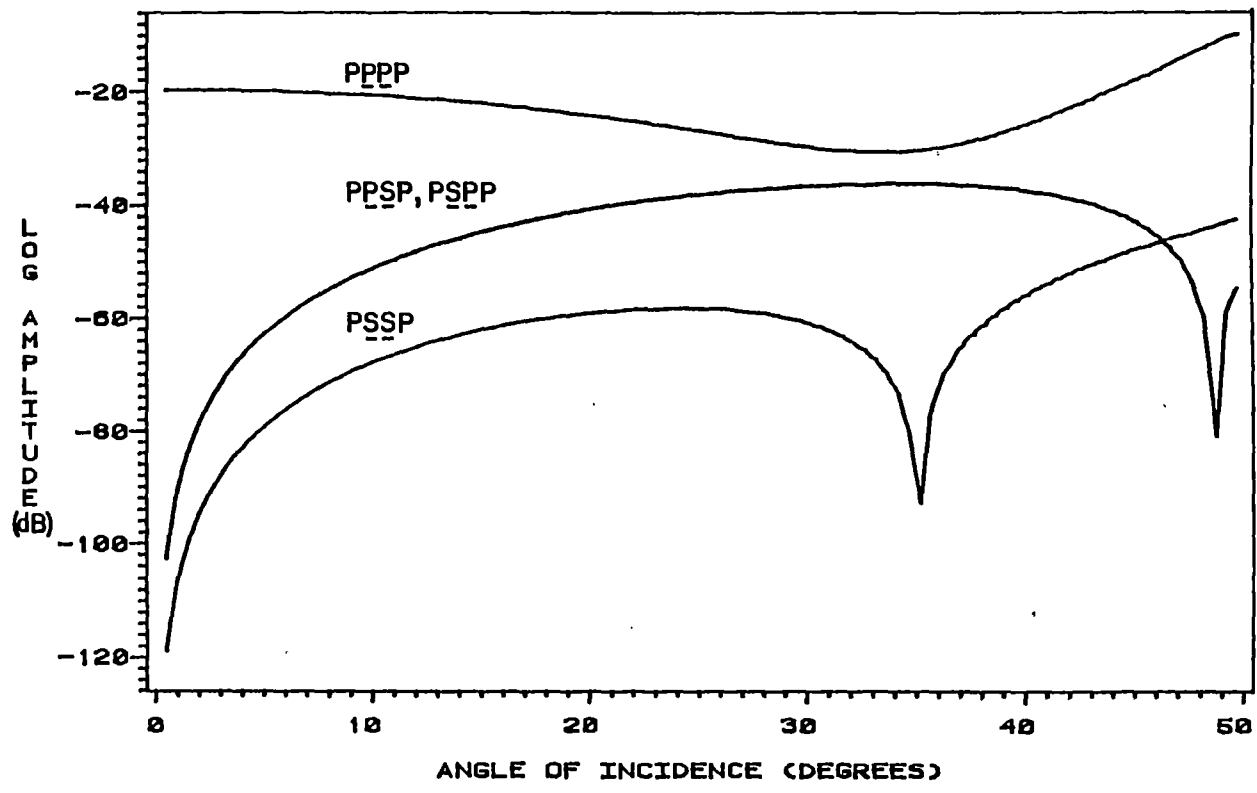


Figure 8 The amplitude of mode converted waves which emerge as p-waves from the layer. These waves have propagated as mode converted s-waves while in the layer and are reconverted to p-waves as they emerge (S/LS/S).

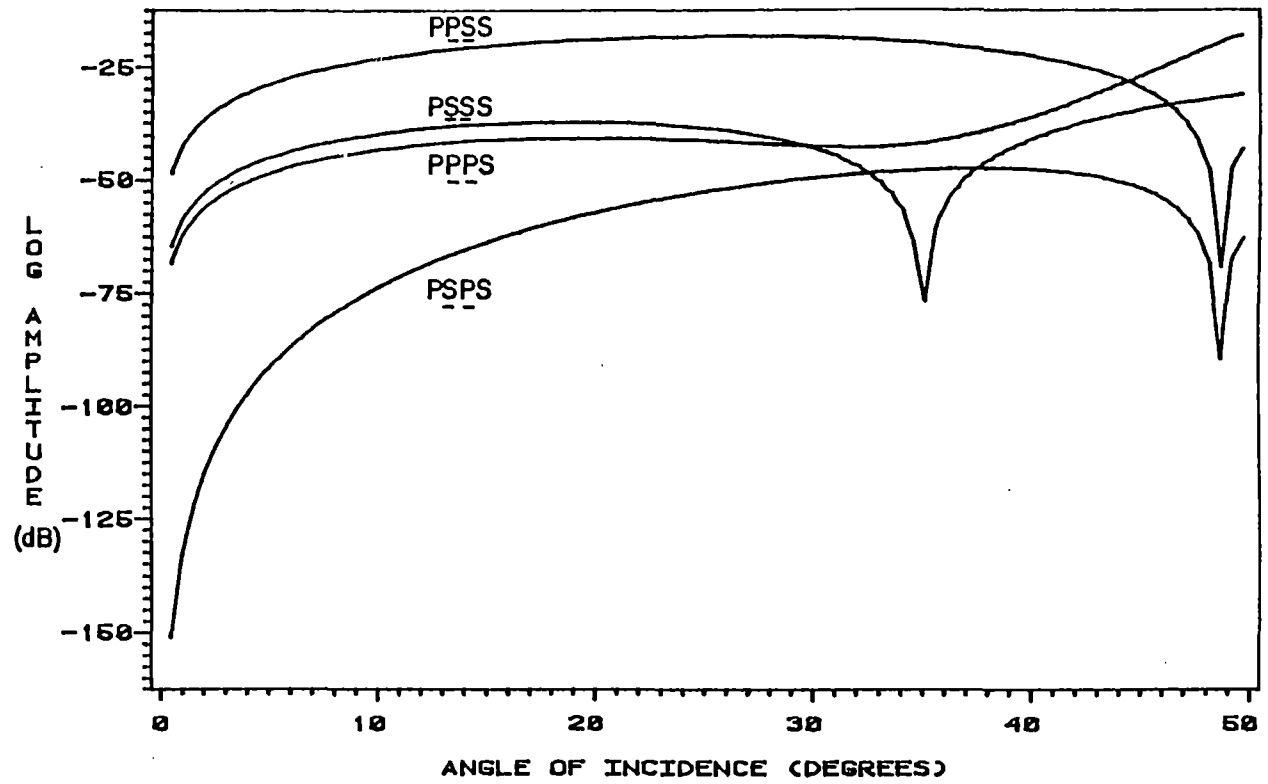


Figure 9 The amplitude of mode converted s-waves for various conversion sequences. The s-waves are emerging into the reflection zone (S/LS/S).

angles as ($\theta_p > 30^\circ$). The overall amplitudes of these mode converted s-waves vary considerably with the lithology and fluid saturation of the layer (Helbig and Mesdag, 1982 and Stumpel et. al 1984) and can be important indicators of the properties of the reflecting layer. In general, their amplitudes are small compared to the p-wave amplitude and therefore require special care in observation. Figures 8 and 9 show the amplitude of the mode-converted waves as a function of angle and are plotted as a function of the incident angle of the incoming p-wave. The angle of emission of the S-wave is determined by the relative S- to P-velocities of the top medium and is restricted to a much narrower range than the incident P-wave angles. Mode converted S-wave, in fact, emerge from the layer in a very narrow beam and can be displayed more readily in a polar directivity pattern which can be considered as an equivalent source distribution. The amplitude of the mode-converted S-wave as a function of the angle of propagation of its wave vector is shown in Figure 10. The amplitude is the length of the polar vector and the direction of propagation is the angle made with the horizontal axis. As seen from the polar plot, the converted S-wave occur in a very narrow angular region of the entire half-space of the reflected zone. Only a limited number of receivers are excited by an appreciable amplitude mode-converted S-wave. This narrow directivity is characteristic of all the materials considered in this investigation.

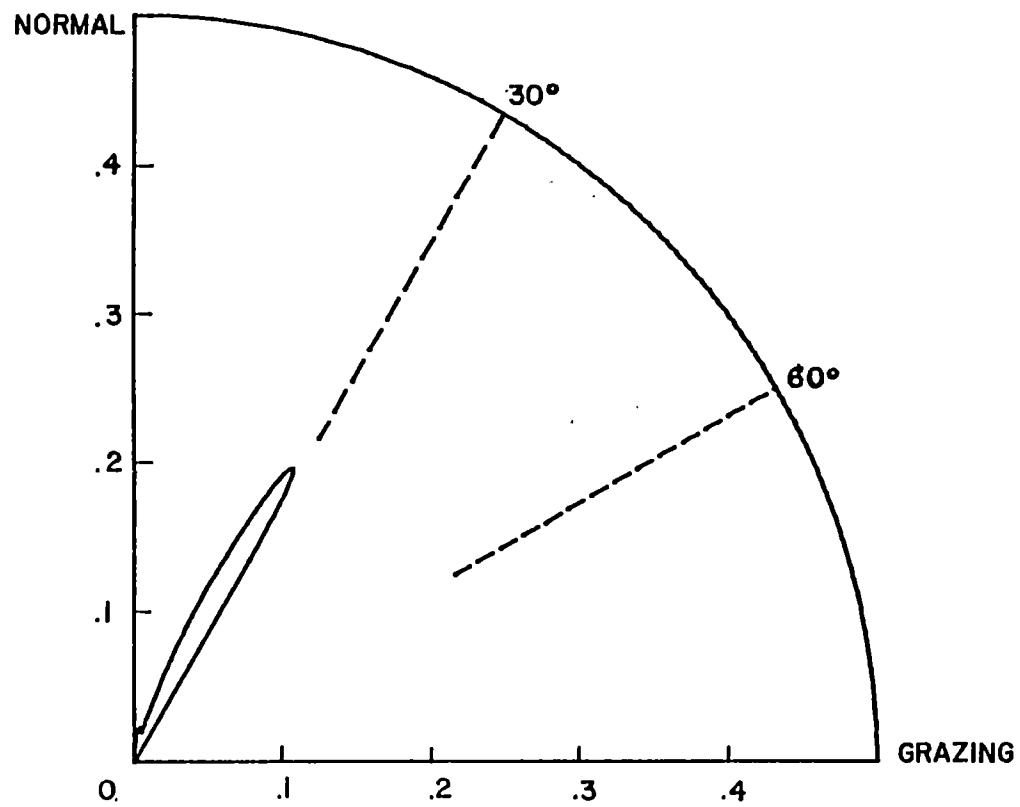


Figure 10 S-wave directivity patterns of their emergence into the reflection zone. The layer (S/GS/S) is one quarter of a wavelength thick.

Thin Layer Reflectivity to an Incident Impulse

In the previous section a wave sum technique was developed to evaluate layer reflectivity for a monochromatic wave when the thickness is varied within the range of the incident wavelength. The same reflectivity can be used to illustrate the frequency dependent of the layer reflectivity for a certain thickness. The thickness of the investigated layer ranges from 5 feet to 45 feet. The maximum thickness considered here is less than the thickness defined for thin beds (one eighth the dominant wavelength) as was pointed out by Widess (1973). The dispersive behavior of the reflectivity of a sandstone layer as the pore fluid is changed from gas to brine is shown in Figure 11 and Figure 12 respectively. The layer acts as a periodic filter function reflecting minimum energy at some frequencies where destructive interference occurs, and maximum energy at other frequencies where constructive interference occurs. The spectrum period F is related to the thickness of the thin layer b , the transmitted P-wave velocity α_2 , and the angle of incidence. At normal incidence $F = \alpha_2/2b$, and it increases with the angle of incidence. These diagrams exhibit the reflectivity function $R(f)$ in the frequency domain at each angle of incidence for a fixed layer thickness of 25 feet. The impulse response of the layer varies with pore fluid through the inclusion of the reflectivity in the system response function $W(f)$.

SHALE / GAS SAND / SHALE

THICKNESS = 25 FEET

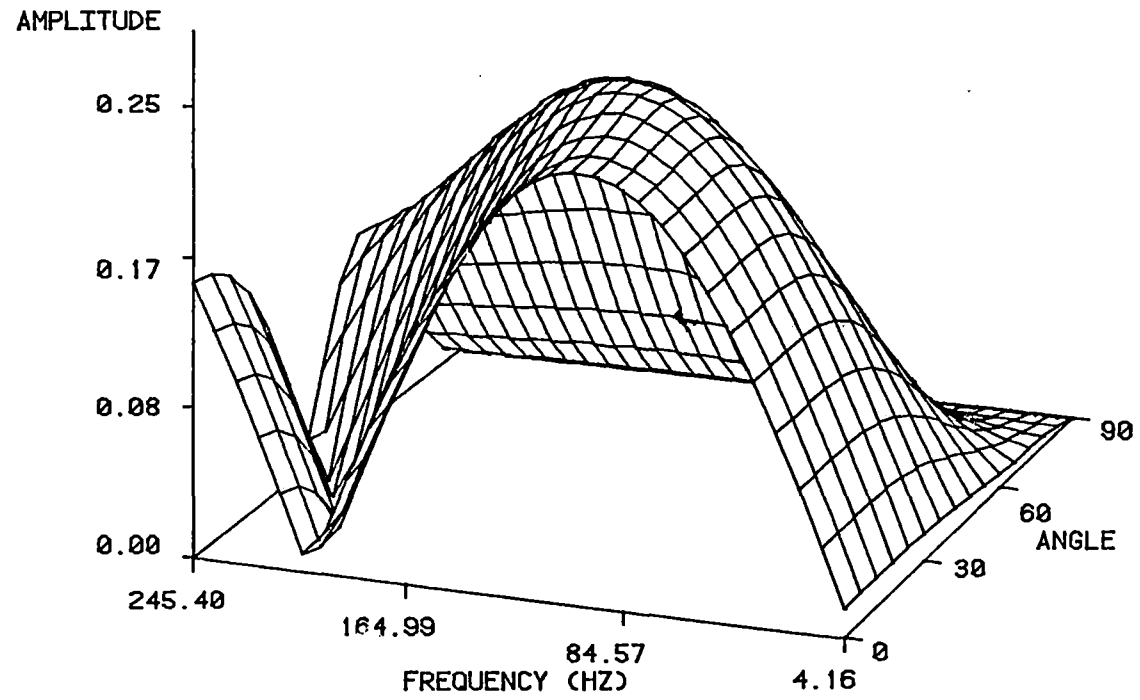


Figure 11 The frequency dependence of layer reflectivity versus angle of incidence.

SHALE / BRINE SAND / SHALE

THICKNESS = 25 FEET

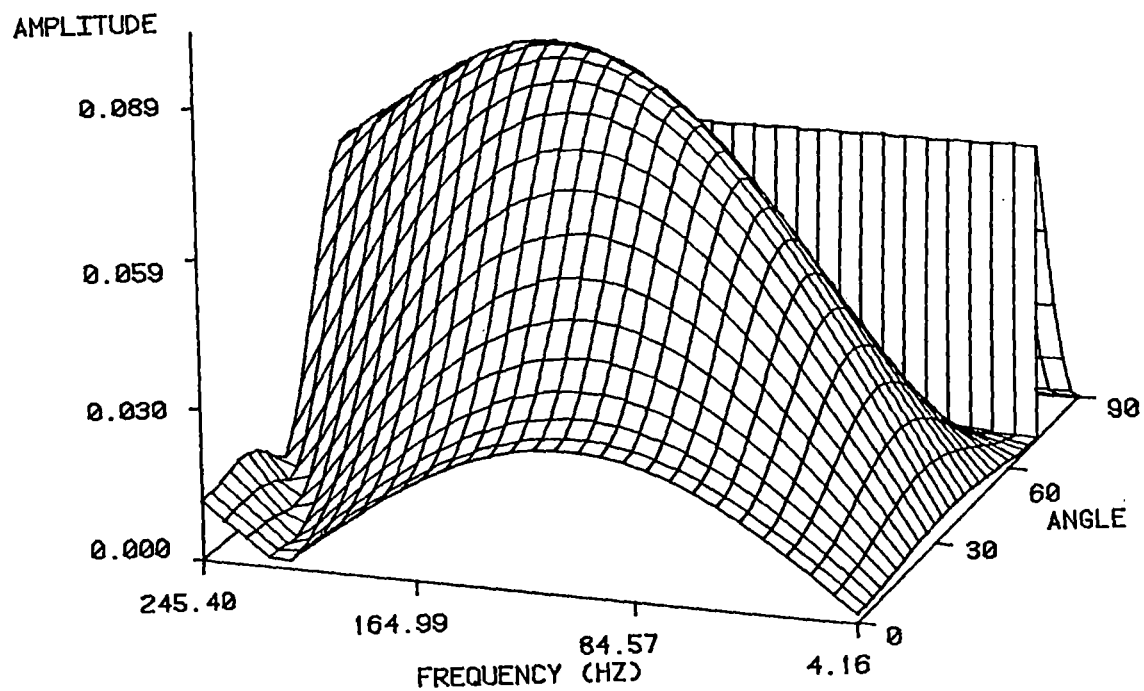


Figure 12 The frequency dependence of layer reflectivity as extended beyond the critical angle.

Input Signal

A 25 Hz zero-phase Ricker wavelet is used as an input for the numerical model. The analytical expression for the amplitude spectrum of the wavelet (Ricker, 1945) is

$$A(\xi) = \xi^2 e^{-\xi^2} \quad (21)$$

where $\xi = f/f_0$, and f_0 is the central frequency in Hz, i.e. corresponding to the maximum value of the spectrum which is chosen to be 25 Hz (Figure 13). The time amplitude expression for the above Ricker wavelet is

$$x(t) = [1 - 2(\pi f_0(t - t_0))^2] e^{-[\pi f_0(t - t_0)]^2} \quad (22)$$

The time shifted zero-phase Ricker wavelet has a unit amplitude at t_0 , which is chosen to be 80 msec as shown in Figure 14. The same Ricker wavelet is used as an input for all numerical results obtained.

The spectrum of the reflected wavelet is of particular importance in this investigation. To see how layer reflectivity causes a shift in the central frequency (frequency corresponds to the maximum amplitude in the frequency spectrum), let us consider the Fourier spectrum of the Ricker wavelet derivative. This is the impulse response for normal reflection from a thin layer encased in identical formations, where the large layer acts as a differential operator.

The Fourier spectrum of the n th-order derivative is given by

Input Ricker Wavelet

FT Amplitude

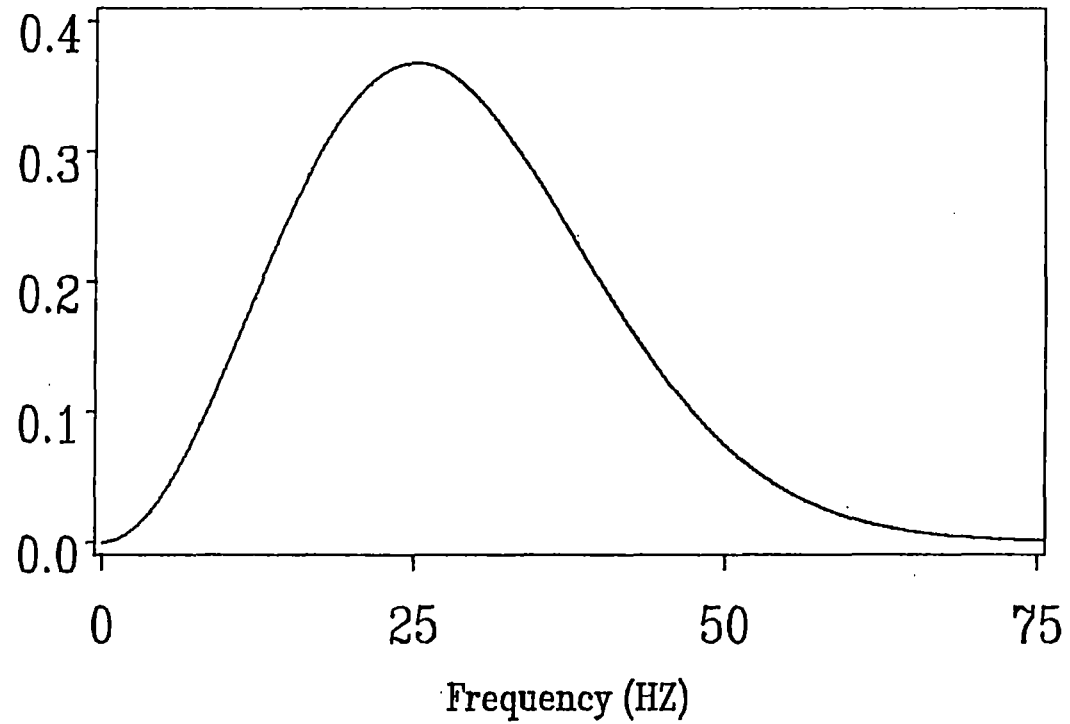


Figure 13 The input signal in the frequency domain. The signal is a 25 HZ zero-phase Ricker wavelet.

Input Ricker Wavelet

Amplitude

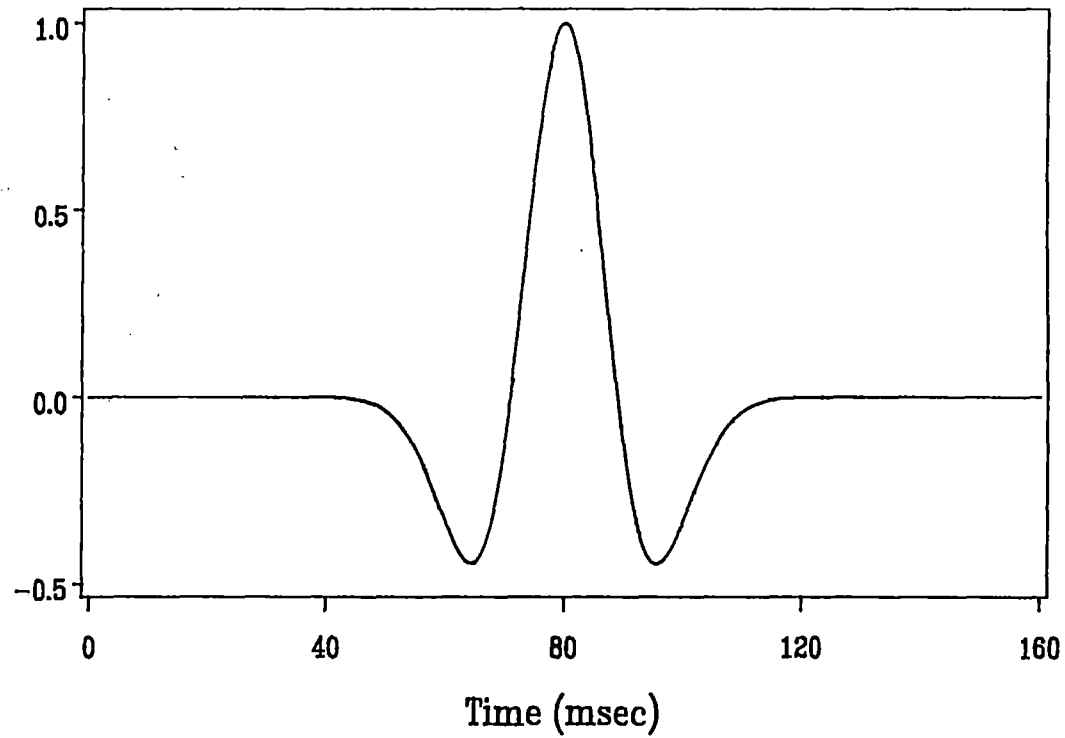


Figure 14 The input Ricker wavelet in the time domain. It has a unit amplitude at 80 msec center point.

$$F(x(t); f) = (-if)^n F(x(t)) \quad (23)$$

(Gradshteyn, and Ryzhiks, 1983)

Then the Fourier spectrum of ricker wavelet derivative, $x_d(t)$, is given by

$$\begin{aligned} X_d(f) &= (-if) X(f) \\ &= (f_0 \xi) X(\xi) e^{-i\pi/2} \end{aligned} \quad (24)$$

This is a result of the linear response of the system for thin layers. There is also a phase difference of $\pi/2$ between the Fourier spectra of Ricker wavelet and its derivative. From Equation (24) the amplitude of the spectrum of the derivative, $A_d(f)$, is given by

$$A(f) = f_0 \xi^3 e^{-\xi^2} \quad (25)$$

where its maximum is at a frequency

$$f'_0 = \sqrt{3/2} f_0 \quad (26)$$

(i.e. $f'_0 = 30.62$ H for the chosen Ricker wavelet).

So, as the wavelet changes from Ricker wavelet to the derivative form, the maximum amplitude of the Fourier spectrum experiences a significant frequency shift ($f'_0 - f_0 = f_0(\sqrt{3/2} - 1)$). The fact that the relative frequency shift ($(f'_0 - f_0)/f_0$) is more than 20%, is the motivation behind focusing on the frequency shift of the central maximum as will be discussed later.

The Fourier Transform

The Fourier transform is considered to be an extremely important mathematical tool in signal analysis. Its importance is based on the fundamental properties which relate the frequency domain representations of signals and

systems. In particular, most seismic signal processing methods (deconvolution; correlation; bandpass filtering;...) are greatly facilitated by the application of Fourier transform techniques. In this section, a brief discussion about the Fourier transform and convolution is given followed by waveform sampling and the discrete Fourier transform. Computer computations of the fast Fourier transform (FFT) and the inverse Fourier transform (IFT) are discussed in Appendix A.

The Fourier Integral

The Fourier integral is defined by the expression

$$H(f) = \int_{-\infty}^{\infty} h(t) e^{-i2\pi ft} dt \quad (27)$$

If the integral exists for every value of the parameter f then equation (27) defines $H(f)$, the Fourier transform of $h(t)$. In general the Fourier transform is a complex quantity:

$$\begin{aligned} H(f) &= R(f) + iI(f) \\ &= |H(f)| e^{i\phi(f)} \end{aligned} \quad (28)$$

where $R(f)$ is the real part of the Fourier transform,

$I(f)$ is the imaginary part of the Fourier transform,

$|H(f)|$ is the amplitude or Fourier spectrum of $h(t)$ and

is given by $R^2(f) + I^2(f)$,

$\phi(f)$ is the phase angle of the Fourier transform and

is given by $\tan^{-1}(I(f)/R(f))$.

The Inverse Fourier Transform

The inverse Fourier transform is defined as

$$h(t) = \int_{-\infty}^{\infty} H(f) e^{i2\pi ft} df \quad (29)$$

Inversion transformation allows the determination of a function of time from its Fourier transform. The two functions $h(t)$ and $H(f)$, which are related by equations (28) and (29), are termed a Fourier transform pair. The relation is indicated by the notation

$$h(t) \longleftrightarrow H(f) \quad (30)$$

A pictorial table of fourier transform pairs which are most frequently encountered is given in Appendix B. Basic properties of the Fourier transform are listed in Appendix C.

Convolution

The Convolution integral is given by

$$\begin{aligned} y(t) &= \int_{-\infty}^{\infty} x(t) h(t-\tau) dt \\ &= \int_{-\infty}^{\infty} h(t) x(t-\tau) dt \\ &= x(t) * h(t) \end{aligned} \quad (31)$$

Function $y(t)$ is said to be the convolution of the functions $x(t)$ and $h(t)$. Although it is difficult to visualize the mathematical representation of the convolution of two functions, it is a significant physical concept which is applied in many scientific fields.

A graphical meaning of convolution is illustrated in the following example. The rectangular pulse $x(t)$ is convolved with $h(t)$ which is a series of impulse functions.

The resulting convolution is a series of rectangular pulses as shown in Figure 15.

According to convolution theorem (Brigham, 1974), the Fourier transform of the convolution of two functions in the time domain is equal to the product of the Fourier transforms of the two functions in the frequency domain, i.e.

$$h(t) * x(t) \longleftrightarrow H(f) X(f). \quad (32)$$

Equivalently, applying the inverse Fourier transform to the convolution in the frequency domain leads to multiplication in the time domain, i.e.

$$h(t) x(t) \longleftrightarrow H(f) * X(f) \quad (33)$$

Waveform Sampling

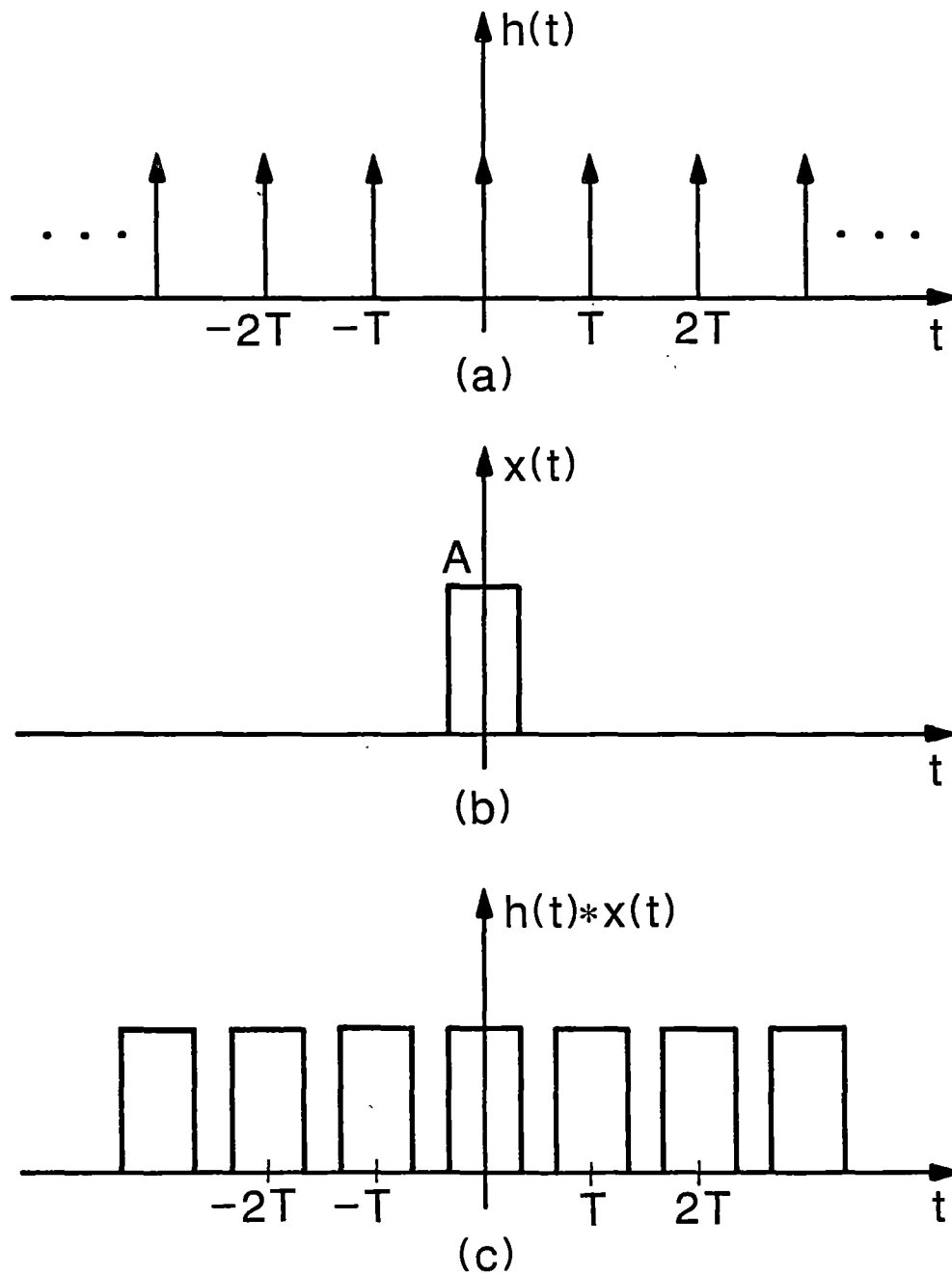
The previous section dealt with the Fourier transform representation of continuous functions of time. It can be extended to include sampled waveforms which are of particular interest in this investigation.

If the function $h(t)$ is continuous at $t=nT$, for $n=0, \pm 1, \pm 2, \dots$, then a sample of $h(t)$ at time equal to nT is expressed as

$$h(t) = \sum_{n=-\infty}^{\infty} h(nT) \delta(t-nT) \quad (34)$$

(Brigham, 1974).

Since equation (34) is the product of the continuous function $h(t)$ and the sequence of impulses, then by comparison with equation (33), the sampled waveform $h(t)$ can



Source: E. Brigham, *The Fast Fourier Transform* (New Jersey, 1974), pp. 59.

Figure 15. Impulse function convolution.

be thought as the inverse Fourier transform of the convolution of the waveform Fourier transform $H(f)$ and the frequency sampling function (the Fourier transform of the sequence of impulses).

Noting that, the Fourier transform of the sampled waveform is a periodic function where one period is equal, within a constant, to the Fourier transform of the continuous function $h(t)$. Provided that the sampling interval T is sufficiently small to avoid any aliasing which is a distortion in the time domain caused by overlapping in the frequency domain.

The Discrete Fourier Transform

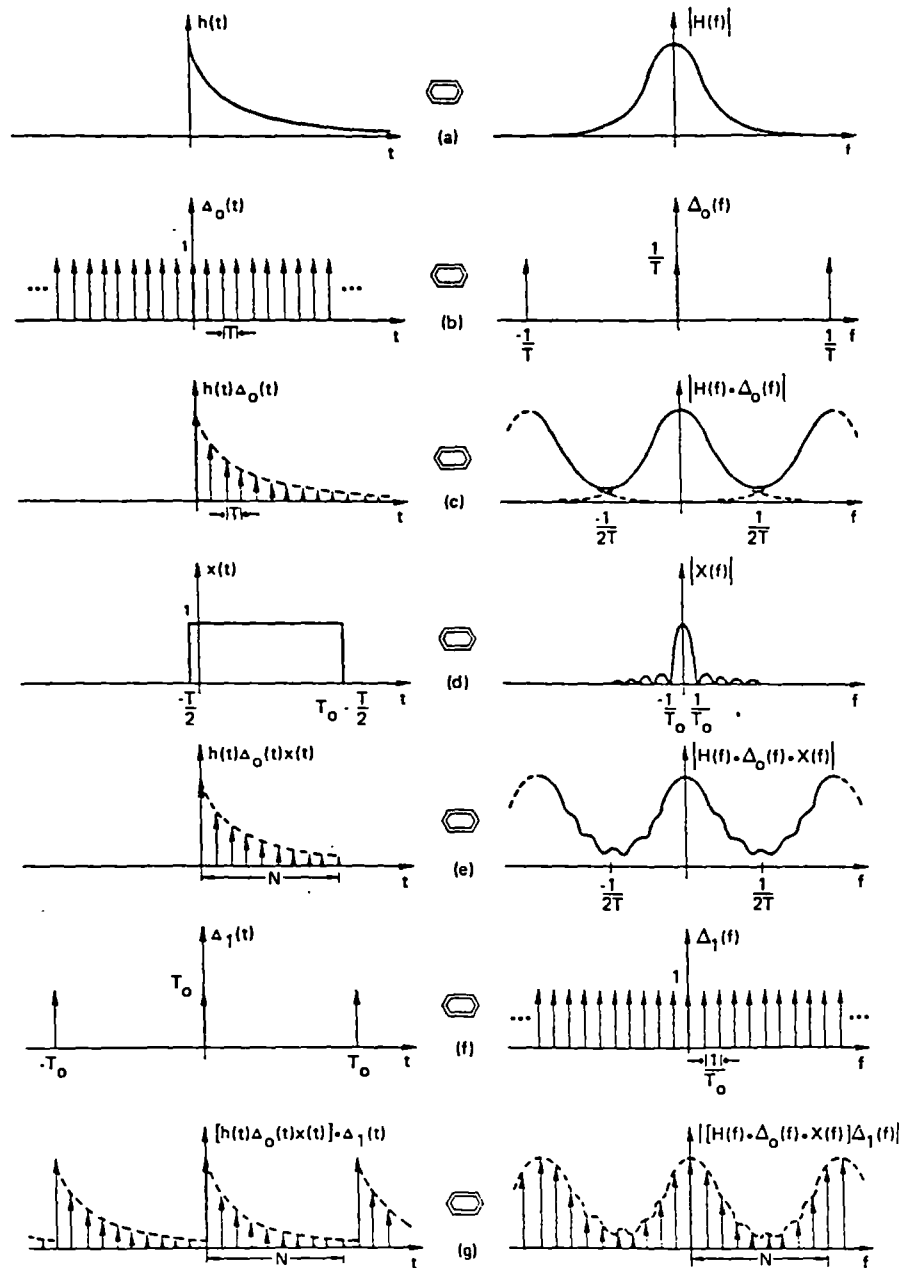
For the purpose of digital machine computation, the discrete Fourier transform has evolved as a special case of the continuous Fourier transform. Graphical evaluation of the discrete Fourier transform is illustrated in Figure (16) which includes time domain sampling, transformation, and frequency domain sampling. The discrete Fourier transform pair is given by $g(kT) \longleftrightarrow G(n/NT)$.

$$\text{where } g(kT) = (1/N) \sum_{n=0}^{N-1} G(n/NT) e^{i2\pi nk/N}$$

$$G(n/NT) = \sum_{k=0}^{N-1} g(kT) e^{-i2\pi nk/N} \quad (35)$$

and both functions are periodic with a period N .

The importance of the discrete Fourier transform has increased with the development of fast computational techniques of the Fast Fourier transform.



Source: E. Brigham, *The Fast Fourier Transform* (New Jersey, 1974), pp. 95.

Figure 16. Graphical derivation of the discrete Fourier transform pair.

CHAPTER III

NUMERICAL RESULTS AND DISCUSSION

The total reflectivity of a layer is determined using the wave sum technique outlined in the previous section and evaluated numerically for particular examples. The wave is assumed to be generated by a point source and the wave divergence $1/r$ is included in the amplitude as a function of angle in the following calculations. Numerical examples will be given for various pore fluid contents and lithologies to model the reflective behavior of a finite layer. The incident pressure waves are of particular interest in this investigation since they are the most common source used in seismic reflection investigations.

Amplitude Variation With Offset and Layer Parameters

The normal component of the net reflected p-wave amplitude is plotted as a function of angle which can be easily translated into offset when the depth of the layer is known. The numerical model consists of a layer of sandstone or limestone bounded by shale. The acoustic properties of the shale and the layer itself are varied in a way that reflects reported in situ values (see Table 2). The pore

fluid in the sandstone is changed from gas to brine to determine its effect on the reflectivity. The layer is of finite thickness which is normalized with respect to an incident p-wave wavelength. The thickness range of particular interest is less than a wavelength of the incident acoustic signal. As a particular example, consider an incident acoustic wave at a frequency of 40 Hz. The dependency of the reflectivity on the pore fluid and lithology of the layer is exhibited in Figure 17 for a layer thickness of 20 meters (65.5 feet). The effect of the pore fluid is rather dramatic near normal incidence where the reflectivity for the gas sand is considerably greater than the reflectivity of the brine sand. This large contrast in reflectivity is a source of "bright spots". It should be noted though, that large reflectivity near normal incidence of the p-wave is also observed for coal layers. If we vary the thickness to a relatively thin layer of 3 meters (10.1 feet), we notice in Figure 18 that the reflectivity for all three layer types has decreased quite considerably. For this layer thickness, the reflectivity for the gas sand would more likely be referred to as a "dull spot" rather than a "bright spot". In both figures, the reflectivity of the brine sand and limestone is calculated only to an angle which corresponds to the critical angle as discussed earlier.

For layers which exceed 30 meters (100 feet) in thickness, we notice that the reflectivity is again very low

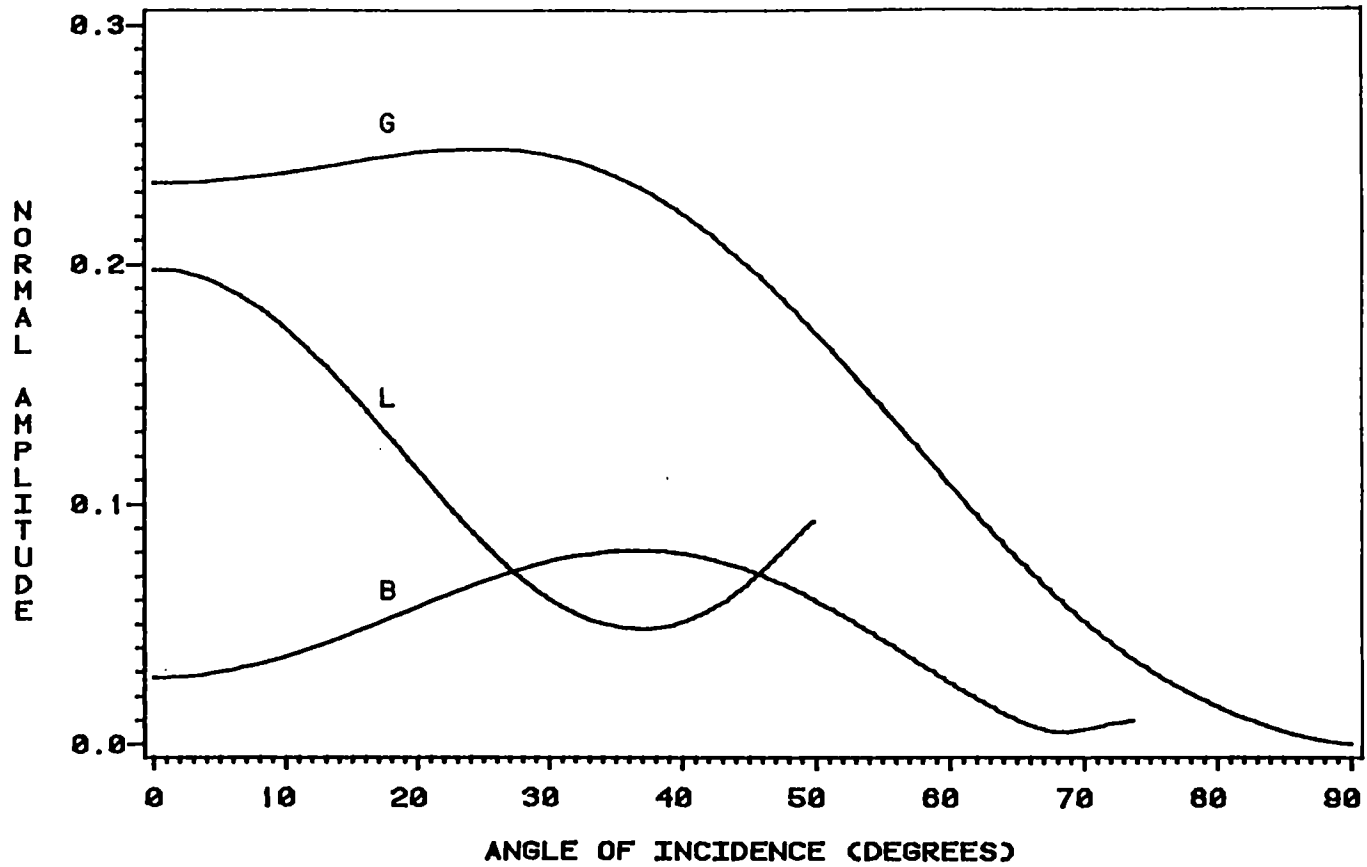


Figure 17 The normal component of the reflected amplitude of p-waves for an incident frequency of 40 Hz and thickness of 20 meters (65.5 feet). The layer consists of either a sandstone saturated with brine or gas, or a limestone layer.

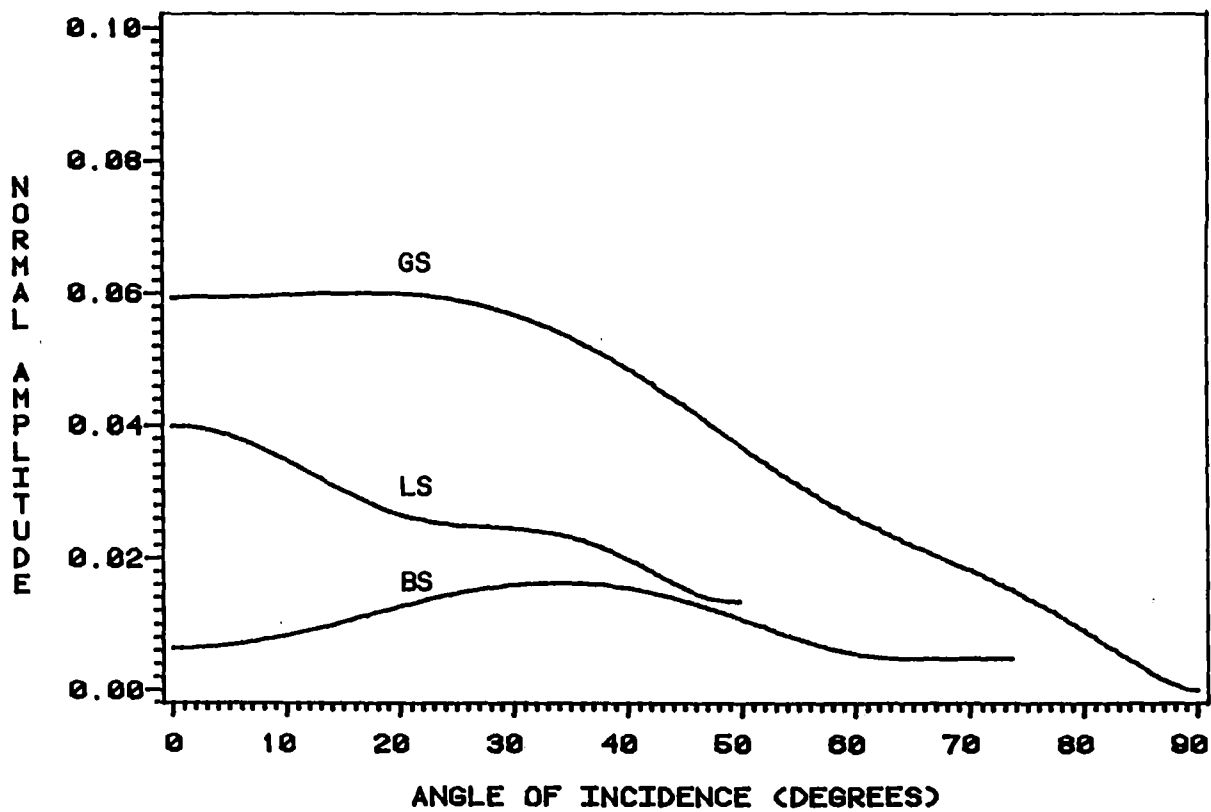


Figure 18 The normal component of the p-wave amplitude of a 40 Hz wave reflected from a 3 meter (10.1 feet) thick layer bounded by identical shale interfaces.

for all three layer types. In addition to the low reflectivity, the angular dependence is more complex than for a thin layer. The low reflectivity again, would correspond to what should be characterized as a "dull spot" in a multi-layer media. These dull spots originating from gas sands occur not only for thin layers, but also for thick layers and are dependent on the relative size of the thickness to wavelength ratio. The introduction of the second parameter, the thickness to wavelength ratio, makes it difficult to display the reflectivity in a two-dimensional diagram and is more conducive to developing amplitude surfaces which are a function of two parameters: the angle of incidence of the p-wave and the normalized thickness of the layer (with respect to the incident wavelength).

The layer reflectivity surface which varies as a function of angle as well as thickness shows a periodicity that results from the interference of the waves (Figure 19). The period is half a transmitted wavelength at normal incidence and leads to very small reflectivity particularly when the boundary layers (shale in this case) have the same properties. At both one quarter and three quarters of a transmitted wavelength, the amplitudes for the reflectivity of the gas sand are large and the typical behavior associated with "bright spots" is observed.

For a sandstone layer, the pore fluid has a large effect on its reflectivity (Domenico, 1974 and Ostrander,

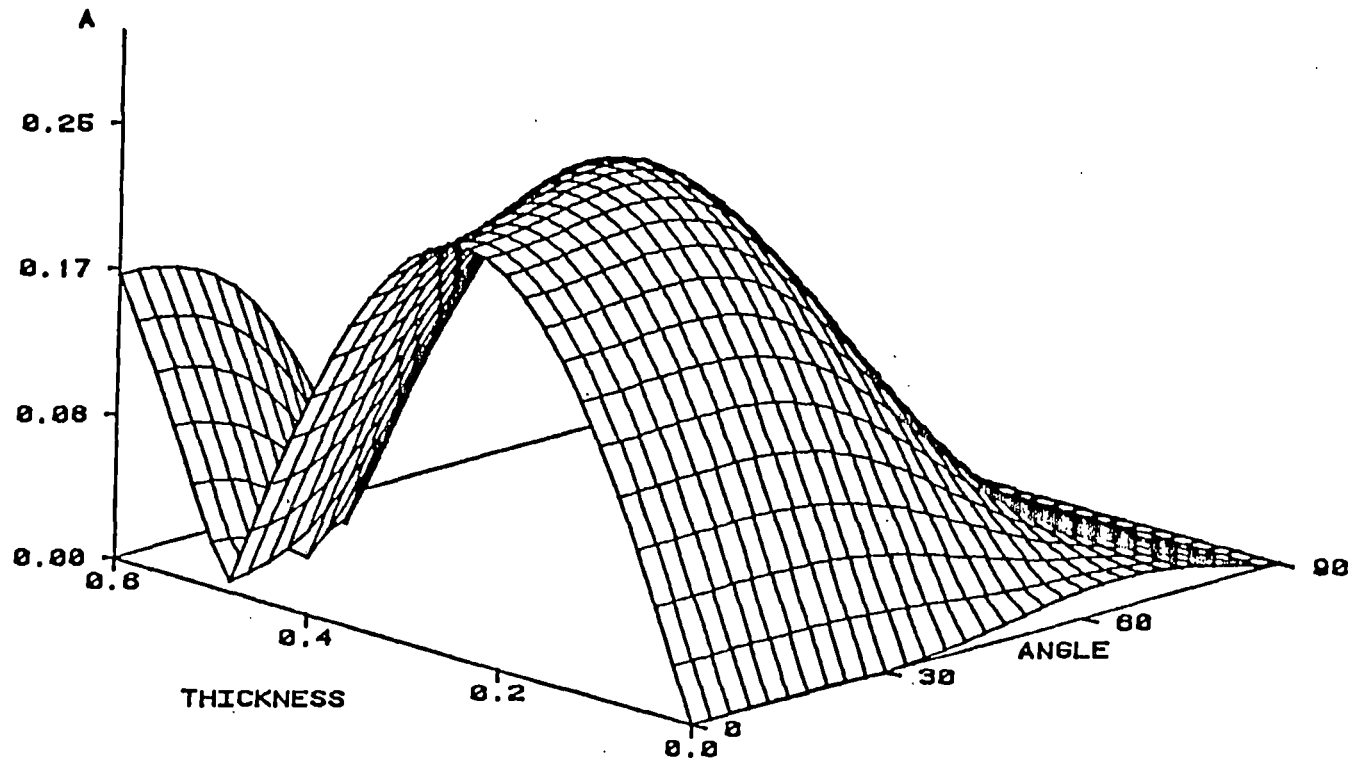


Figure 19 The net normal component of the reflected P-wave amplitude for a sandstone layer saturated with gas and bounded by shale. (S/GS/S).

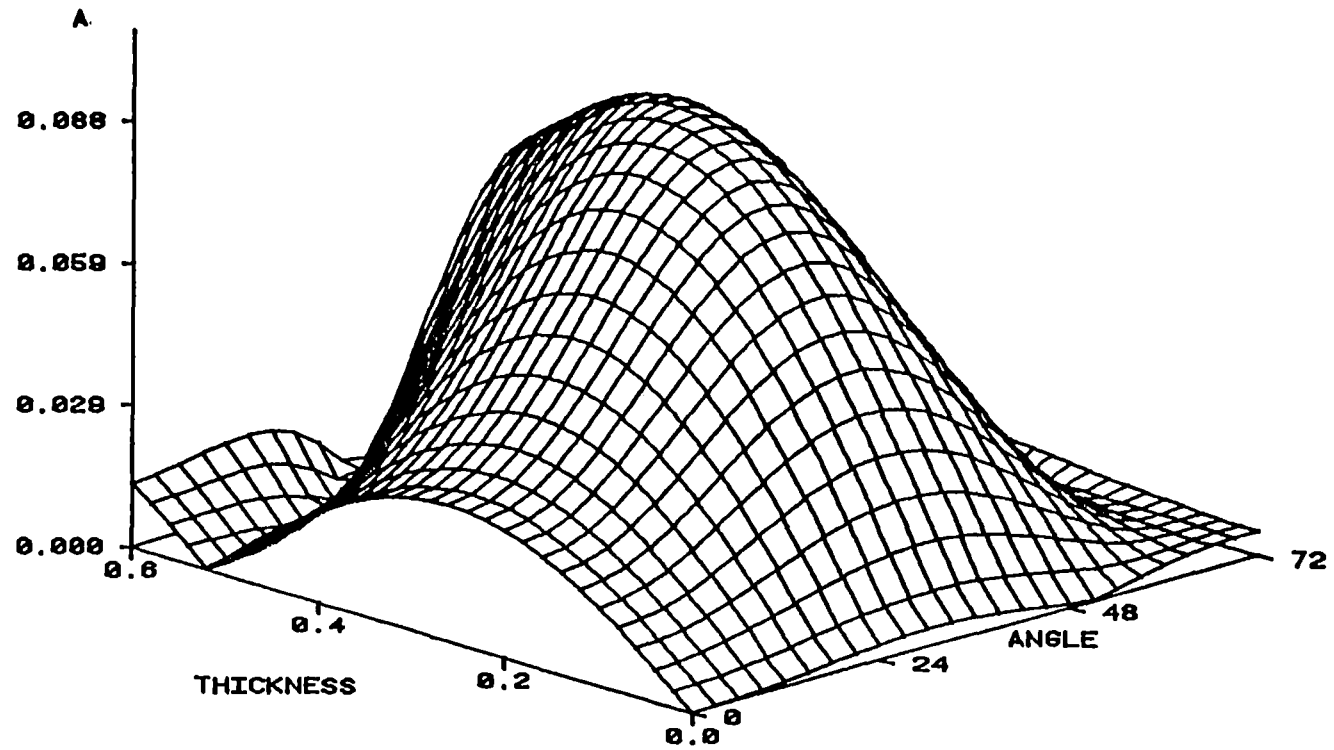


Figure 20 The net normal component of the reflected p-wave amplitude for a sandstone layer containing brine and bounded by shale (S/BS/S).

1984). As seen by comparing Figures 19 and 20, the reflectivity for a gas sand is not only larger at normal incidence than the brine sand, but persists over the whole range of angles for similar thicknesses. The bright spots in the gas sand occur in the quarter wavelength thickness range most dramatically, and are considerably larger in amplitude than those that occur for the brine sand in the same thickness range. The highest reflectivity occurs for the gas sand in this quarter wavelength range even if the layers above and below change in acoustic properties. For example, in Figure 21, the velocity of the shale has been decreased on the lower side of the layer and increased on the top side, compared to Figure 19 where the shale has the same velocity above and below. The general magnitude of the reflectivity near one quarter wavelength is still much larger than anything encountered for the brine sand but the shape of the surface for large angles has been altered. This change in lithology still provides large contrasts in reflected amplitude to distinguish between gas saturation and brine saturation, at least for some thicknesses. As noted earlier, for either thin layers, much less than a quarter of a wavelength, or thicker layers, approaching a half wavelength, the reflectivity of the gas sand is not appreciably greater than that observed for the brine sand. This clearly demonstrates that the pore fluid effect on the reflectivity is dependent on the thickness of the layer as well as the pore fluid. Therefore, the geometry of the

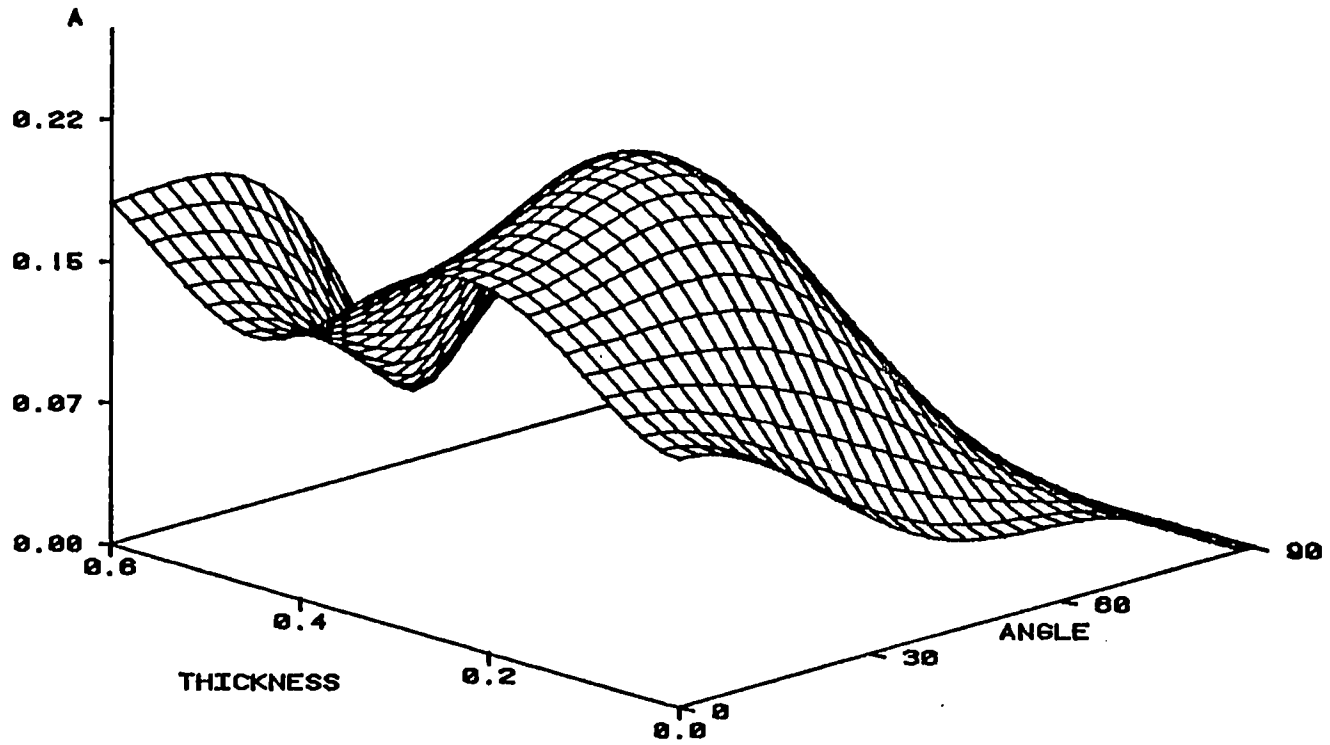


Figure 21 The normal component of the p-wave amplitude surface for a sandstone containing gas when the bounding materials are a shale of higher velocity (shale (H)) above and a lower velocity below (shale (L)) [S(H)/GS/S(L)].

layer is an important criterion in determining the overall reflectivity and gas saturated zones are not necessarily characterized by large reflectivities. In fact, the reflectivities can be of the same order of magnitude as brine saturated zones and be quite low, for some thicknesses. The "bright spot" phenomena becomes a "dull spot" for certain bed thicknesses independent of the pore fluid.

The question of uniqueness of identifying gas saturation with anomalously large reflectivity (Pan and De Bremaecker, 1970 and Sinvhal and Khattri, 1983) is raised in the next figure, (Figure 22) in which the reflectivity surface for coal is compared to the reflectivity of a gas sand. The magnitude of the reflectivity near normal incidence is large for both of these materials. Although the angular dependence is not identical for the two materials, the difference is perhaps too small to be detectable using present seismic techniques. Both have a very high reflectivity at layer thicknesses approaching a quarter of a wavelength and a much diminished reflectivity with thinner layers. The distinction between the coal layer and the gas sand would be difficult to ascertain simply on the basis of the high p-wave reflectivity of that layer resulting in bright spots.

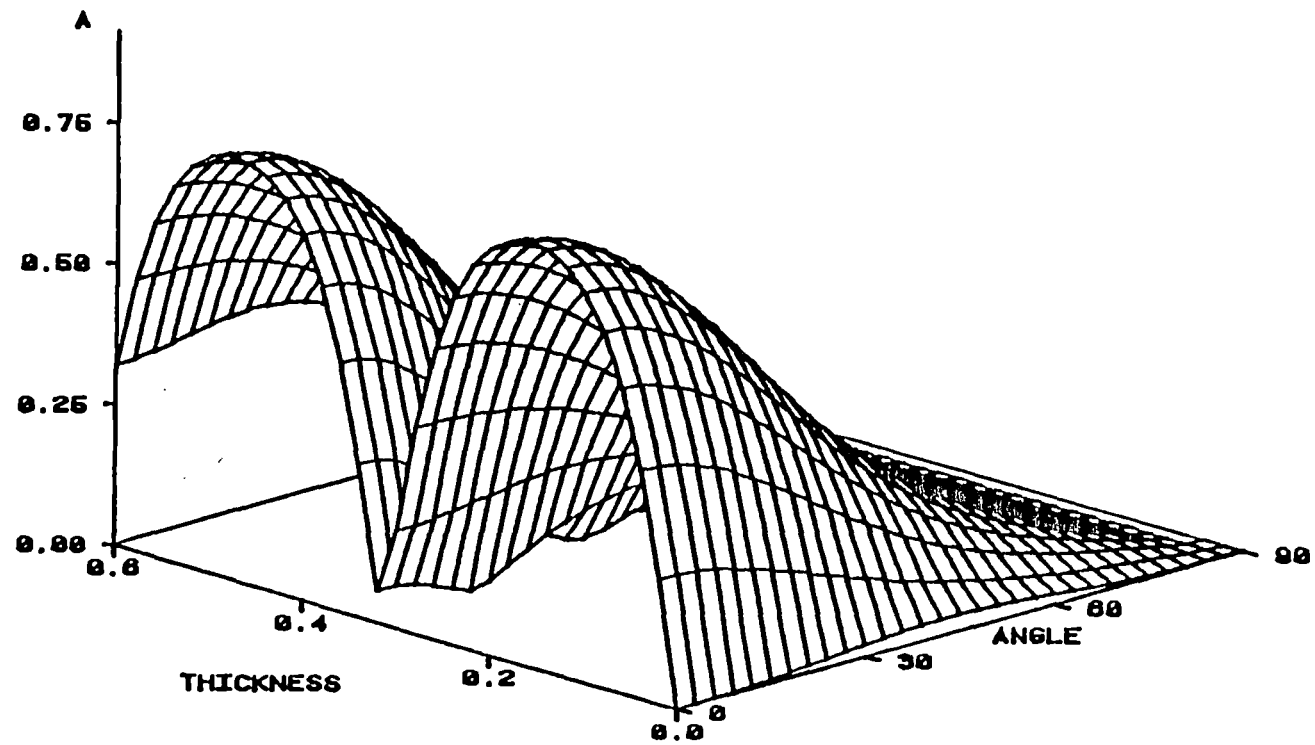


Figure 22 The normal component of the net reflected p-wave amplitude from a layer of coal encased in dissimilar shale formation [S(H)/CO/S(L)].

Mode Converted Shear Waves

In addition to the p-wave reflectivity, there is a comparable s-wave amplitude distribution which results from mode conversion. The s-waves are limited to a very narrow, angular radiation distribution which encompasses approximately 30° from the normal incidence direction. The magnitude of the amplitude of the s-wave is shown in Figure 23 for a coal layer encased in shale and in Figure 24 for a gas sand layer. There is an obvious difference in the amplitude distribution in the region 10 to 15 degrees from normal incidence. The coal exhibits relatively large amplitude shear waves while in the gas sand they are quite small in the same region. In comparable thickness ranges for which the p-wave amplitude for both the coal and gas sand is particularly large, the shear wave amplitude can be quite different for the two layer materials. At approximately a thickness to wavelength ratio of one quarter, the coal mode converted shear waves exhibit a large maximum in an angular range of 10 to 25 degrees, while the amplitude of the gas sand layer mode converted waves is smaller and forms two lobes. Therefore, it is possible to distinguish between reflectivity from gas sand and coal layers by determining the amplitude distribution of the mode converted shear waves as a function of the radiation angle. The amplitude of the mode converted waves for the gas sand can be considerably less than those for the coal in a narrow angular range near normal incidence.

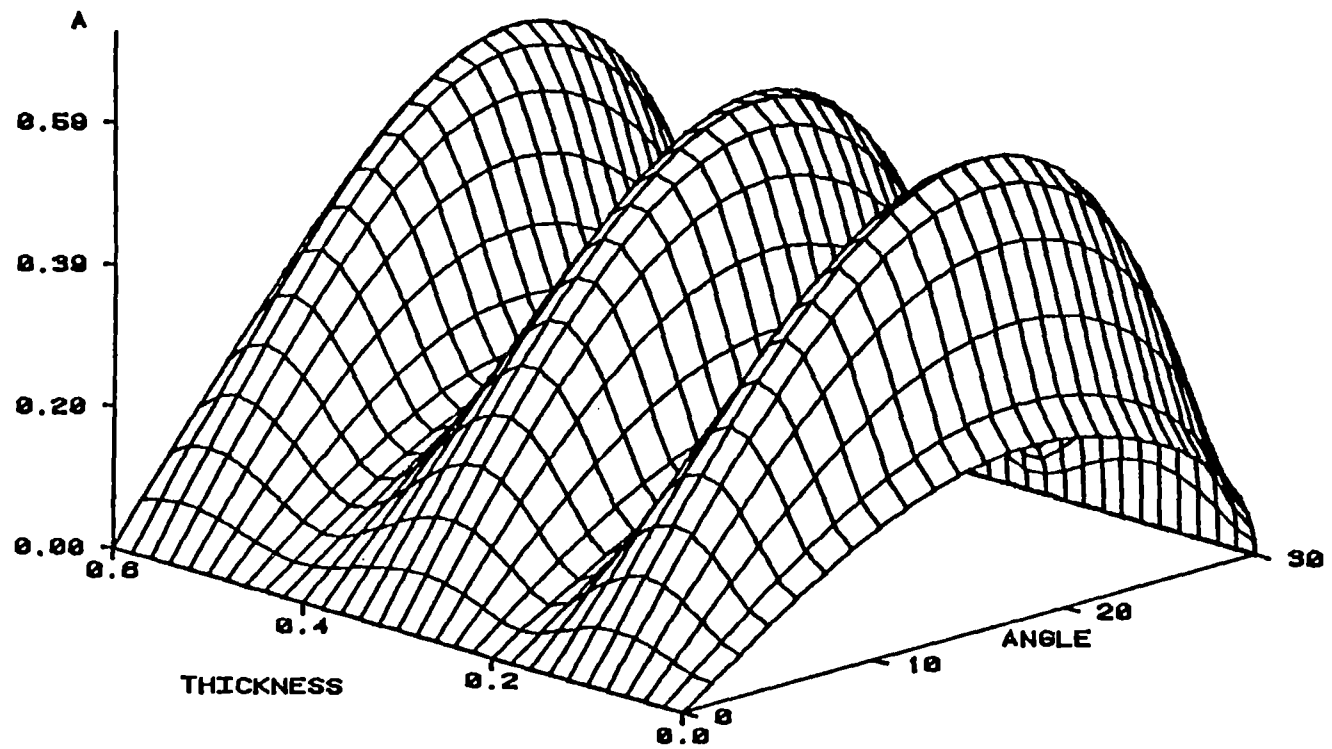


Figure 23 The mode converted s-wave amplitude which results from reflection of a p-wave from a coal layer surrounded by shale [S(H)/CO/S(L)].

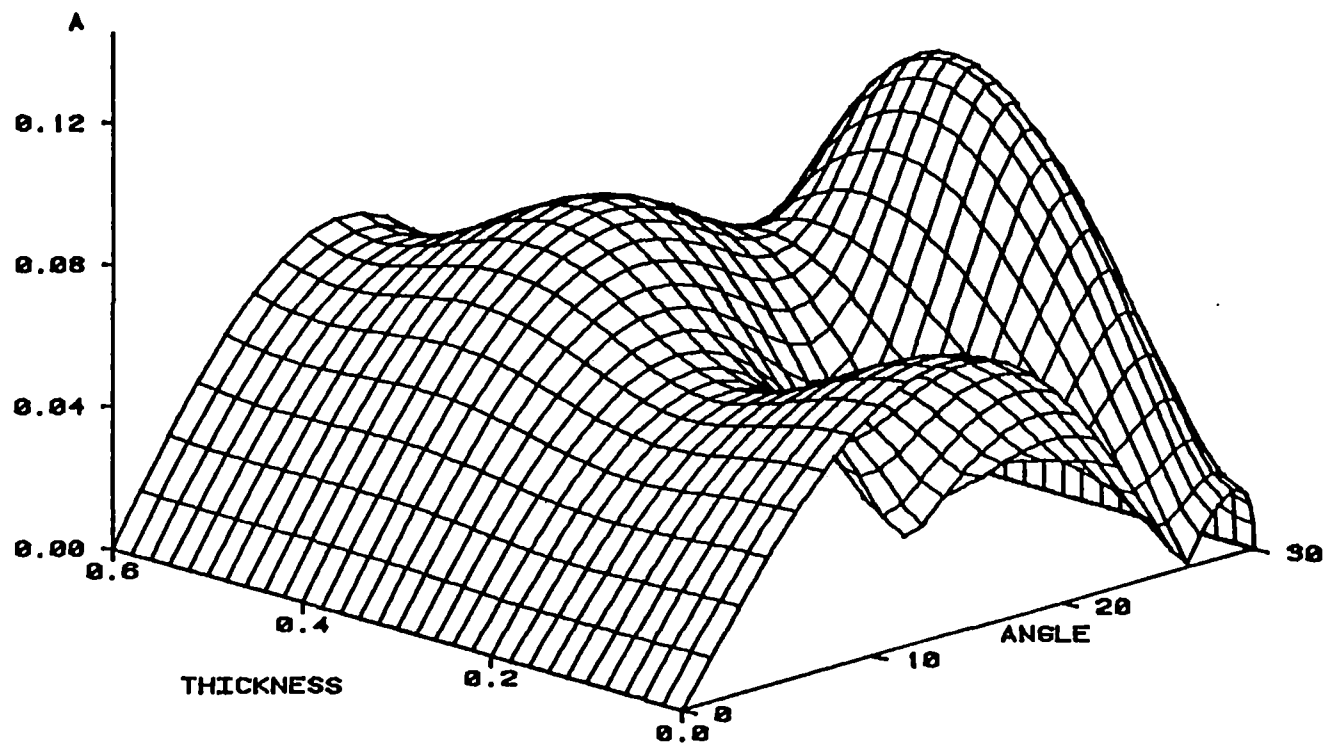


Figure 24 Mode converted s-wave amplitudes for a gas saturated sandstone layer surrounded by shale [S/GS/S].

Phase Shift Variation With Offset and Layer Parameters

An additional feature which can be used to differentiate between layer characteristics is the phase of the reflected p-wave. The wave phase is determined from the wave sum [Eq (18)] by calculating the position of extrema in the net reflected signal as the thickness and incident angle are varied. Examples of a wave phase surface for a limestone layer and gas sand layer are shown in Fig (25) and Fig. (26). There is an average phase difference of approximately 180° between surfaces indicating the return signal is of opposite phase for the two layers at normal incidence. The precise phase difference between the two net reflected waves varies somewhat above and below 180° over the range of parameters of the surface. This variation would be seen as a deviation of the travel time from strictly parabolic behavior. The relative wave phase shift as a function of angle is an important parameter which can be used to distinguish between layers of differing characteristics. The angular dependence of the wave phase for various layers is shown in Figure (27). The layer thickness is chosen to yield the maximum layer reflectivity. Both the angular dependence of the wave phase and the magnitude distinguish the fluid saturated sandstone from the limestone layer. The rapid change in phase for the brine sand is an indication of a critical angle for this

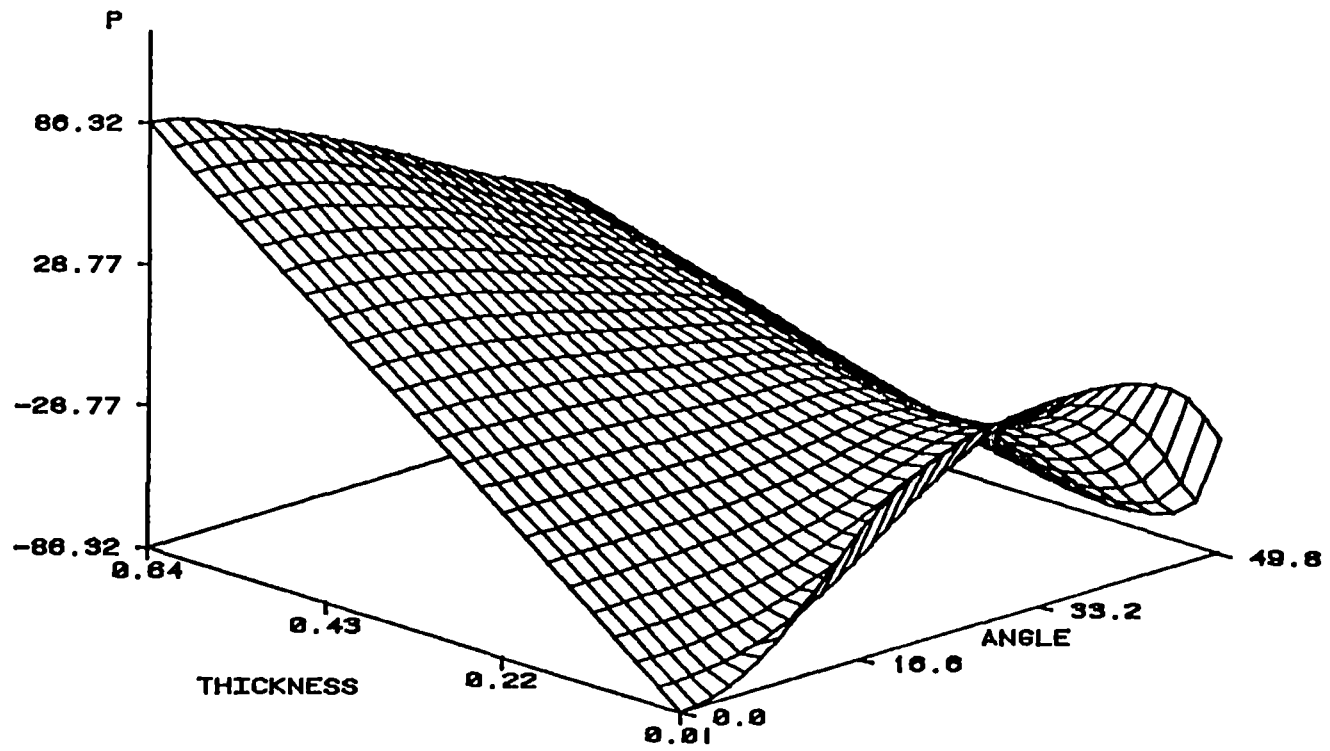


Figure 25 The phase of net p-wave reflected from a limestone layer surrounded by identical shale boundary material (S/LS/S).

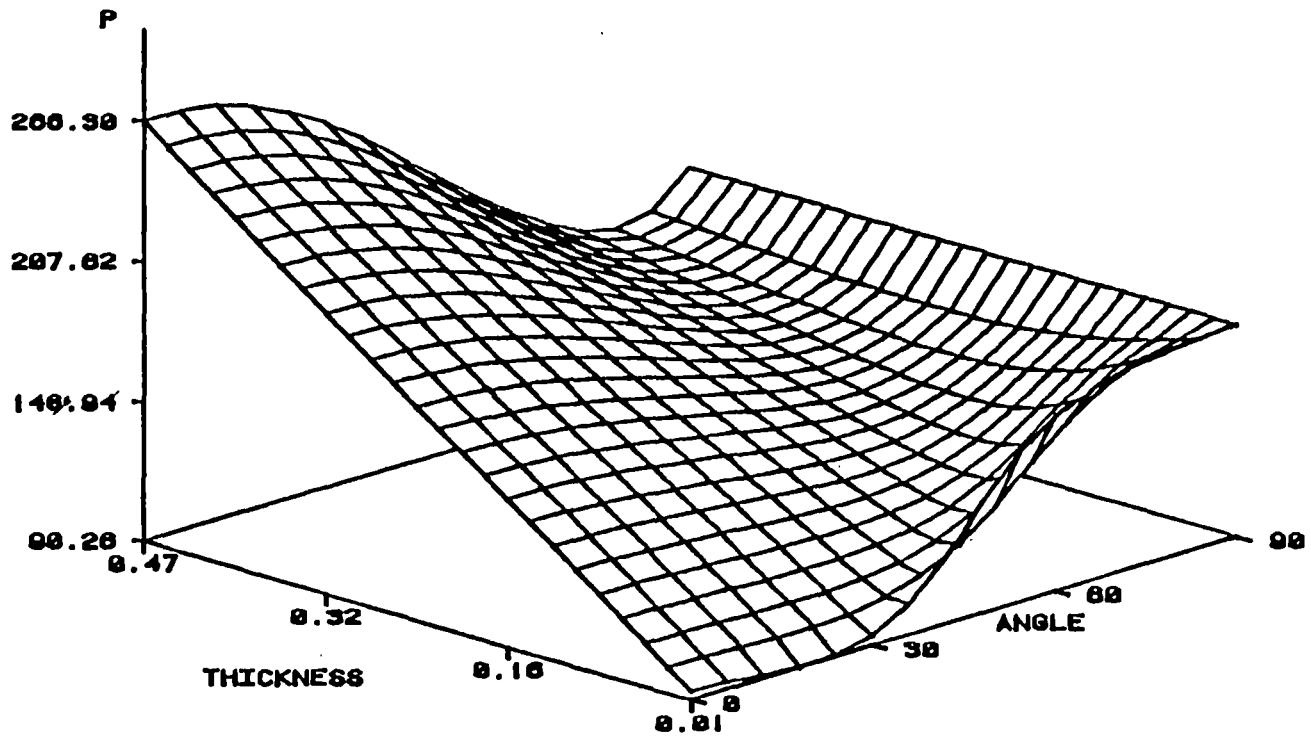


Figure 26 The phase of the net p-wave reflected from a gas-saturated layer encased in shale formation (S/GS/S).

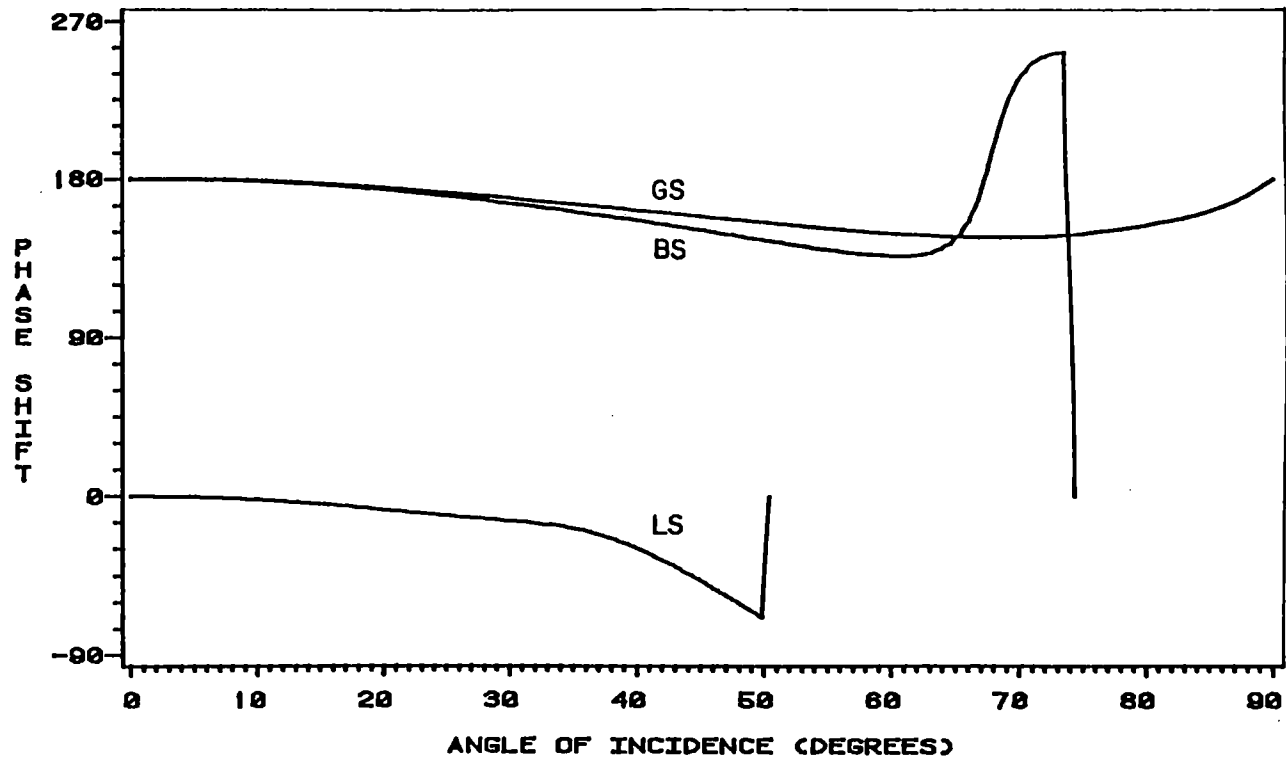


Figure 27 The wave phase for one quarter wavelength thick layer. The layer material consists of either a sandstone saturated with gas or brine, or a limestone layer. The layer is bounded by shale.

particular lithology of the bounding materials. The angular variation in the wave phase is sensitive to both the pore fluid and the surrounding lithology similar to the behavior of the net amplitude.

In our previous discussion, shale, a relatively low velocity structure, had surrounded the layer of interest. The determination of the pore fluid in the layer is now considered with limestone as the upper component surrounding the porous layer which is saturated with gas (Figure 28). Structure as a function of layer thickness that was seen with the shale surfaces is also exhibited when there is no critical angle. The amplitude of the p-wave for the gas saturated sandstone is approximately twice as large as that for the brine saturated sandstone (Figure 20). The $1/r$ dependence for the point source is included and is obvious as one approaches 90° . The normal component of the p-wave is plotted on these surfaces as has been done previously. The larger amplitude of the p-wave reflected from the gas saturated sand also occurs for other lithologies, as for example, if the brine saturated sandstone or shale is encased in two different limestone boundaries. The p-wave amplitude for the gas sand is typically two times larger than that of the brine sand reflections. This is the major distinguishing feature between the two pore fluid types. The mode converted s-wave for this layer boundary arrangement yields similar amplitude mode converted waves which do not offer any distinguishing features.

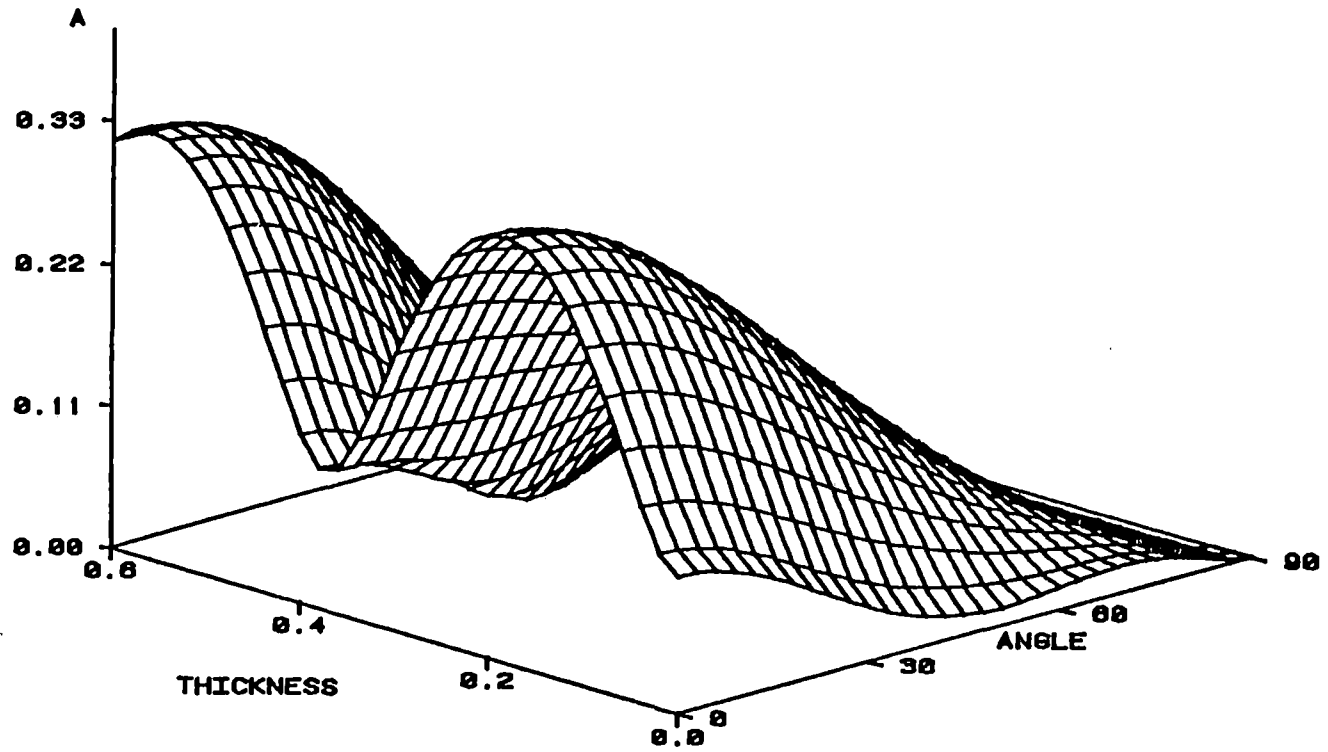


Figure 28 The normal component of the net p-wave amplitude reflected from a gas saturated sandstone bounded above by limestone and below by shale (LS/GS/S).

The sensitivity of the net reflectivity to the lithology and pore fluid of both the layer and its surroundings leads to a diversity of responses to various combinations of materials listed in Table 2.

The reflectivity for both the p-wave and the mode converted s-wave depends critically on the lithology of the surrounding media. To apply amplitude analysis to a range of reflectivities which do not constitute "bright spots" requires additional information concerning the acoustic properties of the surrounding media. Observation of critical angles for both the p-wave and mode converted s-wave can provide this information. The critical angle for the p-wave is related to the ratio of the p-wave velocity of the reflection zone to that of the layer material. The critical angle for the s-wave is related to the s-wave velocity in the reflection zone to the s-wave velocity of the layer. The critical angle for the s-wave is determined from the rather large peak in amplitude which occurs at the critical angle. An example of the mode converted s-wave surface is shown in Fig (29). The surface is continued beyond the critical angle (22.6°) by approximately the net mode converted signal by the top surface and transmitted mode converted wave. The largest amplitude occurs just prior to the critical angle. The angular range of interest is less than 30° from the normal and would be within the coverages of most seismic lines.

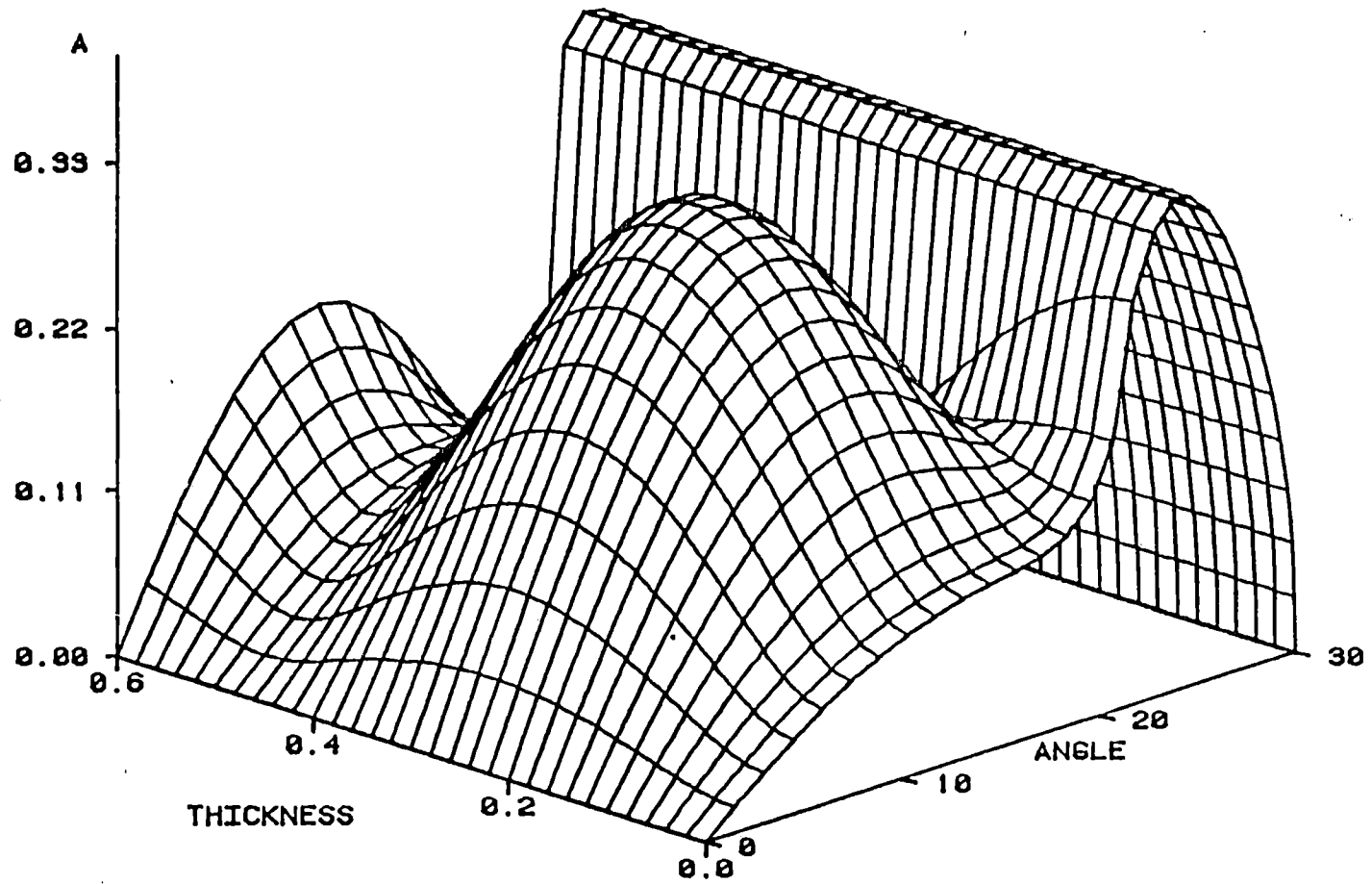


Figure 29 The amplitude of the mode converted shear waves extended beyond the critical angle (50°). The limestone layer is bounded by a low velocity shale [S/LS/S(L)].

The critical angle associated with the p-wave velocities occurs typically at much larger angles for the materials considered in this study. The maximum in the normal component of the net reflected p-wave occurs at the critical angle (50.3°) as seen in Fig (30). The continuation of the amplitude surface beyond the critical angle is approximated by the amplitude of the top surface (PP) reflection. Each of the critical angle reflections is the largest amplitude feature on both the p-wave and mode converted s-wave surfaces and should be observable compared to other amplitude features. Information concerning the acoustic velocity ratio of the upper material and layer can provide a basis for characterizing the properties of the reflection zone and to a lesser extent, the layer itself (Tatham and Stoffa, 1976 and McCormack et, al, 1984). The absence of the critical angle also provides a limited amount of information concerning the reflection zone and layer. The velocity ratios obtained from the critical angles are important quantitative features which may be used to predict which rock types comprise the upper boundary. This would provide important information for developing a model when "bright spots" are not observed, but a producing formation is suspected.

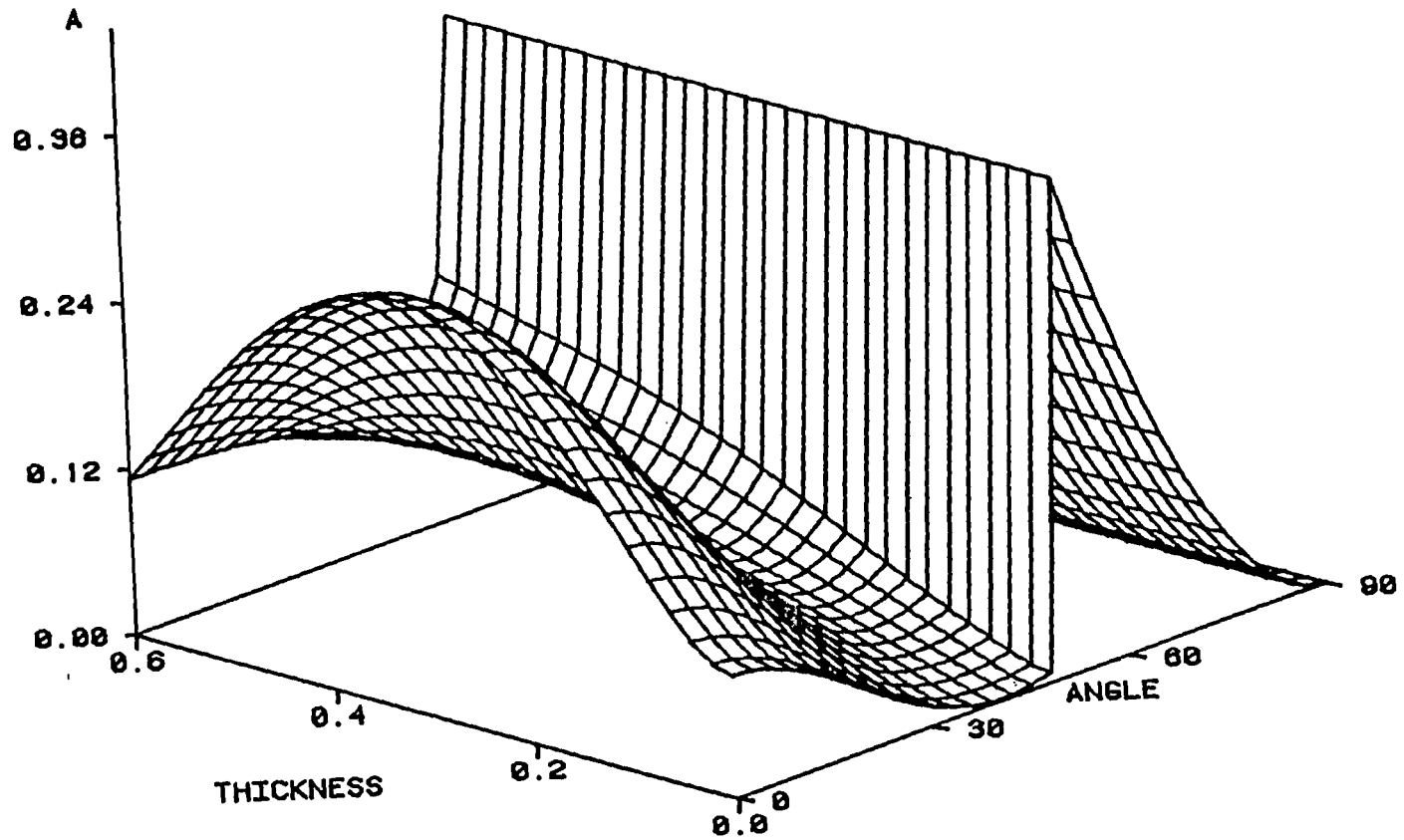


Figure 30 The normal component of the net reflected p-wave extended beyond the critical angle. A maximum in amplitude occurs at the critical angle. The limestone layer is bounded by shale [S/LS/S(L)].

Numerical Evaluation of Thin Layer Response

Layer Thickness

The thickness of the layer plays an important role in the interference of multiples within the layer with the primary reflection, and hence affects the amplitude and shape of the final reflected wavelet. The effect of thickness on the time domain seismic trace is shown in Figure 31 for a 25 Hz zero phase Ricker wavelet reflected from a gas saturated sand layer encased in an identical shale formation. The surface normal component of the p-wave displacement is computed and includes the effect of geometric divergence from a point source. There are two distinct regions in the figure. In the first it is difficult to resolve the shape of the reflected wavelet which is similar to the shape of the derivative of the Ricker wavelet. This is considered the thin response region. The amplitude in this region exhibits a tuning effect due to constructive interference of the multiply reflected signal within the layer and a maximum amplitude is observed. This result is in agreement with those obtained by other investigators (Meckel and Nath, 1977). For layer thicknesses smaller than the tuning thickness the amplitude increases with thickness (Wide, 1973; Koefoed 1980). The second region is the thick layer region, where the first multiple wavelet coming from the bottom interface is resolved from the top reflection wavelet. The amplitude in

SHALE / GAS SAND / SHALE

NORMAL INCIDENCE

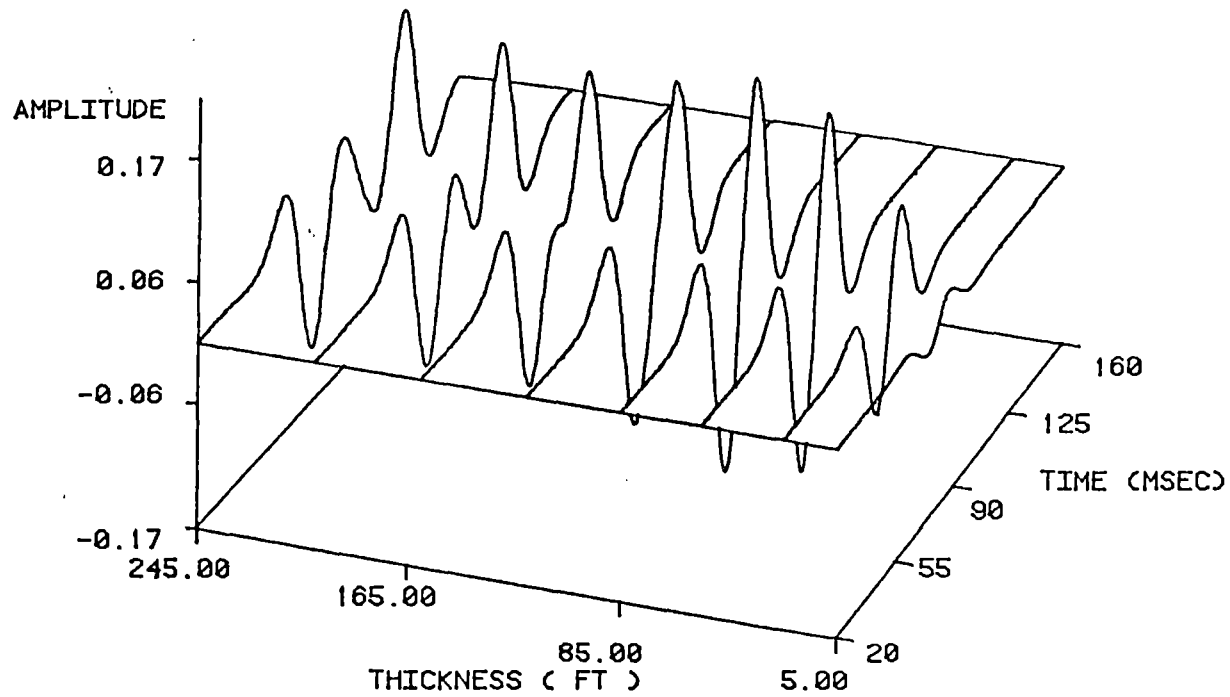


Figure 31 Seismic traces of reflected P-wave for a wide range of thickness, including thin layer region.

this region is invariant with thickness variation and only a function of the relative impedance of the target layer with respect to the surrounding materials. This study is limited to the thin layer region where the thickness is less than fifty feet.

Layer Lithology and Pore Fluids

Recently, there has been a growing interest in the use of reflection amplitude anomalies (bright spots) as a direct hydrocarbon indicator. However, the fact that there have been erroneous interpretations of bright spots indicated more careful analysis of the reflected wavelet character is necessary. The amplitude offset dependence of various configurations which can lead to bright spots, including coal and limestone layers, is discussed below. For the sake of comparison between different layer responses, the surrounding materials are chosen to be identical shales and the thickness of the layer is kept at 25 feet. The amplitudes of the reflected p-wave decreases with offset for gas sand and coal as shown in Figure 32, and Figure 33 respectively. The geophone positions are at equal intervals with the maximum offset at 50° . The amplitudes of coal layer reflections decrease more rapidly than those of the gas sand. The p-wave amplitude for limestone also decreases with offset, then increases sharply near the critical angle as shown in Figure 34. The reflected wavelet character for the limestone varies from a derivative form near normal

SHALE / GAS SAND / SHALE

NORMAL INCIDENCE

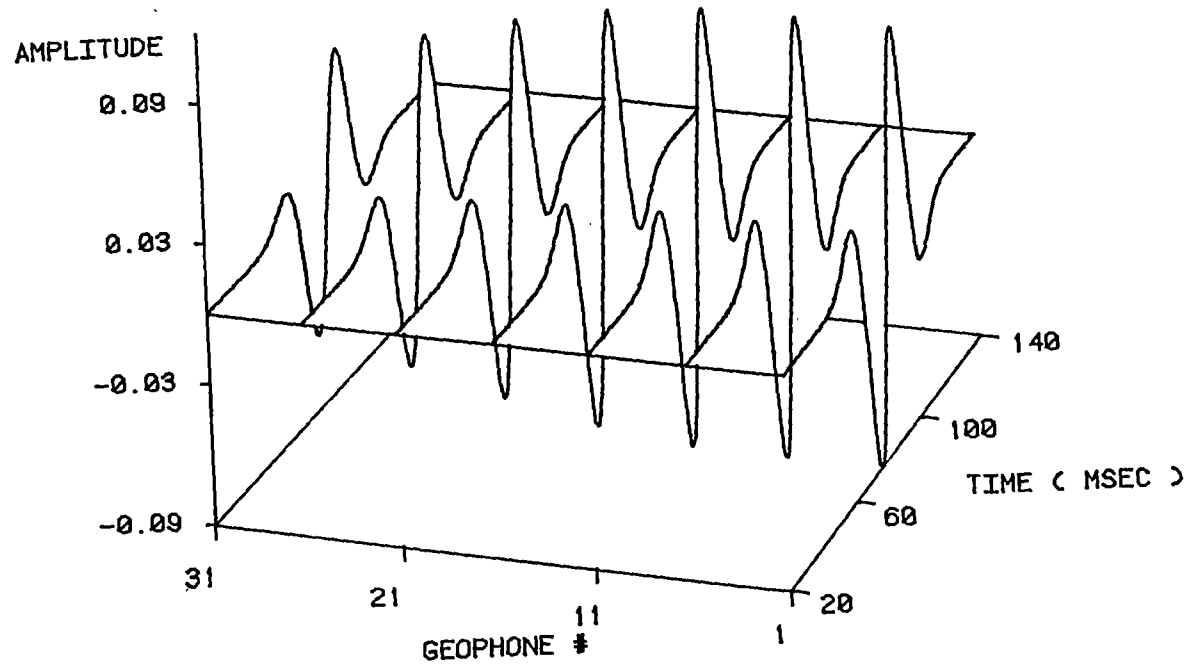


Figure 32 Amplitude offset dependence of reflected P-waves from gas saturated sands, the maximum offset shown refers to 50° angle of incidence.

SHALE / COAL / SHALE

THICKNESS=25 FEET

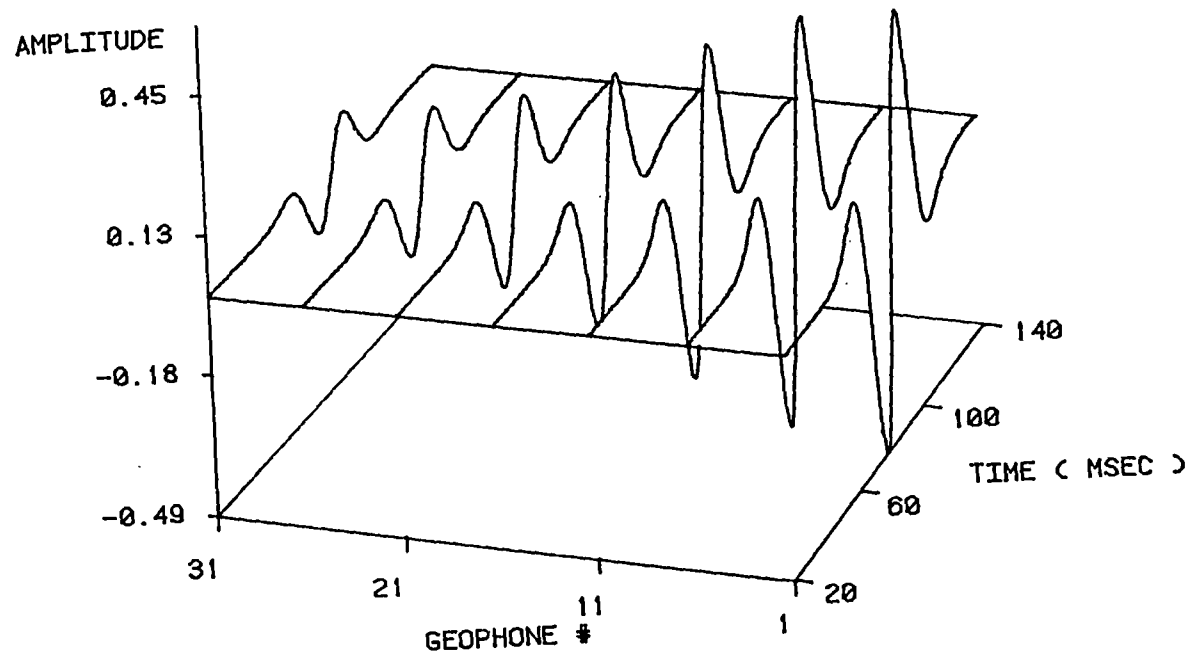


Figure 33 Amplitude offset dependence of reflected P-waves from a coal layer.

SHALE / LIMESTONE / SHALE

THICKNESS=25 FEET

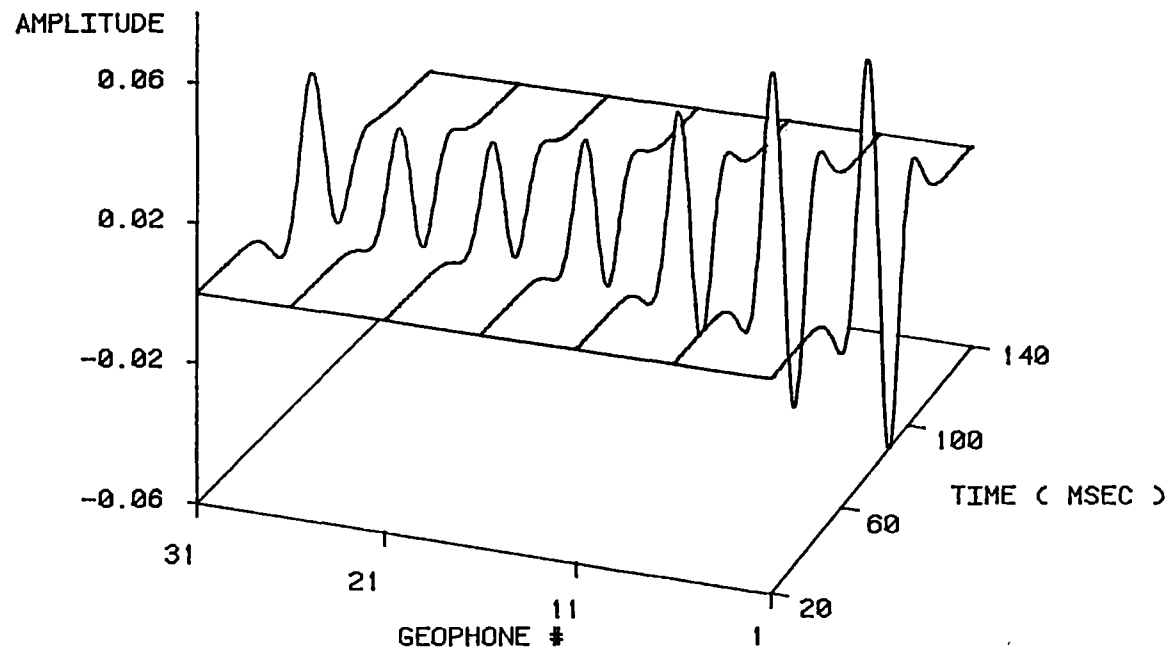


Figure 34 Amplitude offset dependence of reflected P-waves from a limestone layer.

incidence, to the shape of the Ricker wavelet near the critical angle. The polarity of the derivative reflected from a limestone layer is opposite to that from gas sand or coal layers.

Changing the pore-fluid in the sandstone layer from gas to water alters the sandstone seismic velocity and bulk density (Domenico, 1974). This leads to a significant change in the reflection amplitude function. The amplitude of the reflected p-wave Ricker wavelet for brine saturated sand is found to initially increase with offset to some maximum and the wavelet is of a derivative form for the range of offset shown (Figure 35).

The wavelet characteristics in the time domain don't uniquely define the lithology and pore fluid of the target layer. The reflected wavelet characteristics are not only dependent on the layer's pore fluid and lithology but also on its thickness and on the physical properties of the adjacent boundary layers.

Boundary Material

For thin layers, the reflected wavelet is the result of waves reflected from the upper and lower boundaries of the layer as well as multiple waves within the layer. The reflection coefficients at the boundary of the layer are related to the relative density and seismic velocities of the layer to the surrounding media. The model calculations include all possible boundaries combinations listed in Table

SHALE / BRINE SAND / SHALE

THICKNESS=25 FEET

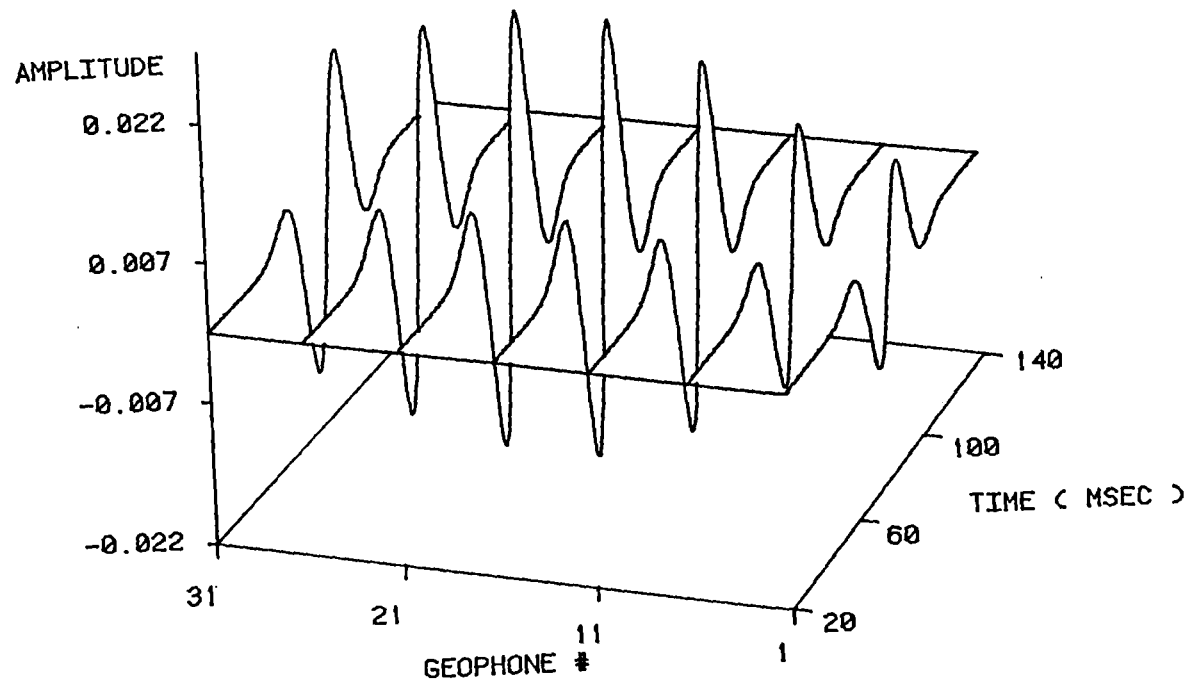


Figure 35 Amplitude offset dependence of reflected P-waves from brine saturated sands.

I- Shale / Gas sand / Shale(H)
 II- Shale(H) / Gas sand / Shale
 III- Shale / Gas sand / Shale

Amplitude

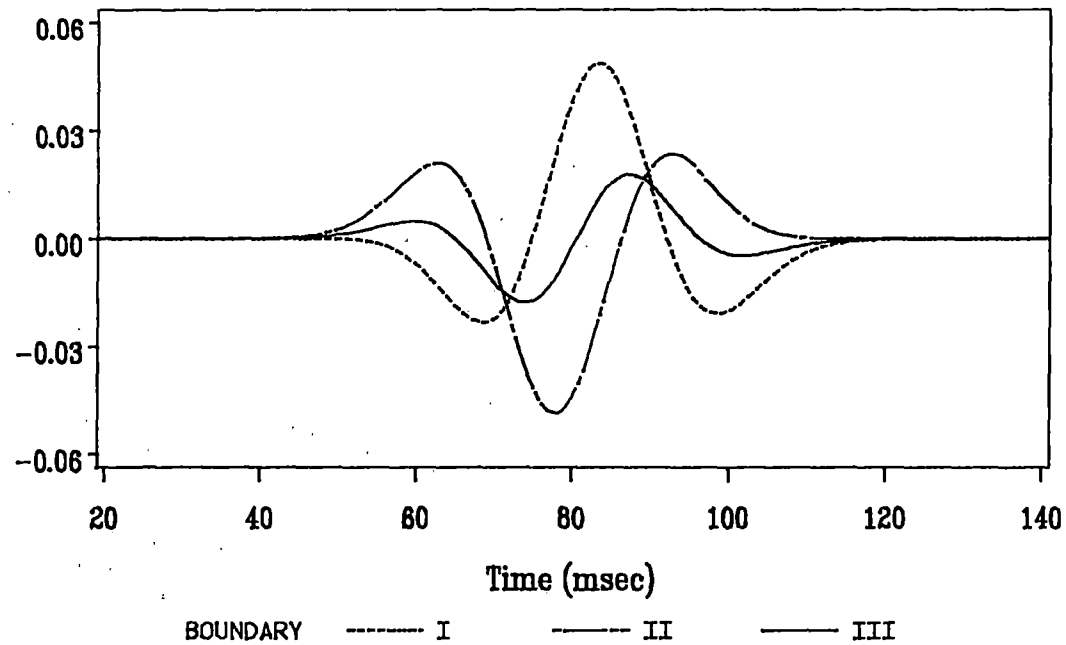


Figure 36 Sensitivity of wavelet polarity to the bounding materials.

TABLE IV

THE LABELING USED TO DESIGNATE THE NEIGHBORING LITHOLOGIES FOR THE SPECIFIED LAYER. FOR EXAMPLE GAS III IMPLIES A SHALE LAYER ABOVE (REFLECTION ZONE), A GAS SATURATED LAYER, WHICH IS BOUNDED BELOW (TRANSMISSION ZONE) BY A HIGH VELOCITY SHALE.

<u>Upper Lithology</u>	<u>Lower Lithology</u>	<u>Boundary Designation</u>
Shale	Shale	I
Shale (H)	Shale (H)	II
Shale	Shale (H)	III
Shale (H)	Shale	IV
Limestone	Shale	V
Limestone	Shale (H)	VI

4 for the four types of layers in question. A representative summary of the boundary effects is given in the following:

The sensitivity of the reflected wavelet at normal incidence to the variation of neighboring lithology is illustrated in Figure 36 for a 10 ft gas sand. As the boundary materials are changed from dissimilar shale (III) to identical shale (I), the reflected signal changes from the Ricker wavelet form to the derivative form. Now, if the boundary shale sequence is reversed (III to IV) the polarity of the reflected wavelet will be reversed. Thus, polarity is dependent on the boundary materials and is not sufficient by itself to identify the characteristics of the target layer.

Mode-Converted Waves

In addition to the reflected p-waves, there are mode converted shear waves whose arrival at the geophones is distinguished by their separation in time. The amplitudes of these shear waves are much smaller than those of the p-wave (Almoghrabi and Lange, 1986). The time domain response of the mode converted shear waves as a function of offset is illustrated in Figures 37 and 38 for both a gas sand and a coal layer with thickness of 25 feet and bounded by two different shales. The polarity as well as the amplitude variation within offset are different for both layer types. These wavelet characters are again affected by the layer

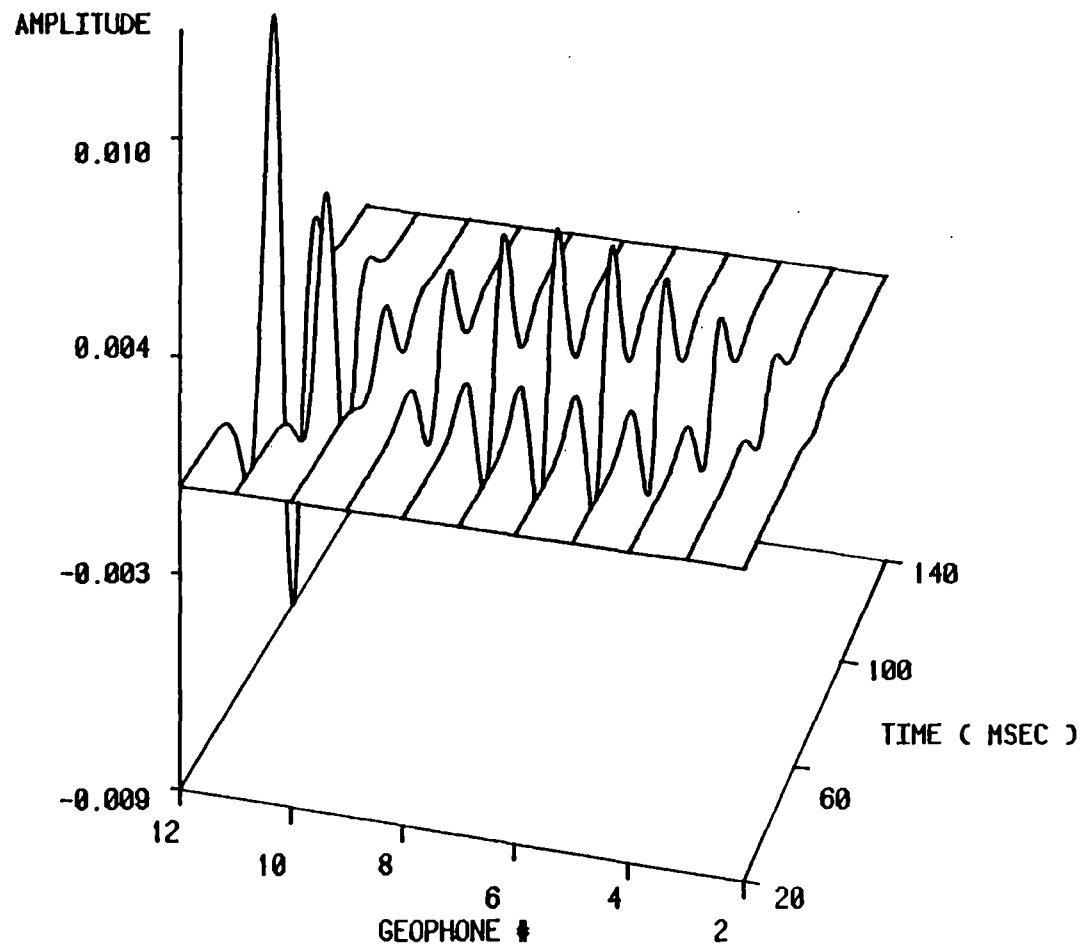


Figure 37 Mode-converted S-waves for a gas sand layer as a function of offset.

SHALE / COAL / SHALE (H)

THICKNESS=25 FEET

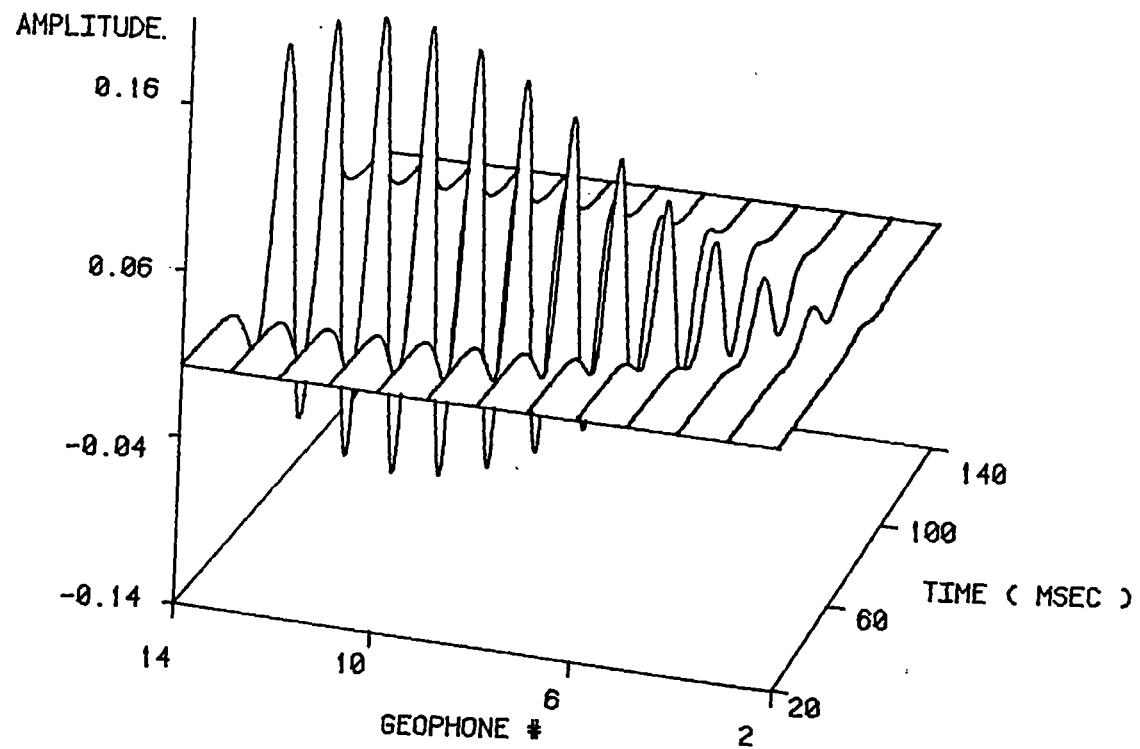


Figure 38 Mode-converted S-waves for a coal layer as a function of offset.

thickness and the physical parameters of the bounding materials. The dependence of the signal shapes in the time domain on a number of parameters in addition to pore fluid prevents their use in uniquely identifying the pore fluid.

Time domain information is limited to the amplitude and polarity but does not readily yield details of the signal shapes. To obtain a more detailed analysis of the reflected impulse, the frequency domain response is analyzed using Fourier transform techniques.

Spectral Characters of Reflected Wavelets

The change in frequency spectrum of the reflected impulse relative to the incident spectrum reveals the filtering behavior of the target layer. The frequency response of the reflected Ricker wavelet is shown in Figure 39 for a gas sand layer 5 feet thick. The Fourier transforms of the time domain signals are obtained as a function of offset. The amplitude of the Fourier spectrum is seen to decrease with increasing offset in a manner which depends on both the layer reflectivity and the specific impulse waveform. The position of the maximum of the Fourier spectrum varies with offset by shifting from 30 Hz at normal incidence to 25 Hz (the center frequency of the incident wavelet) as the offset approaches grazing. The spectrum varies with both layer parameters and the physical properties of the bounding material. This is illustrated by the offset variation of the maximum amplitude of the Fourier

Variation of Central Frequency with Offset
Shale / Gas sand / Shale

FT Amplitude

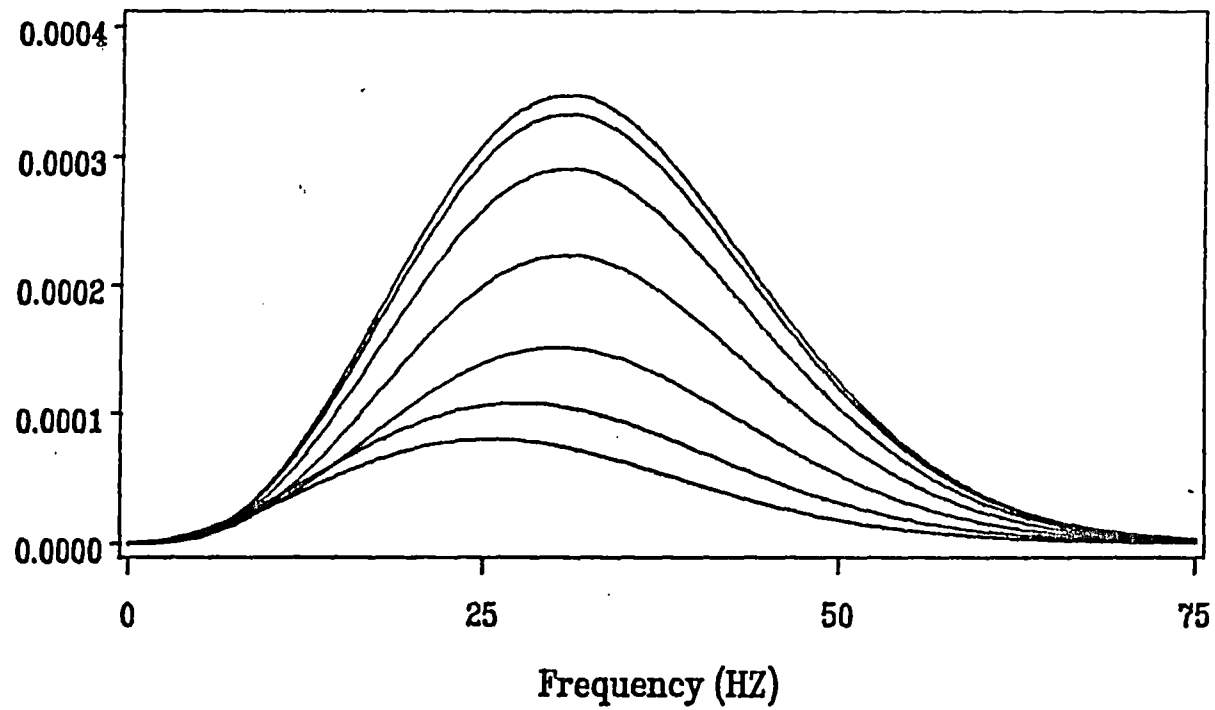


Figure 39 Variation of Fourier transforms of reflected P-waves with angle of incidence.

spectrum for the reflected p-wave (Figure 40), and for the mode converted shear wave (Figure 41). These two figures show the relative amplitude variation of the Fourier spectrum with offset for the four types of layers when they are encased in identical shales and have a thickness of 10 feet.

Gas reflection behavior is seen to be distinct in this series of Figures from other configurations. However this relative behavior is dependent on the boundary material. For instance, when the boundary material is dissimilar shales, gas and brine have very similar reflection behavior in both the time and frequency domain. The only difference is in the magnitude of the reflection rather than the relative amplitude offset dependence. The variation of the frequency shift of the spectrum maximum with layer type and thickness is illustrated in Figure 42 for a normal incident wavelet. Again, the thickness variation changes with lithology and pore fluid type.

The changes in the p-wave central frequency with both the offset and layer thickness are shown in Figure 43 for gas saturated sand encased in non-identical shale formation. The central frequency increases rapidly at normal incidence from 25 Hz at zero thickness to 29 Hz at 35 feet, then it decreases with increasing thickness.

Along a fixed thickness the central frequency varies with offset and exhibits some maximum in the range of offset shown ($0^\circ - 50^\circ$). This local maximum flattens as the

Amplitude Offset Dependence OF Reflected P-wave

Relative Amplitude

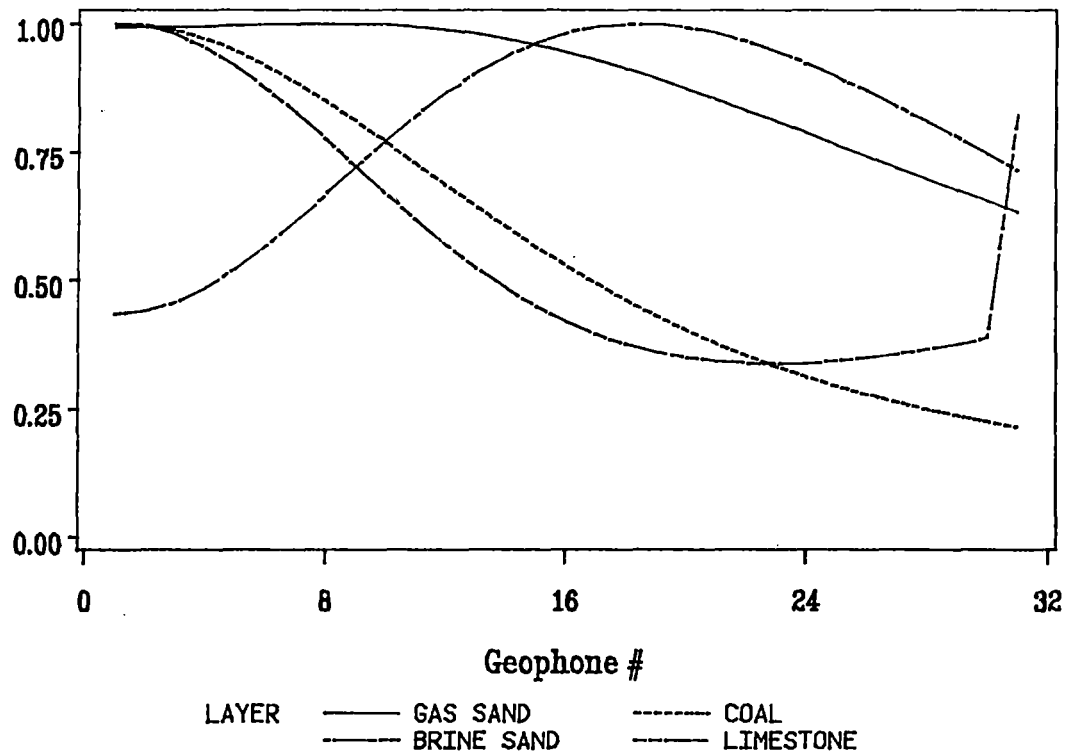


Figure 40 Relative amplitudes of reflected P-waves versus offset.

Amplitude Offset Dependence of Mode-converted S-wave

Relative Amplitude

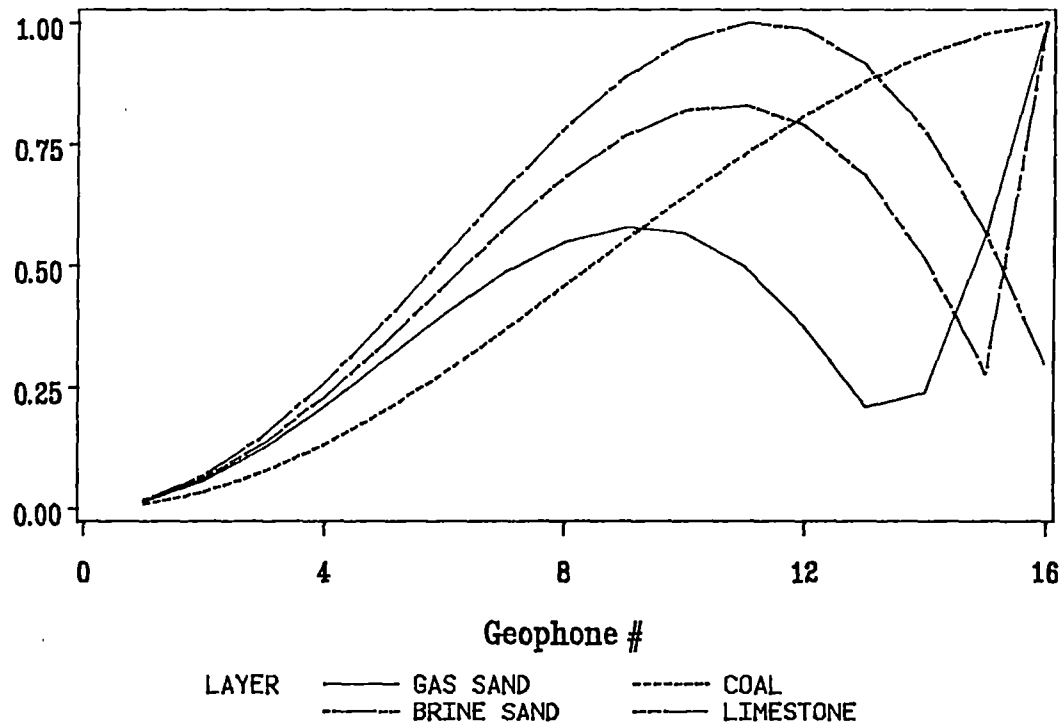


Figure 41 Relative amplitudes of mode converted S-waves versus offset.

Variation of The Central Frequency with Thickness and Lithology

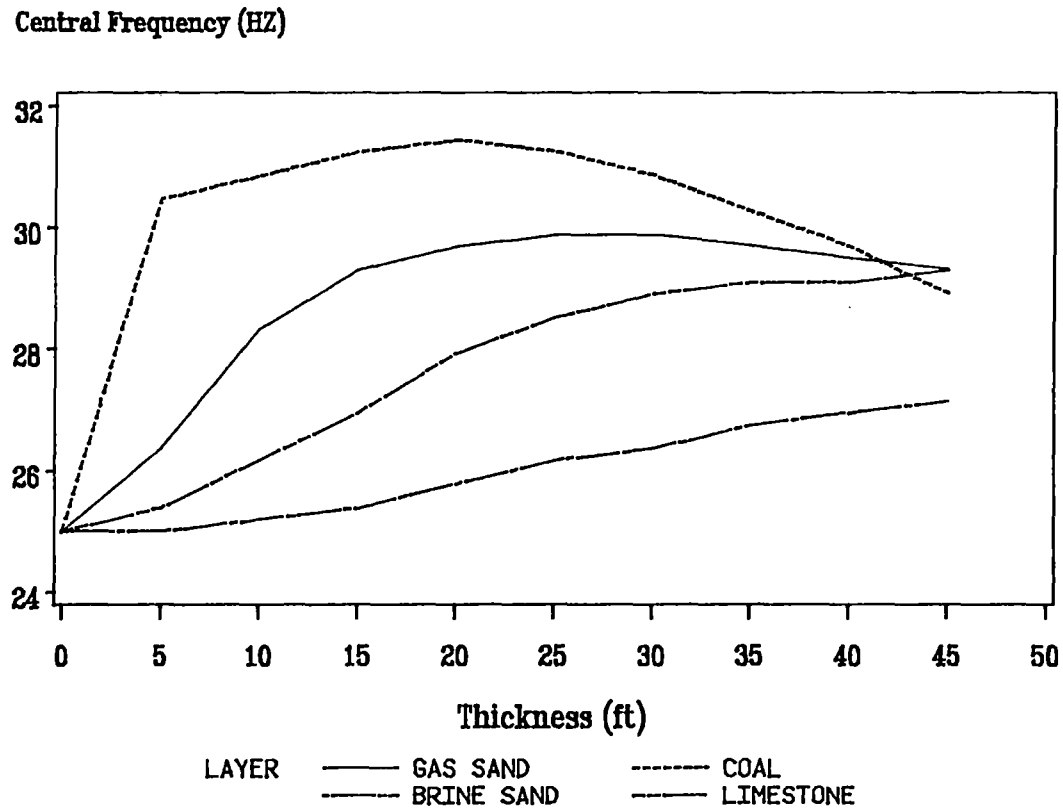


Figure 42 Variation of central frequency of reflected P-waves at normal incidence with thickness and lithology.

thickness increases from 5 feet to 35 feet. Beyond this thickness the central frequency is almost constant showing no variation with offset. As the pore fluid changes from gas to brine the central frequency still increases with thickness for a fixed offset but not as rapidly as it does with gas. Another feature is the deviation of the maximum central frequency from the normal incidence value which increases with increasing thickness, in contrast to the behavior of gas. When sandstone is replaced by limestone, the surface dependence of the central frequency has an upward curvature due to local minimum behavior (in contrast to local maximum for gas) as displayed in Figure 44. Another feature of limestone reflection is the sharp maximum just before the critical angle for all thicknesses. Coal reflection exhibits a completely different behavior. First the central frequency decreases with thickness for a fixed offset (in contrast to the behavior of other layer types), and second, the central frequency increases almost linearly with offset for a fixed thickness.

The variation of the central frequency of the mode converted shear wave with offset and layer thickness is shown for gas saturated sandstone and brine saturated sandstone in Figure 45 and Figure 46 respectively. As we compare the two figures, we see first that the curvature for gas surface is upward while the curvature for brine surface is downward. Furthermore, the value of the central frequency near normal incidence is less than $25 H$ (negative

SHALE / GAS SAND / SHALE(H)

CENTRAL FREQUENCY OF REFLECTED P-WAVE

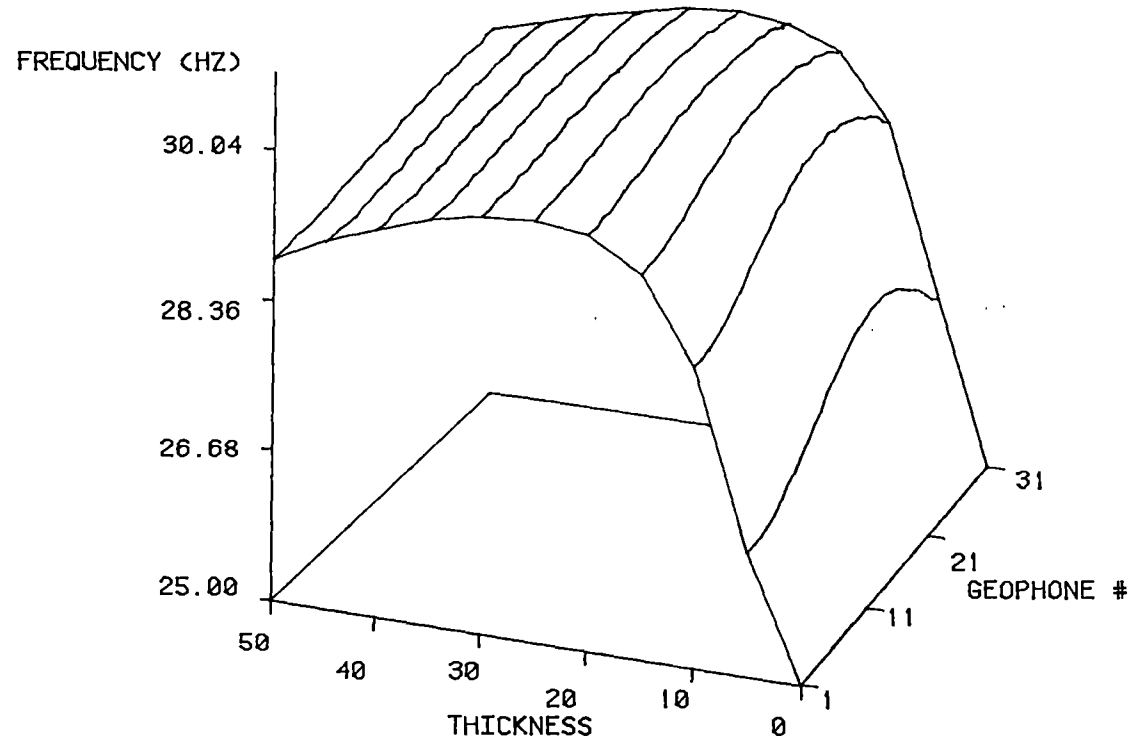


Figure 43 Variation of central frequency of reflected P-waves with offset and thickness for a gas saturated sand.

SHALE / LIMESTONE / SHALE(H)

CENTRAL FREQUENCY OF REFLECTED P-WAVE

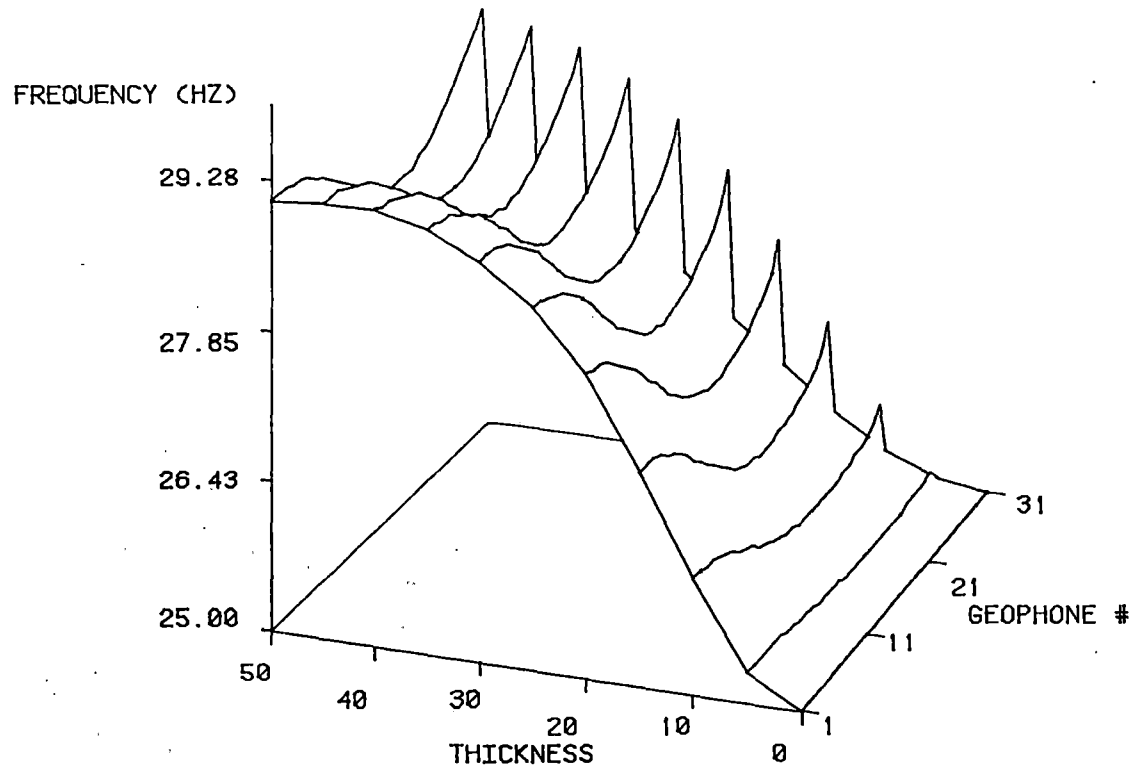


Figure 44 Variation of central frequency of reflected P-waves for a limestone layer.

SHALE / GAS SAND / SHALE(H)

CENTRAL FREQUENCY OF MODE CONVERTED S-WAVE

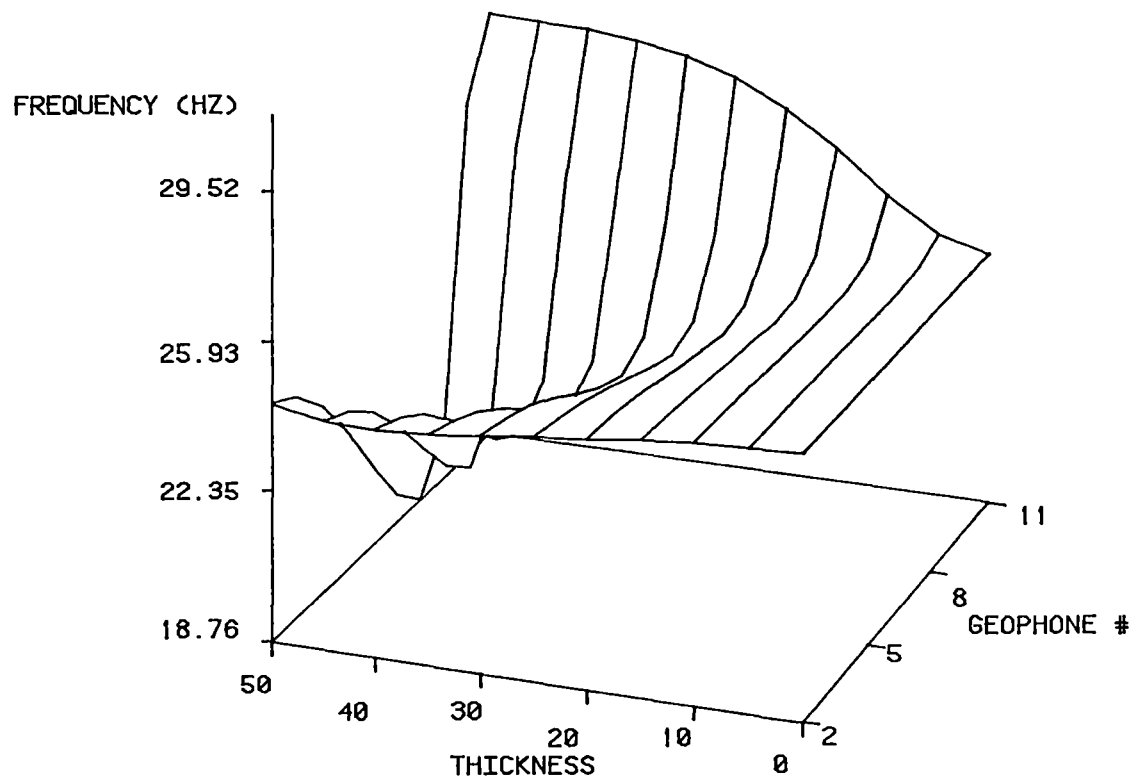


Figure 45 Central frequency shift due to offset and thickness variations for a gas saturated sand.

SHALE / BRINE SAND / SHALE(H)

CENTRAL FREQUENCY OF MODE CONVERTED S-WAVE

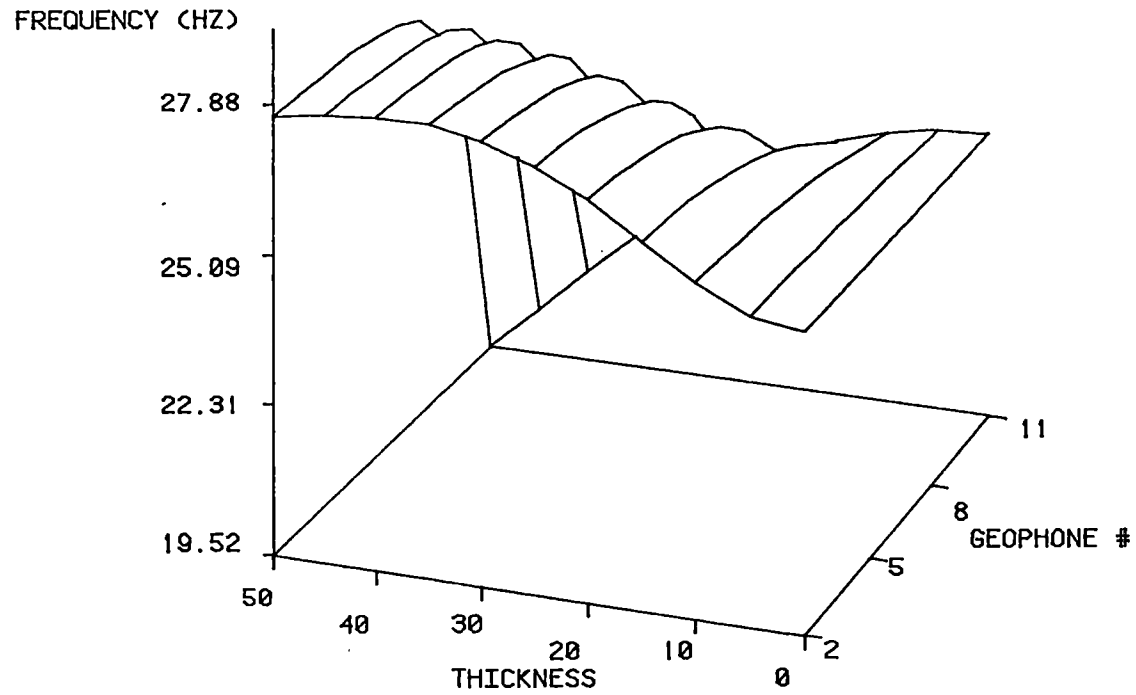


Figure 46 Central frequency shift due to offset and thickness variations for a brine saturated sand.

frequency shift) for gas while it is greater than 25 Hz (positive frequency shift) for brine saturated sand. Combining the information of the frequency shift, for both the reflected p-wave and the mode converted shear wave can help in differentiating between the pore fluids. For example, when the upper bounding material is limestone and the lower bounding material is shale, a scatter diagram can discriminate between gas and brine pore fluids of sandstone as shown in Figure 47. The vertical axis is the central frequency of the P-wave and the horizontal axis is the central frequency of the mode converted wave.

An additional characteristic which distinguishes gas reflection from others in non-identical shale formations is the low frequency content of the mode converted shear wave. This feature is easily recognized when we compare the gas reflection in Figure 48 to the brine reflection in Figure 49. The amplitude in these figures refers to the difference between the normalized Fourier transform of the mode converted wave and the normalized Fourier transform of the incident Ricker wavelet.

For a good range of offset the gas sand reflection exhibits enhanced low frequency content while brine sand reflection possesses more high frequency content.

This discussion of the analysis of time and frequency characteristics of the reflected impulse points out some general characteristics of the thin layer response.

LIMESTONE / THIN LAYER / SHALE

PP- CENTRAL FREQUENCY (HZ)

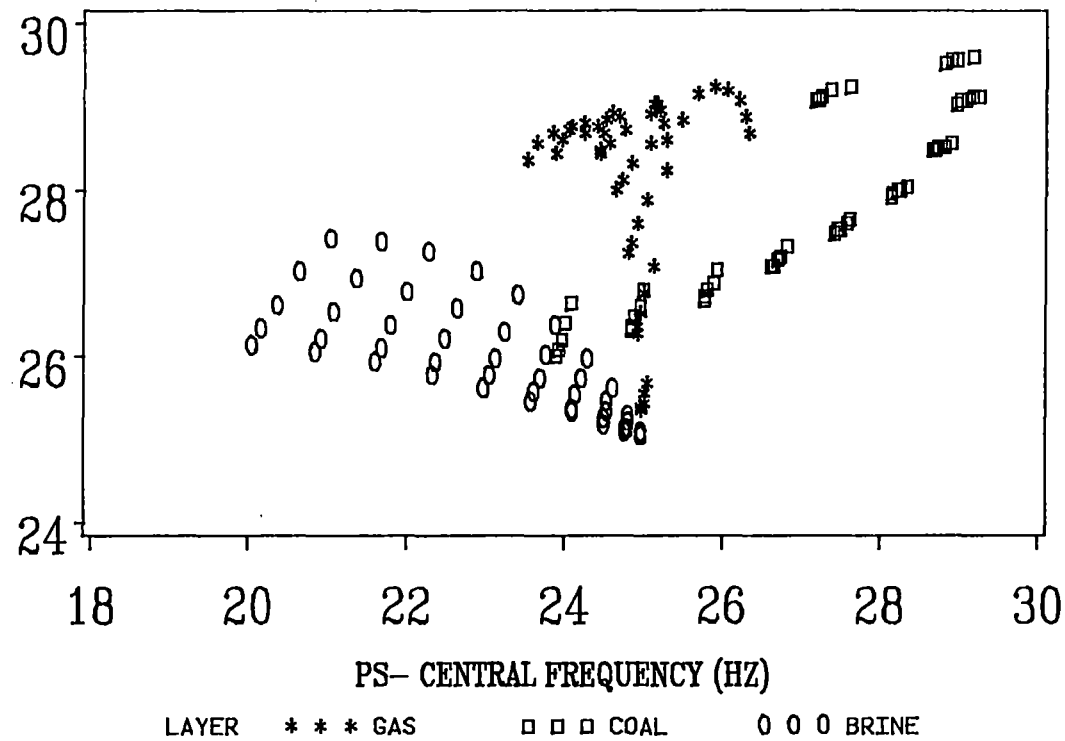


Figure 47 Scattergram of central frequencies of reflected P-waves and mode converted waves for different lithologies and pore fluids.

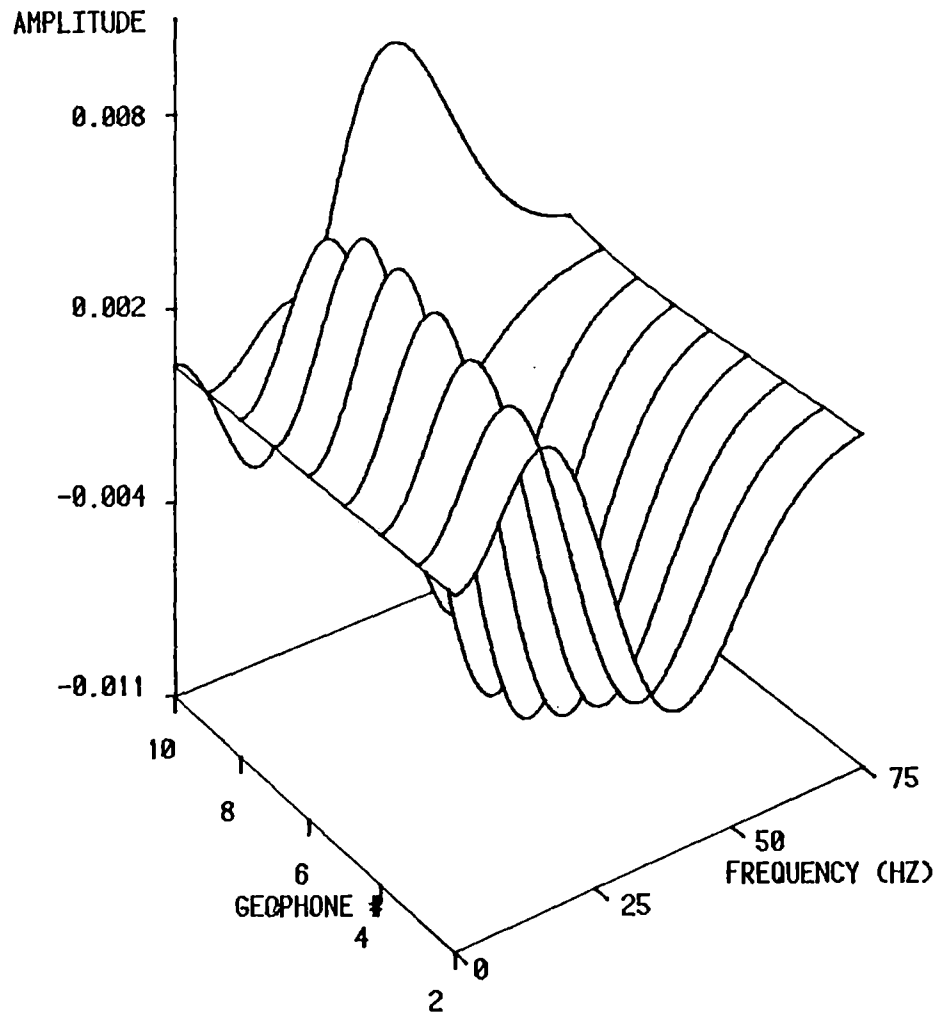


Figure 48 Normalized difference of mode-converted S-waves with respect to the incident Ricker wavelet for a gas saturated sand.

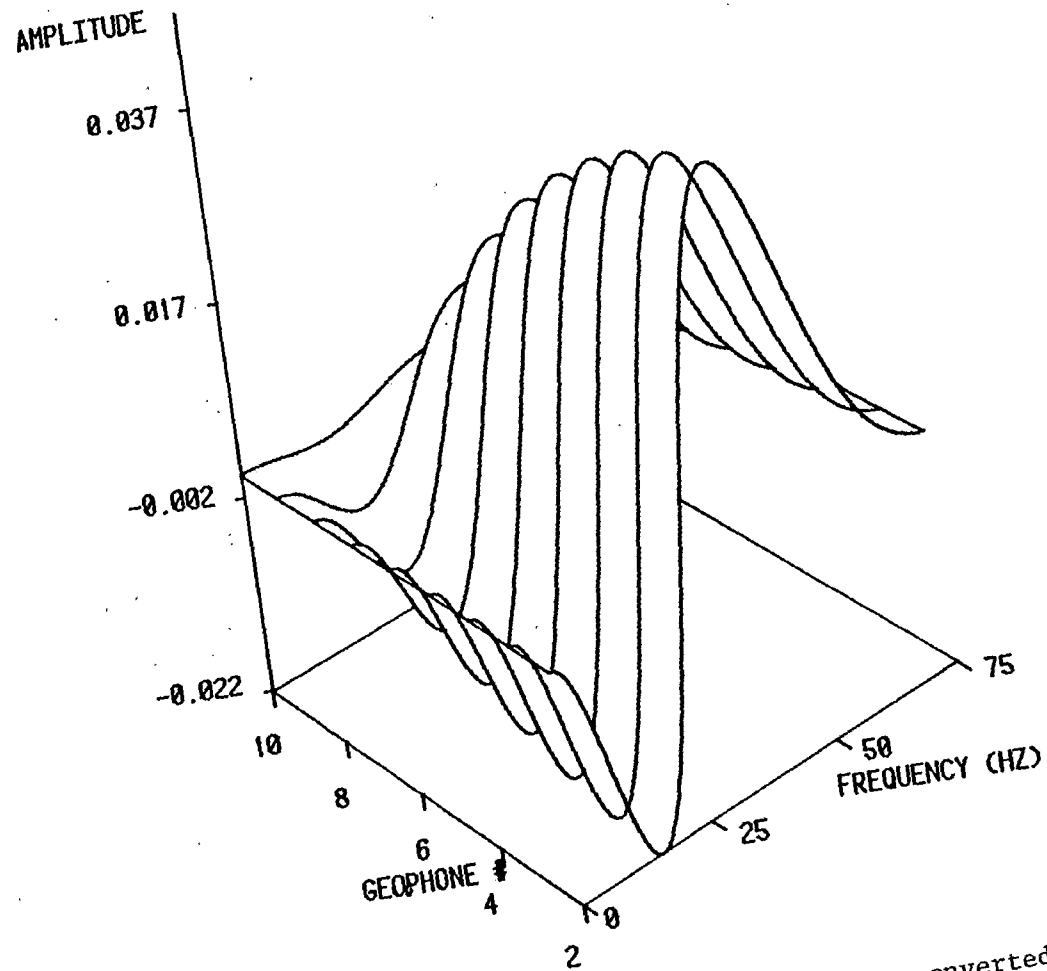


Figure 49 Normalized difference of mode converted S-waves with respect to the incident Ricker wavelet for a brine saturated sand.

1. The seismic response is a complex function of the thin layer parameters and the specific input waveform.
2. There is no single parameter which can be used to diagnose the target layer type without considerable prior knowledge of the system.
3. With some prior knowledge of the system, such as the type of boundary material or the thickness range, there are certain reflected signal features that can serve as reliable criteria to identify gas zones.
4. To evaluate lithology "in situ" a multiparameter approach in both the time and frequency domain is necessary.

MPA Definition and Application

A multiparameter approach is adopted which is designed to develop an algorithm which integrates parameters of significant features in the time and frequency domain of the reflected signal. These parameters include the impulse polarity in the time domain, the frequency shift of the maximum of the Fourier transform in the frequency domain and amplitude-offset dependence of both the reflected p-wave and the mode converted s-wave. The algorithm identifies pore fluid types without prior knowledge of the reflecting system. The input signal for this algorithm is a 25 HZ zero-phase Ricker wavelet. The algorithm proceeds in three successive stages.

The first stage utilizes the signal characteristics of the reflected p-wave at zero offset. The position of the

maximum amplitude of the Fourier transform of the reflected impulse is compared to the incident wavelet center frequency (25 Hz). The extent of the shift to higher frequencies defines the first division mode. The next evaluation criteria requires a determination of the overall shape of the pulse in the time domain (whether it is a differential reflection). The third determines the polarity of the time domain signal compared to the incident signal.

The second stage of the algorithm uses the signal characteristics of the mode converted s-wave in the neighborhood of zero offset ($<10^\circ$). It includes the central frequency shift of the Fourier transform and compares the signal polarity with respect to the Ricker wavelet derivative.

The third stage examines the amplitude-offset dependence of the reflected p-wave and the mode converted s-wave. If a prior knowledge of some parameters of the system is available, such as the boundary material or the range of thickness, some steps can be eliminated leading to a faster convergence of the algorithm in identifying the gas zones.

MPA As Applied To Thin Lithological Units

As with any other inverse technique, it is difficult to apply MPA to a general class of formations and expect a unique solution. However, when MPA is applied to configurations limited to our model (gas saturated sand, brine saturated sand, coal, and limestone encased in all

boundaries listed in Table IV), gas zones are identified as illustrated in the algorithm of Figure 50. The structure of the algorithm is based on the following observations of the characters of the reflected wavelets:

1. When the boundaries are identical the gradient layer causes the reflected p-wave to be a derivative form with a central frequency shift of more than +16% ($f_{pp} > 29$ HZ).
2. When the boundaries are not similar, only coal and limestone layers can cause the reflected p-wave to be in derivative form with a positive polarity for limestone and a negative polarity for coal.
3. The coal layer leads to a p-wave in the derivative form with a negative polarity and a mode converted s-wave in the derivative form with a positive polarity.
4. The limestone layer always causes the reflected p-wave to have a positive polarity whether or not the reflected wave is in the derivative form.
5. When the thickness range is 15 to 25 feet the gas layer is distinguished by being in the Ricker wavelet form and having a central frequency shift of more than 16% ($f_{pp} > 29$ HZ).
6. In non-identical classic formation the gas layer is characterized by the negative central frequency shift of the mode converted s-wave ($F_{ps} < 25$ HZ).
7. There are certain configuration pairs (gas I and brine II; gas V and brine VI) where the amplitude dependence

on offset of the p-wave and the mode converted s-wave are needed in addition to the central frequency shifts to identify gas as the pore fluid.

MPA As Applied To Clastic Formation

The simplicity of the algorithm increases significantly with prior knowledge of the formation characteristics. For example, if limestone boundaries and identical shales are eliminated from the layer configurations listed in Table II a more concise algorithm can identify the gas pore fluid (Figure 51). The frequency domain information for the reflected p-wave and the mode converted s-wave is sufficient to determine the pore fluid. A plot of the central frequency of the mode converted s-wave as a function of offset illustrates the separation of the various model configurations on the basis of pore fluid. The various sets of model curves are a result of different layer thicknesses. The concise form of the algorithm and segregation of the gas pore fluid characteristics in the scattergram (Figure 47) illustrate the importance of prior knowledge of the formation in simplifying the pore fluid identification process.

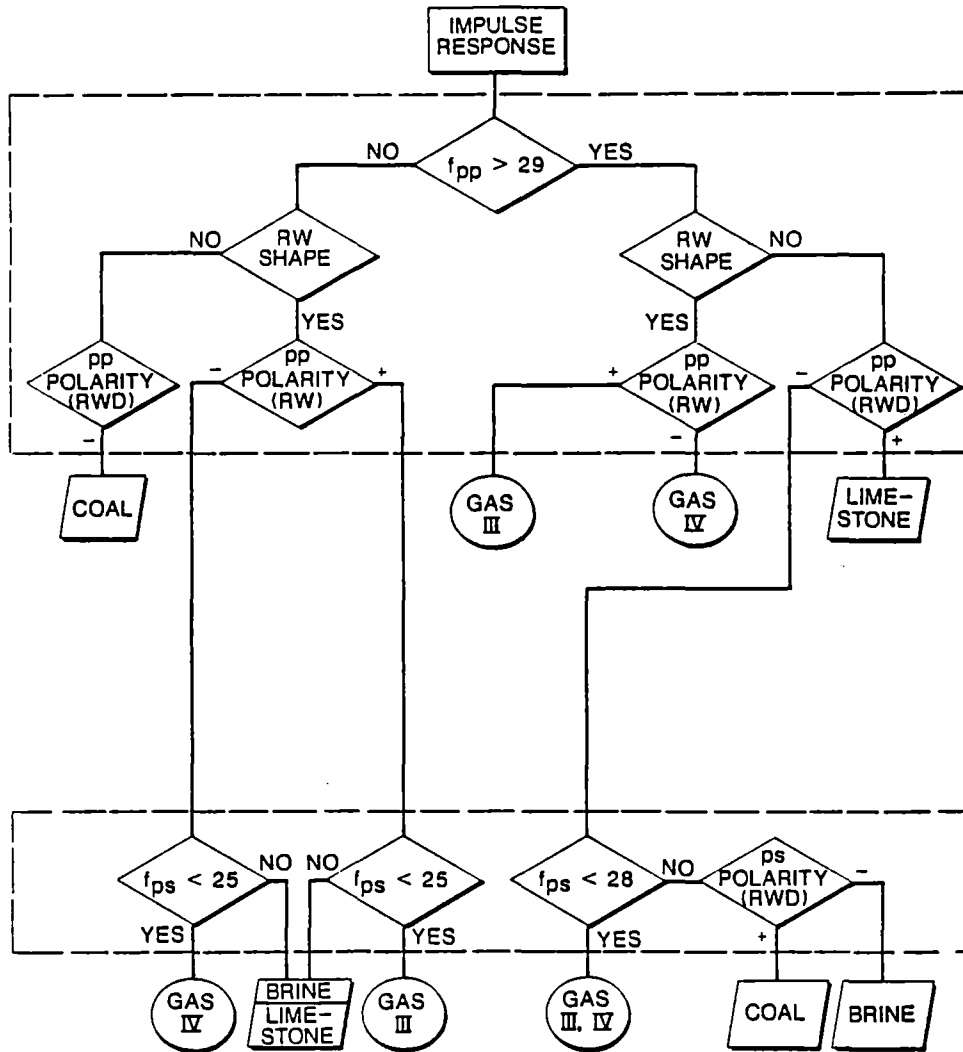


Figure 51 General scheme of MPA technique when applied to formations having shale boundaries.

CHAPTER IV

SUMMARY AND CONCLUSION

There is an ambiguity in interpreting the observed bright spots as a direct indication of gas deposits. While amplitude anomalies can at times be indications of hydrocarbon accumulation, many other factors can produce such phenomena as has been frequently observed in the exploration field. This emphasizes the importance of careful signal analysis in evaluating bright spots and other seismic data.

In this study, a three-layered seismic model has been used to evaluate the potential of using the offset dependence of seismic reflection amplitudes and impulse shapes to identify gas bearing formations. The model has been developed using the following procedure:

- I. First, the layer reflectivity is determined for a monochromatic plane p-wave by adding all of the wave components in a vector summation (amplitude and phase). The net wave amplitude is a result of interference of multiple p-waves and mode-converted s-waves generated within the layer with the primary reflection. Reflection coefficients at each interface are determined for an incident plane wave (p-wave or s-wave) by solving the boundary-value problem for

the wave equation. Results from the wave sum analysis (using a finite number of terms of multiple and mode converted waves) are summarized in the following:

1. At normal incidence where no mode-conversion occurs, the amplitude calculated from a finite wave sum approaches the exact infinite sum values after only a few terms (3 to 4).

2. At oblique incidence, mode-conversion generates other wave types and an exact solution in closed form is not available for comparison to the finite sum; however, when total incident energy flux is compared to the net reflected and transmitted energy, the overall energy is found to be conserved to within 4 percent over the entire range of incident angles.

3. The layer thickness and frequency play an important role in the interference of multiples and mode-converted waves within the layer, and hence affect the net reflection of the layer.

4. Another important parameter in determining the net reflectivity is the lithology of rocks adjacent to the layer.

5. Amplitude anomalies (bright spots) can be a result of lithology variation, such as limestone encased in shale formation, and are not necessarily associated with gas-saturated zones.

6. For thicknesses both larger and smaller than the bright spot region, the gas-saturated zones do not provide

any unusually large p-wave reflections to establish them as unique.

7. Amplitude distribution of mode-converted s-waves, together with the wave phase distribution, provide the necessary basis to identify gas related anomalies.

II. Second, impulse signal response is determined for thin layers. Synthetic seismic traces are generated as a convolution of layer reflectivity with a 25 HZ Ricker wavelet input signal. The input wavelet is digitized in the time domain using sampling methods, then expanded to its frequency components using fast Fourier transforms (FFT). Applying the inverse Fourier transforms (IFT) to the system response in the frequency domain provides the reflected wavelet in the time domain. The reflected signal shape and fourier spectrum are evaluated for varying layer lithologies, pore fluids, and bounding materials for thicknesses less than 50 feet. Amplitude-offset dependence and wavelet characteristics of both, the p-wave and the mode-converted shear-wave, are examined for varying model parameters. The parameters used in the seismic model are characteristic of the variation in acoustic impedance which occurs when systems change pore fluid from a liquid to a gas to exhibit the effects of bright spots. The lithologies of the layer and of the boundary materials are altered to determine the sensitivity of the amplitude and shape to the neighboring lithology. Preliminary results suggested the following guide lines:

1. Amplitude variation with offset alone does not uniquely define pore-fluid type.
2. It is essential to utilize the spectral characters of the reflected seismic wavelets which recognize any change in the frequency content related to the pore-fluid.
3. Polarity of seismic wavelets are very sensitive to boundary materials and they do not uniquely define pore fluids.
4. A multiparameter approach must be taken to evaluate pore-fluid type from seismic data.

III. Based on numerical calculations, a multiparameter algorithm has been developed to determine pore fluid type of thin beds. The algorithm integrates parameters of significant features (wavelet characteristics), in the time and frequency domains of reflected wavelets. These parameters include impulse polarity in the time domain; frequency shift of the maximum of the Fourier transform in the frequency domain; and amplitude-offset dependence of both the reflected p-wave and the mode-converted s-wave. Attention is focused on the frequency content of seismic waveforms due to the dispersive behavior of thin layer reflectivity which differs for various frequency components of the incident impulse. The multiparameter algorithm (MPA) identifies pore fluid types without prior knowledge of the geometry or the lithology of the reflecting system. Applying the algorithm to various model configurations,

including those which can lead to bright spots, provided quite satisfactory results.

This study has demonstrated the usefulness of the MPA technique for detailed lithologic interpretation. Results of this investigation emphasized the following:

1. Care must be exercised when interpreting bright spots. Amplitude anomalies may occur if impedance (product of velocity and density) decreases due to hydrocarbon saturation in sands; it may also occur if impedance increases due to lithology variation, as is the case for limestone layers encased in shale formation.

2. Observation of dull spots does not eliminate the possibility of having gas deposits in structures with thicknesses in the range which leads to destructive interference.

3. Gas saturated sands are characterized by the low-frequency shift of mode converted waves in dissimilar shale formations. This is in contrast to the high-frequency shift experienced by brine saturated sand in the same environment.

4. Reflected p-waves and mode-converted s-waves from coal layers are distinct in their high reflectivity and in being in the derivative form of the input Ricker wavelet.

5. Seismic waves reflected from limestone layers always experience amplitude anomalies for large offsets where they approach critical angles.

6. Recognition of quantitative difference in the frequency content of seismic wavelets for thicknesses less

than 50 feet indicates the importance of using spectral characters of seismic data for a better resolution.

7. Combination of time and frequency domain signal characteristics established the basis for a multiparameter algorithm which can be apply to thin layer offset response.

8. A minimum prior knowledge of the system can lead to fast convergence of the algorithm to identify gas pore fluids.

It is important at this stage to highlight two major difficulties regarding the direct application of the MPA technique. The first one is related to the reliability of the model. The applicability of the model depends on how close it resembles the real structure. Therefore, developing the seismic model to include multi-layer systems and layers with nonparallel boundaries should improve the applicability of MPA technique.

The second difficulty is related to the accuracy in the field measurements of parameters included in the algorithm. Offset-dependent reflectivity is affected by other factors which are not related to the physical properties of subsurface formation (Sherieff, 1975). Examples of such difficulties include source- and receiver-earth coupling which affects the directivity of the arrived signal; noise interference; spherical divergence; absorption; amplitude gain control which is commonly used in CDP gathering technique. However using relative amplitude variation as suggested in the MPA technique and applying advanced seismic

data gathering and processing techniques (Yu, 1985) should overcome these difficulties and make MPA technique a feasible approach to the evaluation of formation in situ.

REFERENCES

- Aki, K., and Richards, P., 1980, Quantitative Seismology Theory and Methods. First Ed. San Francisco: W.H. Freeman and Company, pp. 68-69.
- Almoghrabi, H., 1983, Reflection and Refraction of Acoustic waves at a Plane Interface. A Master Thesis, Oklahoma State University, 27-41.
- Almoghrabi, H. and Lange, J., 1986, Layers and Bright Spots: *Geophysics*, **51**, 699-709.
- Almoghrabi, H. and Lange, J., 1983, Acoustic Impedances and CDP Gathers, Presented at the 53rd Annual SEG International Meeting, Las Vegas, Nevada.
- Backus, M. M., 1983, Reflection seismogram in a solid layered earth: *AAPG Bull.*, **67**, 416-417.
- Brekhovskikh, L. M., 1980, Waves in layered Media: Academic Press, 15-18.
- Brigham, E., 1974, The Fast Fourier transform: Prentice-Hall Inc., 91-109.
- Craft, C., 1973, Detecting Hydrocarbons-for Years The Goal of Exploration Geophysics: *The Oil and Gas Journal*, Feb, 19. 112-125.
- Dedmand, E. V., Lindsey, J. P., and Schramm, M. W., 1975, Stratigraphic modeling: A step beyond bright spot: *World Oil*, 180, 61-65.
- De Voogd, N., and Den Rooijen, H., 1983, Thin Layer response and Spectral bandwidth: *Geophysics*, **48**, 12-18.
- Domenico, S. N., 1974, Effect of water saturation on seismic reflectivity of sand reservoirs encased in shale: *Geophysics*, **39**, 759-769.
- Domenico, S. N., 1984, Rock Lithology and porosity determination from shear and compressional wave velocity: *Geophysics*, **49**, 12-18.
- Ensley, R. A., 1984, Comparison of P-wave and S-wave seismic data: A new method for determining gas reservoirs: *Geophysics*, **49**, 1420-1421.
- Ewing, W. M., and W. S. Jardetzky, 1957, Elastic Waves in Layered Media. First Ed. New York: McGraw-Hill Book, Inc., pp. 74-89.
- Fertig, J. and Muller, G., 1978, Computations of synthetic seismograms for coal seams with the reflectivity method: *Geophysical Prospecting*, **26**, 868-883.

- Gassaway, G. S., Brown, R. A. and Bennett, L. E., 1986, Pitfalls in Seismic Amplitude Versus Offset Analysis: Case Histories, Presented at the 56th Annual SEG International Meeting, Houston, Texas.
- Gassaway, G. S. and Richgels, J. L., 1983, SAMPLE: Seismic Amplitude Measurement for Primary Lithology Estimation, Presented at the 53rd Annual SEG International Meeting, Las Vegas, Nevada.
- Gradshteyn, I. S. and Ryzhik, I. M., 1983, Table of Integrals, Series, and Products: Academic Press Inc., 1146-1148.
- Gregory, A. R., 1977, Rock physics in seismic interpretation, in Seismic Stratigraphy-Applications to hydrocarbon exploration, Payton, C. E., Ed: Am. Ass'n Petr. Geol., memoir 26, Tulsa, 15-46.
- Helbig, K. and Mesdag, C. S., 1982, The potential of shear-wave observations: Geophysical Prospecting, **30**, 413-431.
- Kallaweit, R. S. and Wood, L. C., 1982, The Limits of Resolution of Zero-phase Wavelets: Geophysics, **47**, 1035-1046.
- Koefoed, O., and De Voogd, N., 1980, The Linear Properties of Thin Layers, with an Application to Synthetic Seismograms over Coal Seams: Geophysics, **45**, 1254-1268.
- Lange, J. and Almoghrabi, H., 1986, Impulse Reflectivity of Thin Layers: Modeling: Presented at the 56th Annual SEG International Meeting, Houston, Texas.
- McCormick, M. D., Dunbar, J. A. and Sharp, W. W., 1984, A case study of stratigraphic interpretation using shear and compressional seismic data: Geophysics, **49**, 509-520.
- Meckel, L. D., and Nath, A. K., 1977, Geologic Considerations for stratigraphic modeling and interpretation, in Seismic stratigraphy-Applications to hydrocarbon exploration: C. E. Payton, Ed: Am. Ass'n. Petr. Geol., memoir 26, Tulsa, 417-438.
- Meissner, R. and Hegazy, M. A., 1981, The ratio of the PP- to the SS-reflection coefficient as a possible future method to estimate oil and gas reservoirs: Geophysics Prosp., **29** 533-540.
- Meissner, R., and Meixner, E., 1969, Deformation of seismic wavelets by thin layers and layered boundaries: Geophysical Prospecting, **17**, 1-27.
- Neidell, N. S., and E. Poggiagliolmi, 1977, Stratigraphic modeling and interpretation - Geophysical Principles and Techniques in Seismic stratigraphy - Applications to hydrocarbon exploration: C. E. Payton, Ed: Am. Ass'n. Petr. Geol., memoir 26, Tulsa, 389-416.
- Ostrander, W. J., 1982, Plane Wave Reflection Coefficients for Gas Sands at Nonnormal Angles of Incidence: Presented at the 52nd Annual SEG International Meeting, Dallas, Texas.
- Ostrander, W. J., 1984, Plane-wave reflection coefficients for gas sands at non-normal angles of incidence: Geophysics, **49**, 1637-1648.

- Pan, P. and De Bremaecker, J. C. L., 1970, Direct location of oil and gas by the seismic reflection method: *Geophysical Prospecting*, **18**, 712-727.
- Ricker, N.H., 1945, The computation of output disturbances from amplifiers for true wavelet inputs: *Geophysics*, **10**, 207-220.
- Robertson, J. D., and Nogami, H. H., 1984, Complex seismic trace analysis of thin beds: *Geophysics*, **49**, 344-352.
- Robertson, J. D., and Prichett, W. C., 1985, Direct hydrocarbon detection using comparative P-wave and S-wave seismic sections: *Geophysics*, **50**, 383-393.
- Ross, A. E., 1984, Comparison of P- and S-wave seismic data: A new method for detecting gas reservoirs. *Geophysics*, **49**, 1420-1431.
- Sengbush, R. L., Lawrence, P. L., and McDonel, F. J., 1961, Interpretation of synthetic seismograms: *Geophysics*, **28**, 45-58.
- Sherieff, R. E., 1975, Factors affecting seismic amplitudes: *Geophysical Prospecting*, **23**, 125-138.
- Sinvhal, A. and Khattri, K., 1983, Application of seismic reflection data to discriminate subsurface Lithostratigraphy: *Geophysics*, **48**, 1498-1513.
- Stumpel, H., Kahler, S., Meissner, R. and Milkereit, B., 1984, The use of seismic shear waves and compressional waves for lithological problems of shallow sediments: *Geophysical Prospecting*, **32**, 662-675.
- Taner, M. T., Koehler, F., and Sheriff, R. E., 1979, Complex seismic trace analysis: *Geophysics* **44**, 1041-1063.
- Tatham, R. H. and Stoffa, P. L., 1976, VP/VS - A potential hydrocarbon indicator: *Geophysics*, **41**, 837-849.
- Tatham, R.H., Goolsbee, D.V., Massell, W.F., and Nelson, H.R., 1983, Seismic Shear-wave Observations in a Physical Model Experiment: *Geophysics*, **48**, 688-701.
- Widess, M. B., 1973, How thin is a thin bed?: *Geophysics*, **38**, 1176-1180.
- Wilkens, R., Simmons, G. and Caruso, L., 1984, The Ratio V_p/V_s as a discriminate of Composition for Siliceous Limestones: *Geophysics*, **49**, 1850-1860.
- Wuenschel, P. C., 1960, Seismogram synthesis including multiples and transmission coefficients: *Geophysics*, **25**, 106-129.
- Yu, Gary, 1985, Offset Amplitude Variation and Controlled Amplitude Processing: Presented at the 55th Annuyal SEG International Meeting, Washington, D.C.

APPENDIX A

COMPUTATION OF THE FAST FOURIER TRANSFORM

FFT is a fast algorithm which computes the discrete Fourier transform. FFT algorithm is easily achieved by calling a FORTRAN subroutine from IMSL library and does not require a mathematical background of the algorithm. The subroutine used here computes the FFT of a complex valued sequence of length equal to a power two by the following calling statement:

```
CALL FFT2C (A,M, IWK).
```

The definitions of the arguments are as follows:

- A - COMPLEX VECTOR OF LENGTH N, WHERE $N=2^{**}M$. ON INPUT A CONTAINS THE COMPLEX VALUED SEQUENCE TO BE TRANSFORMED. ON OUTPUT A IS REPLACED BY THE FOURIER TRANSFORM.
- M - INPUT EXPONENT TO WHICH 2 IS RAISED TO PRODUCE THE NUMBER OF DATA POINTS, N (I.E. $N = 2^{**}M$).
- IWK - WORK VECTOR OF LENGTH M+1.

REMARKS 1. FFT2C COMPUTES THE FOURIER TRANSFORM, X, ACCORDING TO THE FOLLOWING FORMULA;

$$X(K+1) = \text{SUM FROM } J = 0 \text{ TO } N-1 \text{ OF} \\ A(J+1) * \text{CEXP} ((0.0, (-2.0*PI*J*K) / N)) \\ \text{FOR } K=0, 1, \dots, N-1 \text{ AND } PI=3.1415\dots$$

NOTE THAT X OVERWRITES A ON OUTPUT.

2. FFT2C CAN BE USED TO COMPUTE THE INVERSE FOURIER TRANSFORM, A, ACCORDING TO THE FOLLOWING FORMULA;

$$X(K+1) = (1/N) * \text{SUM FROM } J = 0 \text{ TO } N-1 \text{ OF} \\ A(J+1) * \text{CEXP} ((0.0, (-2.0*PI*J*K) / N)) \\ \text{FOR } K=0, 1, \dots, N-1 \text{ AND } PI=3.1415\dots$$

BY PERFORMING THE FOLLOWING STEPS;

```
DO 10 I=1,N
  A(I) = CONJG (A(I))
10 CONTINUE
CALL FFT2C (A, M, IWK)
```

```

          DO 20 I=1,N
            A(I) = CONJA (A(I))/N
20 CONTINUE

```

The output vector X is defined mathematically as

$$X_{K+1} = \sum_{j=0}^{N-1} A_{j+1} e^{2\pi i j k / N} \quad \text{where } k=0, 1, \dots, N-1; N=2^M; i=\text{SORT}(-1)$$

Computationally, the above summation which defines S requires N^2 complex multiplications and additions. FFT2C utilizes a modification of the Singleton version of the Cooley-Tuckey FFT algorithm which requires only $N \log_2 N$ basic sets of operations.

Programming Notes

Note that the forward and inverse transforms are sometimes defined differently in the mathematical literature.

Example

This example computes the FFT of a sequence of length 8. Therefore, $M=3$ ($8=2^3$) and the input is $A(1), \dots, A(8)$.

Input

```

INTEGER M, IWK (4)
COMPLEX A (8)
M      = 3
A(1)   = (1.0,2.0)
A(2)   = (4.0,1.0)
A(3)   = (3.0,3.0)
A(4)   = (0.0,1.0)
A(5)   = (2.0,4.0)
A(6)   = (3.0,0.0)
A(7)   = (2.0,2.0)
A(8)   = (1.0,3.0)
CALL FFT2C (A, M, IWK)
      .
      .
      .
END

```

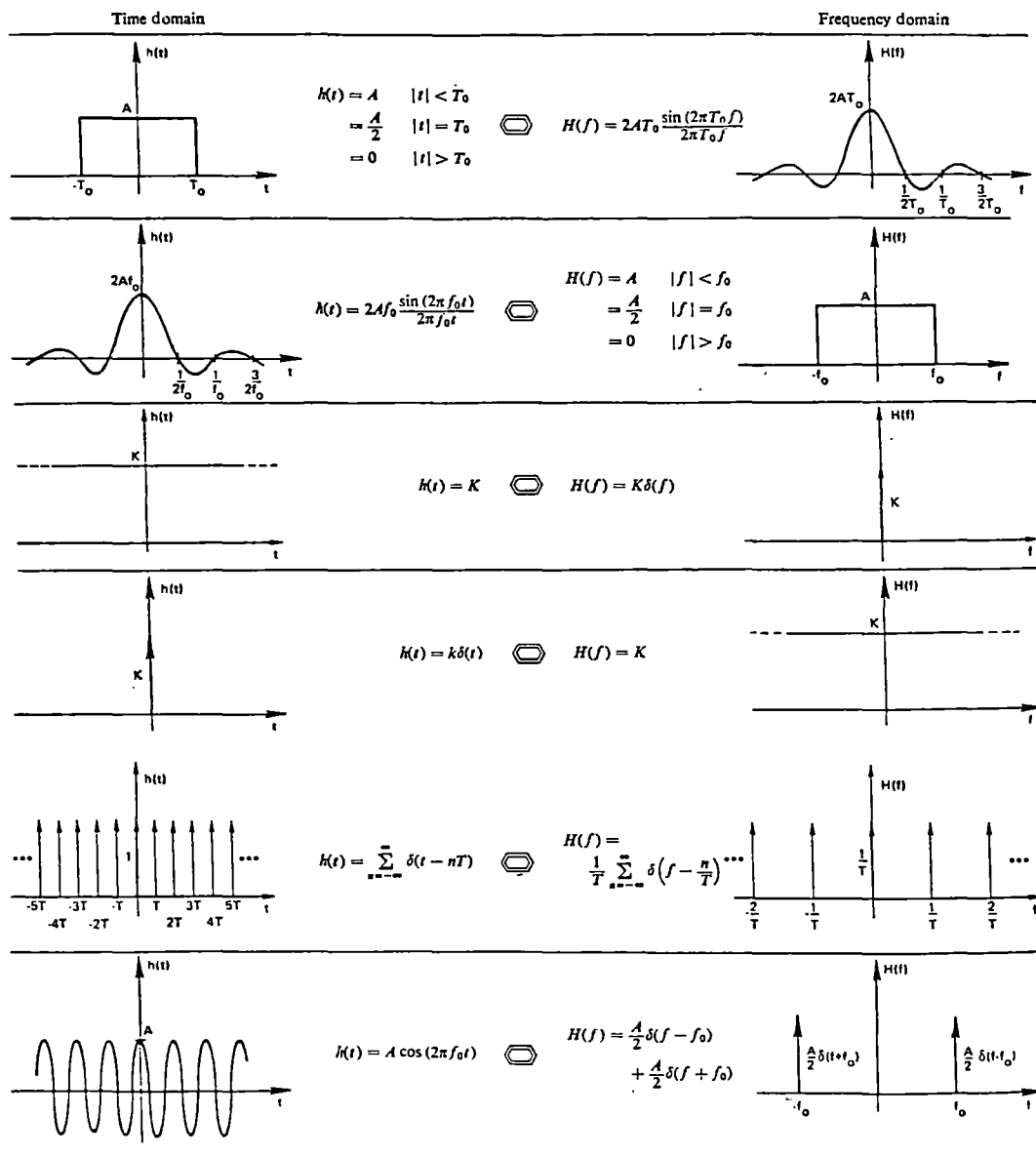
Output:

A(1) = (16.0,16.0)
A(2) = (.121,1.12)
A(3) = (1.0,7.0)
A(4) = (-.707,-5.12)
A(5) = (0.0,6.0)
A(6) = (-4.12,-3.12)
A(7) = (-5.0,-5.0)
A(8) = (.707,-.879)

APPENDIX B

A PICTORIAL TABLE OF FOURIER TRANSFORM PAIRS

The following pictorial table summarizes the Fourier transform pairs which are most frequently encountered in signal analysis (Brigham, 1974).



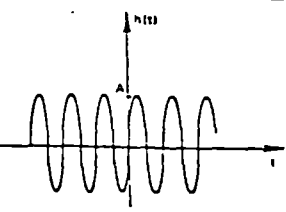
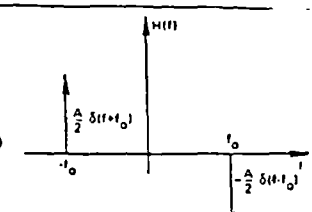
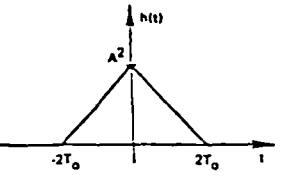
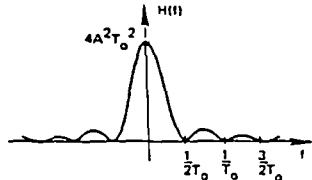
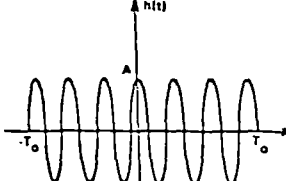
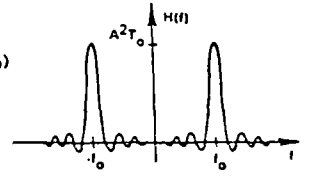
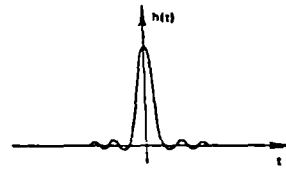
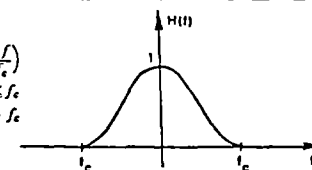
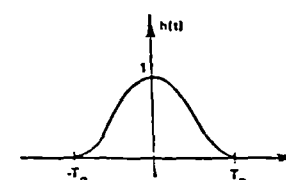
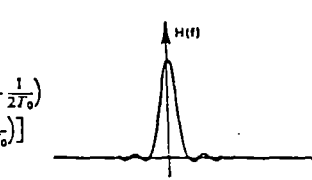
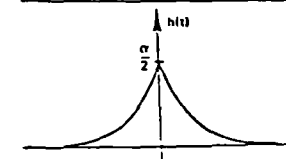
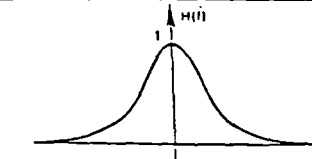
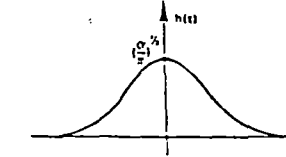
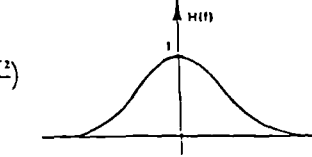
Time domain		Frequency domain
	$h(t) = A \sin(2\pi f_0 t)$	$H(f) = -j\frac{A}{2}\delta(f - f_0) + j\frac{A}{2}\delta(f + f_0)$ 
	$h(t) = -\frac{A^2}{2T_0}t + A^2 \quad t < 2T_0$ $= 0 \quad t > 2T_0$	$H(f) = A^2 \frac{\sin^2(2\pi T_0 f)}{(\pi f)^2}$ 
	$h(t) = A \cos(2\pi f_0 t) \quad t < T_0$ $= 0 \quad t > T_0$	$H(f) = A^2 T_0 [Q(f + f_0) + Q(f - f_0)]$ $Q(f) = \frac{\sin(2\pi T_0 f)}{2\pi f}$ 
	$h(t) = \frac{1}{2}q(t) + \frac{1}{4}q\left(t + \frac{1}{2f_c}\right) + \frac{1}{4}q\left(t - \frac{1}{2f_c}\right)$ $q(t) = \frac{\sin(2\pi f_c t)}{\pi t}$	$H(f) = \frac{1}{2} + \frac{1}{2}\cos\left(\frac{\pi f}{f_c}\right)$ $= 0 \quad f > f_c$ 
	$h(t) = \frac{1}{2} + \frac{1}{2}\cos\left(\frac{\pi t}{T_0}\right) \quad t \leq T_0$ $= 0 \quad t > T_0$	$H(f) = \frac{1}{2}Q(f) + \frac{1}{4}\left[Q\left(f + \frac{1}{2T_0}\right) + Q\left(f - \frac{1}{2T_0}\right)\right]$ $Q(f) = \frac{\sin(2\pi T_0 f)}{\pi f}$ 
	$h(t) = \frac{1}{2}a \exp(-a t)$	$H(f) = \frac{a^2}{a^2 + 4\pi^2 f^2}$ 
	$h(t) = \left(\frac{\alpha}{\pi}\right)^{1/2} \exp(-\alpha t^2)$	$H(f) = \exp\left(-\frac{\pi^2 f^2}{\alpha}\right)$ 

Table (Continued)

APPENDIX C

BASIC PROPERTIES OF THE FOURIER TRANSFORM

The following table summarizes the basic properties of the Fourier transform
(Brighan, 1974)

Property	Time domain	Frequency domain
Linearity	$x(t) + y(t)$	$X(f) + Y(f)$
Time Scaling	$h(kt)$	$(1/K) H(f/K)$
Frequency Scaling	$(1/K) h(t/K)$	$H(Kf)$
Time Shifting	$h(t-t_0)$	$H(f) e^{-i2\pi f t_0}$
Frequency Shifting	$H(f) e^{-i2\pi f t_0}$	$H(f-f_0)$
Even Functions	$h(t) = h_e(t)$	$H_e(f) = R_e(f)$
Odd Functions	$h(t) = h_o(t)$	$H_o(f) = iI_o(f)$
Convolution	$\int_{-\infty}^{\infty} h(\tau) x(t-\tau) dt$	$H(f) X(f)$
Correlation	$\int_{-\infty}^{\infty} h(\tau) x^*(t-\tau) dt$	$H(f) X^*(f)$

2

VITA

Hamzah Abdulgader Almoghrabi

Candidate for the Degree of

Doctor of Philosophy

Thesis: NUMERICAL EVALUATION OF BRIGHT SPOTS AND THIN LAYER
REFLECTIVITY

Major Field: Physics

Biographical:

Personal Data: Born in Khulais, Hejaz, Saudi Arabia, May 13, 1955. Married to Naherah Ahmed and has two daughters and one son.

Education:

Graduated from Al Shati High School, Jeddah, Saudi Arabia, in 1972, received Bachelor of Science degree in Physics from the University of Petroleum and Minerals, Dahrhan, Saudi Arabia, in May 1977; received Master of Science Degree in Physics from Oklahoma State University in July 1983; Completed requirements for the Doctor of Philosophy Degree at Oklahoma State University in December, 1986.

Professional Experience:

Teaching Assistant, Department of Physics and Mathematics, College of Architecture, King Faisal University, 1977-1979; Research Assistant, Department of Physics, Oklahoma State University, January 1983 to December 1986.

Professional Organizations:

Member of the Society of Exploration Geophysicists, and The American Physical Society.